Depletion, Quantum Jumps, and Temperature Measurements of $^{88}Sr^+$ Ions in a Linear Paul Trap

by

Philip J. Richerme

Submitted to the Department of Physics
in partial fulfillment of the requirements for the degree of

Bachelor of Science in Physics

at the

MASSACHUSETTS INSTITUTE OF TECHNOLOGY

June 2006

© Massachusetts Institute of Technology 2006. All rights reserved.

Author ....
Department of Physics
May 12, 2006

Certified by ....
Isaac L. Chuang
Associate Professor
Thesis Supervisor

Accepted by ....
David E. Pritchard
Senior Thesis Coordinator

MASSACHUSETTS INSTITUTE OF TECHNOLOGY
JUL 07 2006
LIBRARIES
ARCHIVES

Depletion, Quantum Jumps, and Temperature Measurements of $^{88}Sr^+$ Ions in a Linear Paul Trap

by

Philip J. Richerme

Submitted to the Department of Physics
on May 12, 2006, in partial fulfillment of the
requirements for the degree of
Bachelor of Science in Physics

Abstract

This thesis describes the design and construction of two laser systems to probe the 674nm transition of $^{88}Sr^+$ ions in a linear Paul trap. The first laser system made use of a molecular transition in Iodine to stabilize the length of a Fabry-Perot cavity for laser locking. After constructing this laser, we measured an unsuitable experimental stability of 10 MHz over 5 minutes. A completely new monolithic laser system was built, providing better environmental isolation and a frequency stability of at least 1 MHz over 5 minutes. Using this laser, we were able to observe depletion and quantum jump effects in our ion trap system. Additionally, by scanning the red laser frequency, we were able to see the blue-laser broadened spectrum of the 674nm transition. Fitting the spectrum to a Voigt function yielded an ion temperature of 35 mK. To avoid blue-broadening, we set up blue and red laser pulse sequences. This allowed us to observe a red spectrum with secular sidebands and calculate an ion temperature of $6.8^{+4.4}_{-2.2}$ mK.

Thesis Supervisor: Isaac L. Chuang
Title: Associate Professor

Acknowledgments

Researching and writing a thesis is a task greatly simplified by the helpful advice and support of others. With this in mind, I would like to acknowledge the Quanta research group as a whole. Every member of the group has shown me a great deal of kindness and has been amazingly eager to help whenever necessary.

Specifically, I would like to thank the two graduate students, Rob Clark and Jarek Labaziewicz, with whom I worked most closely. I greatly appreciate the large amount of time that Rob has sacrificed for me, teaching me how to trap ions, explaining the physics behind the various experiments around lab, and serving as a fantastic sounding board for my experimental ideas. Jarek has also devoted quite a lot of his time teaching me and helping me set up my experiments. He has taught me practically everything that I know about lasers and laser systems.

Ken Brown, the postdoc, has been phenomenal. He has displayed seemingly infinite patience towards me while explaining the theoretical background of my experiments. He has consistently challenged me to improve my understanding of physics, and has always been willing to help solve any problem I may have faced. Additionally, he has lent me a sizable amount of sound career advice, for which I am extremely grateful.

It goes without saying that I am indebted to Prof. Isaac Chuang. He has allowed me to thrive in his lab, given me an interesting and stimulating research project, and offered his vast knowledge and expertise whenever I got stuck. I am certain that his attention to detail and high standards have made me a better physicist.

Finally, I would like to thank my parents for their never-ending support and constant reminders that there is indeed life outside of lab.

Contents

1 Introduction **15**

1.1 Background 15

1.2 Overview 16

1.3 Contributions to this work 16

2 Ion Trapping **19**

2.1 The Linear Quadrupole Paul Trap 20

2.2 Full Solution: The Mathieu Equation 22

2.3 The Secular Approximation 25

2.4 Operating the Trap 28

2.4.1 Vacuum System 29

2.4.2 Ionization 30

2.4.3 Ion Detection 30

2.4.4 Compensation 32

2.5 Summary 33

3 The Strontium Ion **35**

3.1 Energy Level Structure 35

3.1.1 The 422nm Transition 36

3.1.2 The 1092nm Transition 38

3.1.3 The 674nm Transition 38

3.2 Linewidth Considerations 39

3.3 Depletion, Quantum Jumps, and Temperature Measurements 40

3.3.1 Depletion 40
3.3.2 Quantum Jumps 41
3.3.3 Temperature Measurements 44
3.4 Sideband Cooling 47
3.5 Summary 49

4 An Iodine-Stabilized Red Laser **51**
4.1 Theoretical Background 51
4.1.1 Laser Diodes 51
4.1.2 Diffraction Gratings 53
4.1.3 Absorption Cells 55
4.1.4 Fabry-Perot Cavities 56
4.1.5 Electronic Feedback 62
4.2 The Dual-Laser Setup 65
4.3 Laser Construction 66
4.3.1 Building an ECDL 66
4.3.2 Optical Breadboard Setups 70
4.4 Stability Results 73
4.4.1 Side-locking to a Fabry-Perot Cavity 73
4.4.2 Side-locking to Iodine Transition 75
4.4.3 Peak-locking to Iodine Transition 76
4.4.4 Locking to a Saturated Absorption Line 76
4.5 Summary 77

5 A Monolithic Red Laser **79**
5.1 Monolaser Design 80
5.1.1 Optical Breadboard Setup 80
5.1.2 The Filter Cavity 83
5.2 Construction of the Monolaser 85
5.2.1 Baseplate and Housing 85
5.2.2 Diode Mounting, Collimation, and Frequency Tuning 86

5.2.3 Transmission Through the Filter Cavity 87
5.2.4 Feedback and Operation 88
5.3 Monolaser Stability 91
5.4 Summary 93

6 Experimental Setup and Results **95**
6.1 Ion Trap Setup 95
6.2 Depletion 97
6.3 Quantum Jumps 99
6.4 Temperature Measurements 101
6.4.1 Blue-broadened Regime 101
6.4.2 Resolved Sideband Regime 104

7 Conclusion **107**

A MATLAB Code for Quantum Jump Simulations **111**

List of Figures

2-1 Schematic of the linear Paul trap. 20
2-2 The radial potential at two points in time. 21
2-3 Mathieu stability regions in the $a - q$ plane. 24
2-4 Secular motion and micromotion for a trapped ion. 28
2-5 Schematic of the ion trap chamber and vacuum assembly. 29
2-6 Picture of the trap chamber showing the strontium oven and electron gun. 30
2-7 Optical setup for detecting and imaging ions. 31
2-8 CCD camera image of trapped ions. 32
2-9 Detection of Ion Micromotion. 33

3-1 Energy level diagram for $^{88}\mathrm{Sr}^{+}$. 36
3-2 Laser-induced fluorescence at 422nm from a cold chain of ions. 37
3-3 Numerical solution to the 3-level problem with spontaneous emission. 42
3-4 Probability of being in the D state as a function of Rabi frequency with the red laser on resonance. 43
3-5 Monte-Carlo simulation of quantum jumps for two different red Rabi frequencies. 44
3-6 Expected spectrum of the 674nm line for high and low red laser power. 45
3-7 Energy level diagram for sideband cooling. 48

4-1 The Sanyo DL3149-056 laser diode. 52
4-2 Schematic of an extended-cavity diode laser. 54
4-3 Drawing of a Fabry-Perot cavity. 57

4-4 Fabry-Perot interference fringes for three different mirror reflectivities. 59
4-5 Fabry-Perot cavity in a confocal arrangement. 61
4-6 Side-locking to a voltage signal. 63
4-7 Peak-locking to a voltage signal. 64
4-8 Schematic of the dual-laser setup. 66
4-9 Photographs of the ECDL baseplate and housing. 67
4-10 Photographs of the collimation process. 69
4-11 Characteristic Power-Current curve for the Sanyo DL3149-056 laser diode. 70
4-12 Photograph of a laser stabilized to a Doppler-broadened Iodine line. . 71
4-13 Pictures and schematic of a saturated-absorption setup. 72
4-14 Schematic of a laser system locked to an iodine-stabilized Fabry-Perot cavity. 74
4-15 Frequency drifts of a laser side-locked to an Iodine transition. 75
4-16 Frequency drifts of a laser peak-locked to an Iodine transition. 76

5-1 Optical layout for the monolithic laser. 81
5-2 Photograph of the filter cavity. 83
5-3 Photograph of the monolaser baseplate. 85
5-4 Photograph of the completed monolaser. 86
5-5 Transmission through and reflection from a well-aligned filter cavity. . 88
5-6 Filter cavity transmission spectrum with optical feedback. 89
5-7 Schematic of an AOM in a double-pass configuration. 90
5-8 Monolaser frequency stability over a 5 minute period. 91
5-9 Blue monolaser frequency stability over a 5 minute period when locked to the ion fluorescence signal. 92

6-1 Schematic of the ion trap setup. 96
6-2 Depletion in an ion cloud. 97
6-3 Depletion in an ion crystal. 98
6-4 Quantum jumps of 3 trapped strontium ions. 99

6-5 Discrete quantum jump levels. 100
6-6 Frequency dependence of ion fluorescence in the high red power limit. 102
6-7 Frequency dependence of ion fluorescence in the low red power limit. 103
6-8 The 674nm transition spectrum with resolved sidebands. 105

Chapter 1

Introduction

1.1 Background

Atomic ion traps exemplify an experimental elegance that is difficult to surpass. They permit physicists to study and control ions with exceptional precision to gain insight into the quantum world. Ion traps come in many flavors and sizes [1, 2], and have been used to perform various experiments in a wide range of subfields.

This thesis is concerned with trapping $^{88}\mathrm{Sr}^{+}$ in a linear Paul ion trap. Owing to the electronic level structure of strontium, blue and infrared (IR) lasers are required to trap, cool, and image the ion. Unfortunately, after the trapping has succeeded, there is little further science that can be performed with these two lasers alone.

We can now ask what types of experiments become accessible if we introduce a third laser to address the 674nm red transition in $^{88}\mathrm{Sr}^{+}$. One can group the possible experiments roughly into three classes: quantum phenomena, ion probing, and quantum information. Experiments in the first category, such as depletion, quantum jumps, and the quantum Zeno effect, are able to test and verify the fundamentals of quantum theory. The second type of experiments, such as temperature measurements and sideband cooling, use the red laser as a probe to determine and affect properties of the ions and ion trap system. The third class of experiments investigates how information can be stored and manipulated using trapped ions. This thesis will focus on the depletion, quantum jump, and temperature measurement experiments.

1.2 Overview

Before presenting the experiments in detail, a suitable background must first be established. Chapter 2 presents a broad overview of the ion trapping process. Sections 2.1-2.3 detail the geometry and mathematics pertaining to the trap used in our strontium experiments. Section 2.4 describes the finer points of trap operation, including construction of the vacuum system, producing and detecting ions, and correcting for any stray fields in the trap.

Chapter 3 presents the structure of the strontium ion and the theory behind depletion, quantum jumps, and temperature measurements. In this chapter, one can find calculations and predictions showing the data we expect to see when the experiments are run.

Chapter 4 describes a first attempt at building a laser with sufficient frequency stability to observe the desired effects. Section 4.1 provides a theoretical background of the important optical components used in constructing the setup. Section 4.2 presents the design for a dual-laser system, and Section 4.3 describes its construction. Stability results are presented in Section 4.4.

Chapter 5 details the design and construction of a more stable laser than the one described in Chapter 4. The important differences and expected performance improvements are highlighted throughout the chapter. Section 5.3 gives the stability measurements of this new red laser.

Chapter 6 presents experimental results. Using the laser constructed in Chapter 5, we show our depletion, quantum jump, and temperature measurement data. Additionally, we describe the setup of each experiment and compare the results to the theoretical predictions made in Chapter 3.

1.3 Contributions to this work

This work was performed in Prof. Isaac Chuang's laboratory at the MIT Center for Bits and Atoms. This project is part of an ongoing, long-term effort to realize large-scale quantum computation in ion traps.

Robert Clark, Jaroslaw Labaziewicz, and Kenneth Brown all assisted me in constructing the laser system introduced in Chapter 4. Several of the electronic components necessary to operate the laser were built by Clark, and Labaziewicz designed the software and hardware used for stabilizing the laser via electronic feedback. I fabricated the electronic feedback circuits designed by Labaziewicz, built and stabilized two external cavity diode lasers, and set up various locking and optical breadboard schemes. For each setup, I measured the stability to determine if it would be sufficient for our experiments (see Sec. 4.4).

The design and construction of the monolithic laser described in Chapter 5 was spearheaded by Labaziewicz. The idea was inspired by a setup employed by Prof. Kazuhiro Hayasaka of the Kansai Advanced Research Center in Japan. Labaziewicz and Chuang developed software to interface with an FPGA chip and lock the laser. I aided in the monolaser construction and testing process by building the ECDL and optics and performing some simple debugging.

The linear Paul trap used in these experiments was designed and fabricated in Japan by Prof. Shinji Urabe's group at Osaka University. Brown designed much of the vacuum chamber mounting system, and Labaziewicz was primarily responsible for cleaning and installing the trap.

While Labaziewicz was refining the monolaser design, Clark taught me the ion trapping process. From then on, Brown and I typically worked together to trap ions for experimentation. Using the monolaser, Brown, Labaziewicz, and I were able to collect the experimental data presented in Chapter 6.

Chapter 2

Ion Trapping

Ion traps have proven themselves to be an important tool for research in experimental atomic physics. Since their development, ion traps have allowed researchers to make very precise spectroscopic measurements [3, 4, 5], perform fundamental tests of quantum theory [6, 7, 8], and determine the masses of various atoms and molecules to very high accuracy [9, 10]. Additionally, several groups have demonstrated quantum information processing and have implemented quantum algorithms on small numbers of ions [11, 12], providing a promising avenue for large-scale quantum computation.

There exist several different mechanisms for trapping ions. In general, charged particles may be trapped by electric and magnetic fields. However, as was first shown by Samuel Earnshaw [13], static electric or magnetic fields alone cannot provide confinement in three dimensional space. This arises directly from Laplace's equation, $\nabla^2 V = 0$. For any local minimum, the potential in the surrounding region would be harmonic for small displacements: $V = ax^2 + by^2 + cz^2$. Taking $\nabla^2(ax^2 + by^2 + cz^2)$ gives $a + b + c = 0$, implying that the potential cannot be simultaneously attractive (or repulsive) in all 3 directions.

In 1936, Penning proposed a way to circumvent this restriction by designing a trap with superposed electric and magnetic fields [14]. Two decades later, Wolfgang Paul presented an alternative approach involving oscillating electric potentials to confine the ions [15, 16, 17]. Since the work in this thesis was performed exclusively in a Paul trap, we will now examine the theoretical foundations and operation of such traps.

2.1 The Linear Quadrupole Paul Trap

Paul traps use radio-frequency (rf) fields to create a quadrupolar trapping potential. In his original paper, Paul presented a geometry involving a ring and two endcaps to generate a stable trapping point at the center of the ring. Since Paul's initial design, various new geometries for trapping ions with rf fields have been suggested, including the linear quadrupole trap [18, 19]. This design is comprised of four rods; two provide the rf voltage, while the other two are grounded (see Fig. 2.1). Segments on the ends of the rods may be biased to provide axial confinement. As opposed to the original Paul traps that contained only one stable point, linear Paul traps provide a line of stable points along the central axis, permitting a chain of ions to be trapped and cooled.

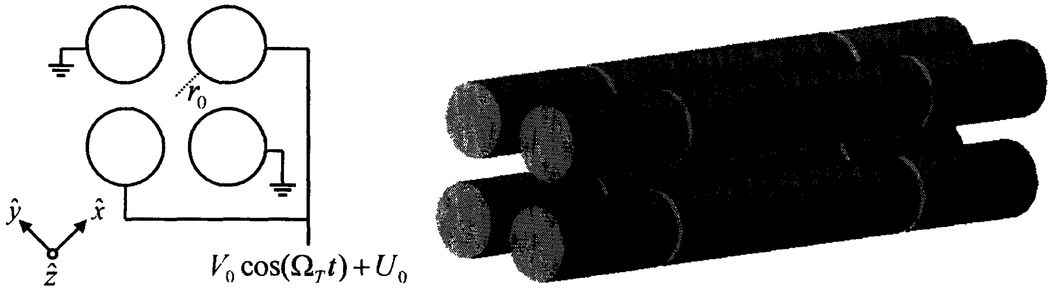

Figure 2-1: Schematic of the linear Paul trap. *Left*: end view of the trap. Two opposing rods carry a potential $V = U_0 + V_0 \cos(\Omega_T t)$, where V_0 is the zero to peak amplitude of the rf voltage and U_0 is a DC bias. The other pair of rods are held at ground. Note also the coordinate system: $\hat{x}$ and $\hat{y}$ point radially, while $\hat{z}$ points axially. *Right*: three-dimensional view of the trap. The outer segments of the rods (endcaps) are held at positive DC voltage.

To generate a purely quadrupolar field along the central trap axis, it is necessary for the four rods to be shaped like hyperbolas. Fortunately, calculation shows that alternate geometries, such as round or knife-edged rods, can produce quadrupolar fields to very good approximation [20]. As a result, most modern traps use these constructions due to ease of fabrication and lower costs.

The positive, static voltage applied to the endcaps prevents the ions from leaking out of the trap axially. Let us now consider the behavior of the potential in the radial direction only. The most general quadrupolar potential can be written:

$$\Phi_{x,y} = A(\lambda x^2 + \sigma y^2) \tag{2.1}$$

Substitution into Laplace's equation gives:

$$\begin{aligned} \nabla^2[A(\lambda x^2 + \sigma y^2)] &= 0 \qquad (2.2) \\ \lambda + \sigma &= 0 \qquad (2.3) \end{aligned}$$

As we expect, if the potential is attractive along $\hat{x}$, it is repulsive along $\hat{y}$ (and vice versa). The potential forms a saddle point along the center of the $x-y$ plane. Clearly, ions will escape along the $\hat{y}$ direction after a short time. However, as we will see, the ions can be confined if we rotate the potential at some frequency Ω_T. Including the possibility of a DC bias U_0, we may write the radial potential as:

$$\Phi_{x,y}(t) = \frac{1}{2}\left(U_0 + V_0 \cos(\Omega_T t)\right)\left(1 + \frac{x^2 - y^2}{r_0^2}\right) \tag{2.4}$$

where V_0 is the zero-to-peak amplitude of the rf potential and r_0 is the distance from the center of the trap to the rods. This potential is plotted in Fig. 2.2.

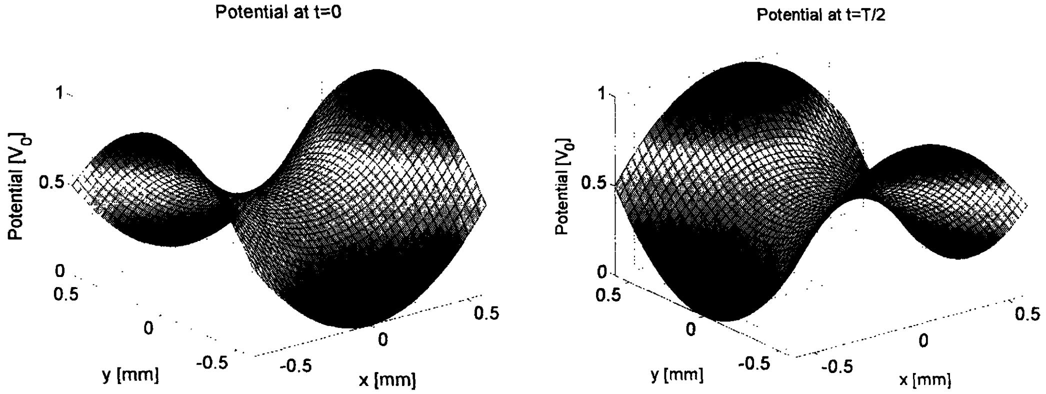

Figure 2-2: The radial potential at two points in time, with $U_0 = 0$. *Left*: at $t = 0$, the potential is attractive in $\hat{x}$ and repulsive in $\hat{y}$. *Right*: after half a period, the situation has reversed, and the potential is now attractive in $\hat{y}$.

Armed with this potential, we can now examine the behavior of ions in the linear quadrupole trap. We will first solve the complete problem of a charged particle moving in this potential, from which we can calculate the stability criteria for the trap. We will then make some approximations which allow us to gain intuition about ion motion.

2.2 Full Solution: The Mathieu Equation

Given our expression for the potential (Eq. 2.4), we may calculate the equation of motion for an ion. Since there are no cross terms (e.g. xy) in the potential, the motion in x and y can be solved independently. Due to the symmetry in the setup ($\lambda = -\sigma$), solutions for x and y should have the same magnitude, but with opposite signs. If we solve the system in the x direction for an ion with mass m and charge Q,

$$F_x = m\ddot{x} = -Q\nabla\Phi_x(t) \tag{2.5}$$

where

$$\Phi_x(t) = \frac{1}{2}\left(U_0 + V_0\cos(\Omega_T t)\right)\left(1 + \frac{x^2}{r_0^2}\right). \tag{2.6}$$

Taking the gradient,

$$\begin{aligned} m\ddot{x} + Q\left(\frac{U_0 + V_0\cos(\Omega_T t)}{r_0^2}\right)x &= 0 && (2.7) \\ \frac{d^2x}{dt^2} + \left(\frac{QU_0}{mr_0^2} + \frac{QV_0\cos(\Omega_T t)}{mr_0^2}\right)x &= 0 && (2.8) \end{aligned}$$

At this point, we can change variables to make the equation dimensionless. Let us make the following definitions (the reasoning will soon become clear):

$$\xi = \frac{\Omega_T t}{2} \qquad a_x = \frac{4QU_0}{mr_0^2\Omega_T^2} \qquad q_x = -\frac{2QV_0}{mr_0^2\Omega_T^2} \tag{2.9}$$

If we were to repeat this process along along the y direction, we would find that $a_x = -a_y$ and $q_x = -q_y$. Substituting the scaled x variables into Eq. 2.8 gives:

$$\begin{aligned} \frac{d^2x}{d\xi^2} + \frac{4}{\Omega_T^2}\left(\frac{QU_0}{mr_0^2} + \frac{QV_0\cos(2\xi)}{mr_0^2}\right)x &= 0 \qquad (2.10) \\ \frac{d^2x}{d\xi^2} + (a_x - 2q_x\cos(2\xi))x &= 0 \qquad (2.11) \end{aligned}$$

Eq. 2.11 is the exact canonical form of the Mathieu equation [21], whose solutions are well known. Since the physical goal is to trap ions, we seek stable solutions to the equation of motion (i.e. solutions bounded for all t). As demonstrated by Floquet [22], a complete solution to the Mathieu equation can be written:

$$x(\xi) = Ae^{\mu\xi}\phi(\xi) + Be^{-\mu\xi}\phi(-\xi) \qquad (2.12)$$

where A and B are constants of integration, μ is a complex constant, and ϕ is a function with period π [23]. Since ϕ is periodic, we can expand Eq. 2.12 using Fourier's theorem:

$$x(\xi) = Ae^{\mu\xi}\sum_{n=-\infty}^{\infty} C_{2n}e^{2in\xi} + Be^{-\mu\xi}\sum_{n=-\infty}^{\infty} C_{2n}e^{-2in\xi} \qquad (2.13)$$

where the C_{2n}'s represent the amplitude of each term in the Fourier series. With the periodicity of the solution now explicit, we can turn our attention to the $e^{\mu\xi}$ and $e^{-\mu\xi}$ factors that appear in Eq. 2.13. Since μ is complex, it may be rewritten $\mu = \alpha + i\beta$. We notice immediately that if μ has any real component ($\alpha \neq 0$), the trajectory is unstable since $e^{\mu\xi}$ or $e^{-\mu\xi}$ goes to infinity as ξ increases. Imposing this condition, the solution becomes:

$$x(\xi) = A\sum_{n=-\infty}^{\infty} C_{2n}e^{i\xi(2n+\beta)} + B\sum_{n=-\infty}^{\infty} C_{2n}e^{-i\xi(2n+\beta)} \qquad (2.14)$$

Applying Euler's formula ($e^{i\theta} = \cos\theta + i\sin\theta$),

$$x(\xi) = A' \sum_{n=-\infty}^{\infty} C_{2n} \cos[\xi(2n+\beta)] + B' \sum_{n=-\infty}^{\infty} C_{2n} \sin[\xi(2n+\beta)] \tag{2.15}$$

with $A' = (A+B)$ and $B' = i(A-B)$. Given Eq. 2.15, the value of β alone determines the stability of a trajectory [24]. If β is an integer, the solutions - called Mathieu functions of integral order - will be periodic but unstable. If β is a non-integer, then the solution $x(\xi)$ will be periodic and bounded; these are the stable solutions we desire.

We can now substitute the solution Eq. 2.15 into the original Mathieu differential equation (2.11) and solve for values of a_x and q_x that provide stable ion trajectories. This process is detailed thoroughly by N. McLachlan [25]. From these calculations, one can divide the $a - q$ plane into regions of stability and instability. For certain values (q,a), the trajectory in the x direction will be periodic and bounded. If we then repeat the process along $\hat{y}$ and combine the results, we will find regions in $a - q$ space where the ions are confined in both directions simultaneously (see Fig. 2.3).

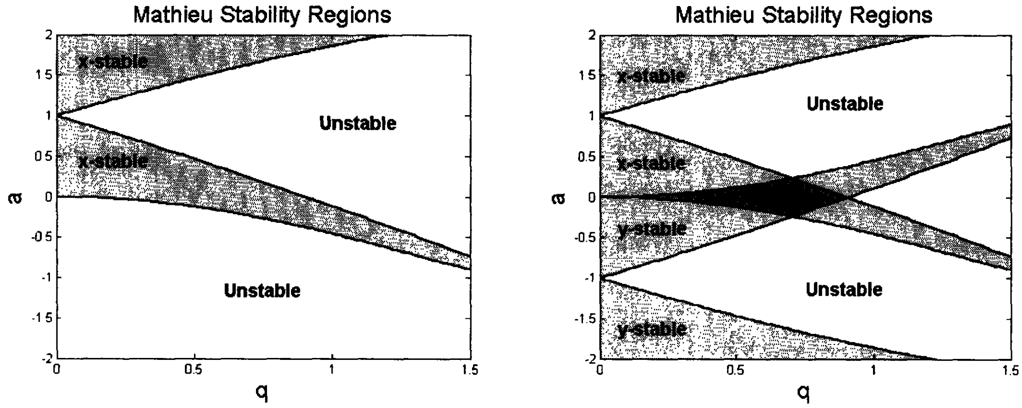

Figure 2-3: Mathieu stability regions in the $a - q$ plane. *Left*: Stability region along the x-direction (light grey). *Right*: Stability region along $\hat{x}$ or $\hat{y}$ only (light grey), and in both dimensions (dark grey).

Ions will be effectively trapped if (q,a) lies within the dark grey diamond in Fig. 2.3 (right). Recalling the definitions presented in Eq. 2.9, we can now determine the values of U_0, V_0, and Ω_T that will give a stable trap (all other factors are physical constants or geometrical measurements). Consider, as was typically done in this thesis, the case of no DC bias on the rf rods ($U_0 = 0$). Calculation shows that the maximum stable q value is .908 [25]. Recalling the definition of q, we find

$$\frac{2QV_0}{mr_0^2\Omega_T^2} \leq .908 \tag{2.16}$$

Assuming a $^{88}\mathrm{Sr}^+$ ion in a trap with $r_0 = .6\mathrm{mm}$,

$$\frac{V_0}{\Omega_T^2} \leq 1.5 \times 10^{-13}\ \mathrm{V}\cdot\mathrm{s}^2 \tag{2.17}$$

From Eq. 2.17, we find a relation between V_0 and Ω_T that determines the stability of the trap. Typical trapping values used in this thesis were $V_0 = 320$ V and $\Omega_T/2\pi =$ 17.5 MHz, giving a stable q of .16.

We have now solved the problem of trapping ions using only electric fields. By appropriately choosing the free parameters U_0, V_0, and Ω_T (and hence a and q), one can determine whether or not the arrangement will be stable. Unfortunately, Eq. 2.15 is somewhat complex, making it difficult to gain intuition about ion behavior in the trap. By applying some approximations to the system, however, we may develop insight into ion dynamics.

2.3 The Secular Approximation

Let us begin by qualitatively understanding the interaction between a trapped ion and the surrounding electric fields. By construction, there is a trapping potential oscillating at Ω_T. This oscillation can send ions into forced vibration with drive frequency Ω_T and some small amplitude. At slower time scales, the ions effectively "see" a harmonic potential in all directions. Analogously to classical simple harmonic oscillators, we expect the ion to undergo harmonic motion at some secular frequency ω_{sec}. The total motion is given by the sum of the fast, driven motion (called micromotion) at frequency Ω_T and the slow, secular motion at frequency ω_{sec}.

As before, with no bias on the rf rods, we begin by writing the equations of motion for x and y:

$$\begin{bmatrix} \ddot{x} \\ \ddot{y} \end{bmatrix} = \frac{QV_0}{mr_0^2}\cos(\Omega_T t)\begin{bmatrix} -x \\ y \end{bmatrix} \tag{2.18}$$

We qualitatively saw that the total ion motion was comprised of secular motion and micromotion. If we let $x = x_{sec} + x_\mu$ and $y = y_{sec} + y_\mu$,

$$\begin{bmatrix} \ddot{x}_{sec} + \ddot{x}_\mu \\ \ddot{y}_{sec} + \ddot{y}_\mu \end{bmatrix} = \frac{QV_0}{mr_0^2}\cos(\Omega_T t)\begin{bmatrix} -x_{sec} - x_\mu \\ y_{sec} + y_\mu \end{bmatrix} \tag{2.19}$$

At this point, we introduce the secular (or pseudopotential) approximation [26, 27]. In this approximation, the amplitude of the micromotion is taken to be small as compared with the amplitude of the secular motion (i.e. $x_\mu \ll x_{sec}$). Additionally, since we expect the drive frequency Ω_T to be larger than the secular frequency ω_{sec}, we assume that $\ddot{x}_\mu \gg \ddot{x}_{sec}$. Identical expressions hold for y. Substituting back into Eq. 2.19,

$$\begin{bmatrix} \ddot{x}_\mu \\ \ddot{y}_\mu \end{bmatrix} = \frac{QV_0}{mr_0^2}\cos(\Omega_T t)\begin{bmatrix} -x_{sec} \\ y_{sec} \end{bmatrix} \tag{2.20}$$

Solving the equation for the micromotion is now straightforward:

$$\begin{bmatrix} x_\mu \\ y_\mu \end{bmatrix} = \frac{QV_0}{mr_0^2\Omega_T^2}\cos(\Omega_T t)\begin{bmatrix} x_{sec} \\ -y_{sec} \end{bmatrix} \tag{2.21}$$

As we may expect, the trajectory due to micromotion oscillates at the rf frequency Ω_T. Additionally, the amplitude is guaranteed to be smaller than the secular motion amplitude since we can rewrite the prefactor $QV_0/mr_0^2\Omega_T^2$ as $q/2$, where q is a Mathieu parameter. For a stable trap, q cannot exceed .908, so $x_\mu < .454 x_{sec}$. Plugging our expressions for the micromotion (Eqs. 2.20 and 2.21) into Eq. 2.19,

$$\begin{bmatrix} \ddot{x}_{sec} \\ \ddot{y}_{sec} \end{bmatrix} = -\frac{Q^2V_0^2}{m^2r_0^4\Omega_T^2}\cos^2(\Omega_T t)\begin{bmatrix} x_{sec} \\ y_{sec} \end{bmatrix} \tag{2.22}$$

If we again use the approximation that Ω_T is fast compared with ω_{sec}, we can time average Eq. 2.22 over one period of rf drive. Using that $\langle\cos^2(\Omega_T t)\rangle = 1/2$,

$$\begin{bmatrix} \ddot{x}_{sec} \\ \ddot{y}_{sec} \end{bmatrix} = -\frac{Q^2V_0^2}{2m^2r_0^4\Omega_T^2}\begin{bmatrix} x_{sec} \\ y_{sec} \end{bmatrix} \tag{2.23}$$

The solutions to these simple differential equation are given by

$$x_{sec} = A\cos(\omega_x t + \phi) \tag{2.24}$$

$$y_{sec} = B\cos(\omega_y t + \delta) \tag{2.25}$$

where

$$\omega_x = \omega_y = \frac{QV_0}{\sqrt{2}mr_0^2\Omega_T} \tag{2.26}$$

are the secular frequencies in the x and y directions. A schematic of an ion's position as a function of time is plotted in Fig. 2.4.

One particularly nice feature of the pseudopotential model is that it allows approximation of the trap depth. We define trap depth as the maximum energy an ion can have before running into the rods [27]. The trap depth is calculated by treating the system classically and equating forces:

$$QD_x = \frac{1}{2}m\omega_x^2r_0^2 \tag{2.27}$$

where D_x is the depth in the $\hat{x}$ direction. Rearranging and substituting for ω_x gives

$$D_x = \frac{QV_0^2}{4mr_0^2\Omega_T^2} \tag{2.28}$$

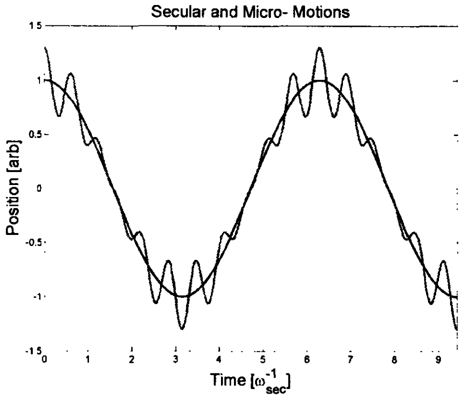

Figure 2-4: Secular motion and micromotion for a trapped ion. The large-amplitude, low frequency curve (blue) is the secular motion, while the high frequency red curve is the total ion motion. For this figure, $\Omega_T = 5\omega$ and $|x_\mu| = .3|x_{sec}|$.

If we again substitute typical experimental values ($V_0 = 320$ V, $\Omega_T/2\pi = 17.5$ MHz, $r_0 = .6$ mm), we find a trap depth of 6.4 eV. Given that we have been able to hold ions experimentally as low as 2 eV, these trapping parameters provide good confinement. Additionally, as we have seen earlier, they are well within the Mathieu stability region.

2.4 Operating the Trap

In addition to setting an appropriate rf drive frequency and voltage, several other factors must be addressed before we can trap ions. First, we need to ensure that the trap is in an ultra-high vacuum (UHV) environment. At high pressures, random collisions between the ions and background gas will impede the trapping process. Once the trap is under UHV, we need to devise a way of ionizing neutral strontium. Next, we need a way to image the ions. Finally, we should have the flexibility to compensate for any microscopic defects or stray fields in the trap that may alter the potential.

2.4.1 Vacuum System

The UHV system in this experiment was built to achieve a vacuum of 10^{-10} torr. The design is relatively straightforward (see Fig. 2.5). The ion trap chamber (Kimball Spherical Octagon, MCF450-SS20400-A) connects to the vacuum system via a 2 3/4" conflat (cf) fitting. This fitting connects to three branches. The first branch connects to a valve, permitting attachment of a rough or turbo pump. This allows us to bring the trap pressure from atmosphere down to $\sim 10^{-5}$ torr. The second branch connects to an ion pump (Varian StarCell VacIon *Plus* 40). With a pumping speed of 20 L/s, the ion pump can be used to evacuate the ion trap chamber to $\sim 10^{-10}$ torr. The third branch connects to an ion gauge (Varian SenTorr) to monitor the pressure.

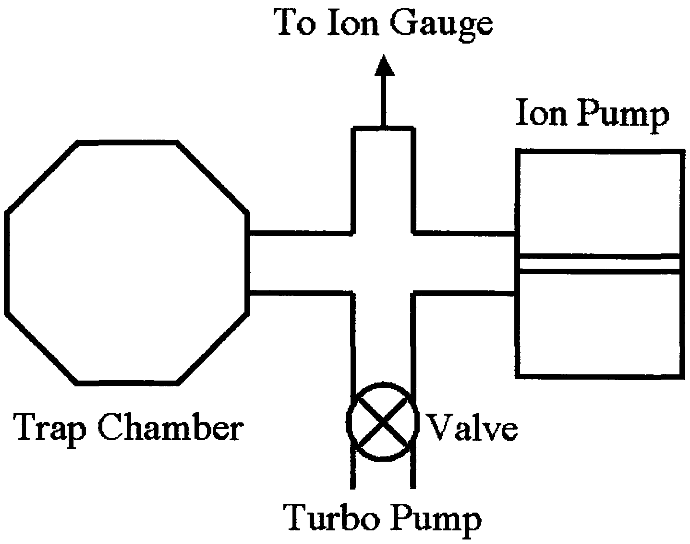

Figure 2-5: Schematic of the ion trap chamber and vacuum assembly. See text for details.

Before using the trap, it is "baked" by maintaining it at a temperature of 150°C for one week. The entire trap assembly is wrapped in aluminum foil, covered with heater tape, and wrapped with a second layer of foil. During this process, water vapor and hydrogen gas are driven off the interior surfaces and readily collected by the ion pump. Once an acceptable pressure has been reached, the heater tape and foil may be removed, and the system can cool to room temperature.

2.4.2 Ionization

In order to create ions from a neutral strontium source, an electron beam was fired at a strontium oven. The oven consists of a small piece of strontium wrapped in tantalum foil. A high current (typically 4.5 A) is passed through the foil, thereby heating the strontium within and spraying neutral atoms towards the trapping site. On the opposing side of the trap chamber sits a small coil of tungsten wire biased at -20 V. When a voltage is passed through the wire (typically 2 V), it emits a stream of electrons which ionize the strontium in the trapping region. In practice, this method is almost always effective for loading an ion cloud into the trap. A diagram of the setup can be seen in Fig. 2.6.

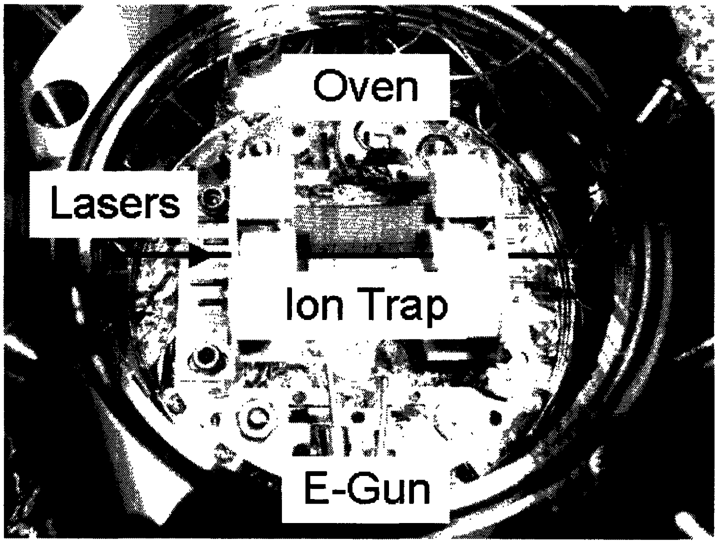

Figure 2-6: Picture of the trap chamber showing the strontium oven and electron gun. Collisions between the electrons and neutral strontium causes ionization at the trapping site.

2.4.3 Ion Detection

When strontium ions are irradiated with the proper frequency of laser light, they will absorb photons and transition to higher energy states. Soon thereafter, the atoms will fluoresce by decaying to the ground state and emitting photons. We employ two

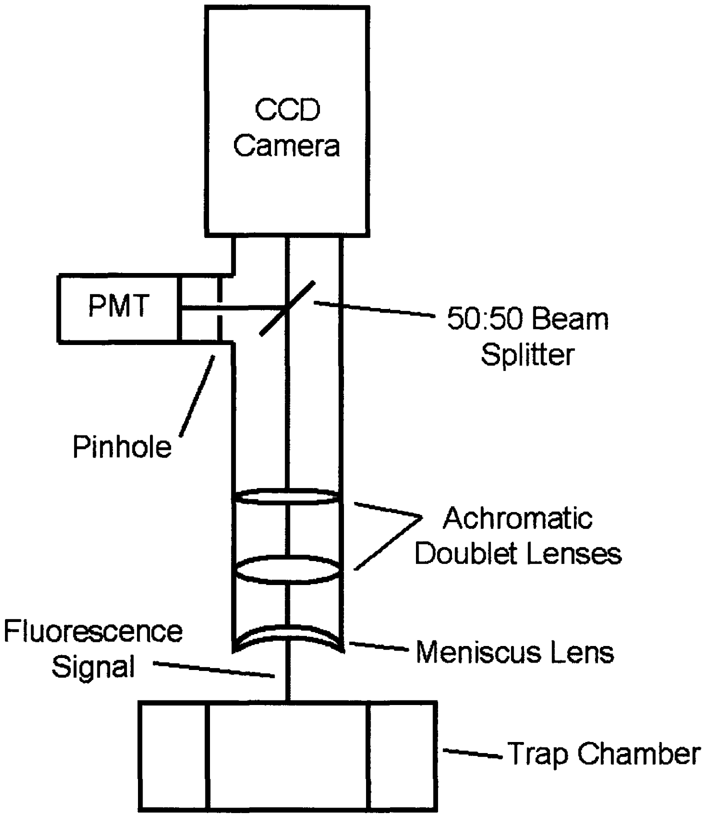
CCD
Camera
PMT
50:50 Beam
Splitter
Pinhole
Achromatic
Doublet Lenses
Fluorescence
Signal
Meniscus Lens
Trap Chamber

Figure 2-7: Optical setup for detecting and imaging ions. The ion fluorescence signal is focussed by a 100mm meniscus lens and a pair of achromatic doublet lenses (100mm and 500mm focal lengths), providing ~7X magnification. A 50:50 beam splitter sends half the signal through a pinhole and into a photomultiplier tube (PMT), while the other half is sent to a CCD camera for imaging.

different methods to detect this fluorescence. The first is a simple photon-counter setup. Light emitted from the ion trap is focussed through a pinhole to reduce scatter, then sent to a photomultiplier tube (PMT). The output signal from the PMT is directed to a lab-built FPGA controller for signal processing. This allows us to count the total number of photons received during a user-specified period of integration. Additionally, the controller can sync to an external trigger so that any periodicities in the ion fluorescence signal may be observed. A schematic of the setup is shown in Fig. 2.7.

The second method for detecting ions is direct imaging with a CCD Camera

(Princeton Instruments PhotonMax). The camera contains a silicon charge-coupled device (CCD) segmented into a grid of 512×512 light-sensitive cells. The total number of photons per frame incident on each cell is recorded, and the result is output to form an image. Software designed in lab allows us to set the integration time (100ms minimum), measure the total fluorescence intensity, digitally zoom in on regions of interest, and perform background subtraction. Images of trapped ions can be seen in Fig. 2.8.

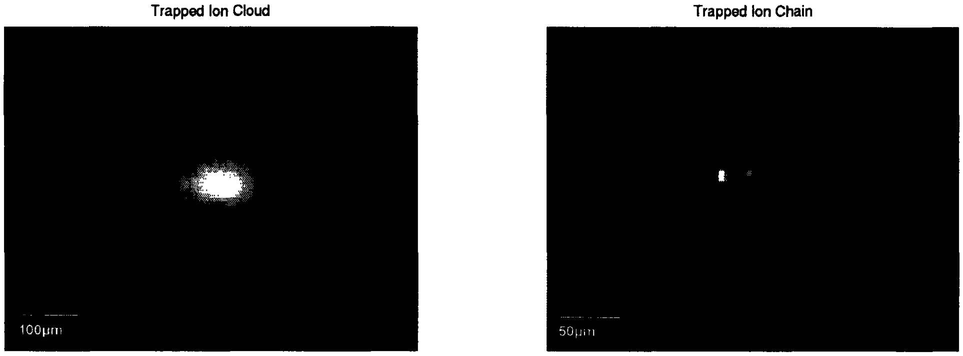

Figure 2-8: CCD camera image of trapped ions. *Left*: a large, hot cloud of trapped ions. *Right*: three individual ions lined up along the trap axis.

2.4.4 Compensation

When performing ion trap experiments, it is necessary for the ions to sit exactly along the nodal line of the rf drive. Unfortunately, trap defects and stray electric fields make this condition difficult to realize. A direct consequence of such imperfections is an increase in micromotion amplitude, which may obscure delicate spectroscopic features and cause Doppler shifts in atomic transition frequencies [28]. We therefore need to detect and eliminate micromotion.

The best way to minimize micromotion is to push the ions back to the rf null. To accomplish this, compensation electrodes with static DC biases are built into the ion trap. By including two radial biases and one axial bias, it is possible in theory to perfectly compensate the trap along all three degrees of freedom.

Both the PMT and the camera can be used to detect micromotion (see Fig. 2.9). Recalling Eq. 2.21, we expect the micromotion oscillation to occur at the rf drive frequency Ω_T. Thus by triggering the photon counter at the drive frequency, we can observe periodicities in the ion fluorescence due to micromotion. Similarly, micromotion causes an ion image to become spread out when viewed with a camera. By appropriate adjustment of compensation voltages, the oscillations on the PMT and spreading on the camera will vanish, and the ions will sit along the rf node.

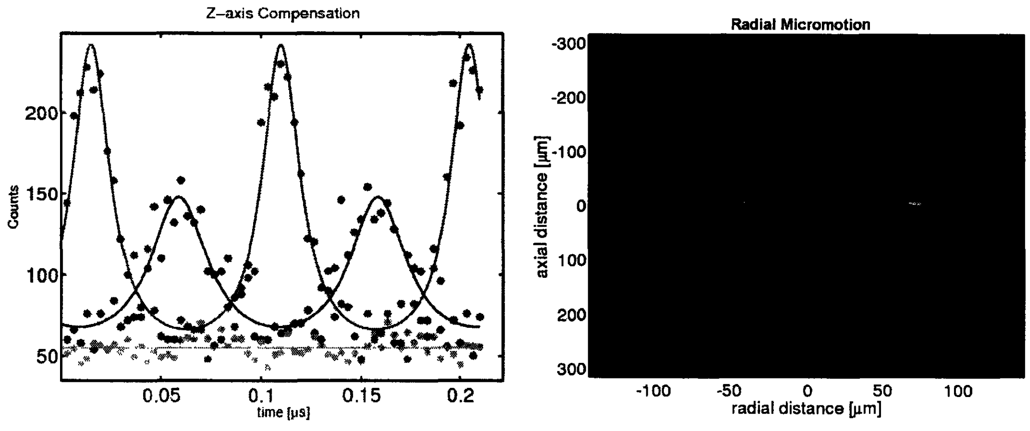

Figure 2-9: Detection of Ion Micromotion. *Left*: micromotion oscillations for endcap voltages of 7V (blue), 31V (green), and 45V (red). The green curve exhibits good compensation, while the blue and red curves show a relative phase flip. *Right*: CCD camera image of a single ion with a large radial micromotion.

2.5 Summary

In this chapter, we have discussed the theory and experimental considerations of trapping ions. Starting with a relatively simple potential, we were able to solve the equations of motion and derive stability criteria for ions in a linear Paul trap. We were also able to gain insight into ion behavior and calculate the trap depth by making some small approximations. Finally, we have discussed the construction and operation of ion traps. At this point, we are ready to consider the interesting physics that confined strontium ions can offer.

Chapter 3

The Strontium Ion

This chapter will characterize the strontium ion and describe some experiments that may be performed when ions are trapped. Although there exist many suitable atomic species for ion trapping, atoms in Group II of the periodic table are preferable. After ionization, these atoms will contain a single valence electron, and their electronic level structure is vastly simplified.

Research groups around the world work with various atoms, including $^{9}\mathrm{Be}^{+}$ [29], $^{40}\mathrm{Ca}^{+}$ [30, 31], $^{88}\mathrm{Sr}^{+}$ [32, 33, 34], and $^{111}\mathrm{Cd}^{+}$ [35]. We have chosen to trap $^{88}\mathrm{Sr}^{+}$ since all of its relevant transitions can be addressed with diode lasers, giving a compact and relatively inexpensive setup. We shall now turn our attention to the strontium energy level diagram and discuss the three important transitions.

3.1 Energy Level Structure

A partial energy level diagram for strontium is shown in Fig. 3.1. A variety of states are displayed along with their transition wavelengths and lifetimes. For our experiments, there are three important transitions: $5^2\mathrm{S}_{1/2} \rightarrow 5^2\mathrm{P}_{1/2}$ (422nm), $5^2\mathrm{P}_{1/2} \rightarrow 4^2\mathrm{D}_{3/2}$ (1092nm), and $5^2\mathrm{S}_{1/2} \rightarrow 4^2\mathrm{D}_{5/2}$ (674nm). Each serves a different purpose, and each is critical for realizing useful results.

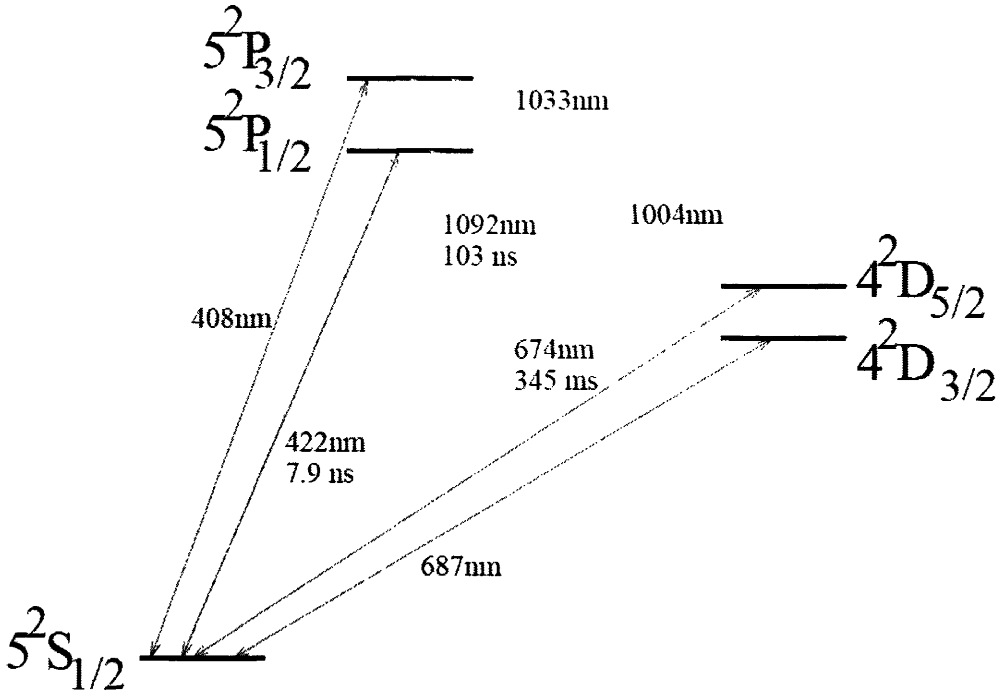

Figure 3-1: Energy level diagram for $^{88}Sr^+$. The relevant transitions are at 422nm (blue), 674nm (red), and 1092nm (IR).

3.1.1 The 422nm Transition

Before carrying out any experiments, the atoms must first be detected and cooled. The 422nm blue transition is used to accomplish both. When 422nm light impinges on a trapped strontium ion, it induces the transition $5^2S_{1/2} \rightarrow 5^2P_{1/2}$. On average, the atom will decay back to the ground state after 7.9ns, emitting a 422nm photon. This photon can then be detected with a photon counter or CCD camera (see Sec. 2.4.3).

The absorption and emission of the blue photon can also reduce the energy of the atom through the Doppler cooling process [36, 37]. Suppose the frequency of the laser is tuned slightly lower than the transition frequency. Atoms moving towards the beam will effectively "see" a higher frequency due to the Doppler effect. As a result, the atom will be on resonance, absorb the photon, and receive a momentum kick of $\hbar k$ in the opposite direction. When the atom decays back to the ground state, however, the direction of photon emission is random. Thus on average, the atom will lose $\hbar k$ units of momentum each time a photon is scattered. In this way, the motion and temperature of the ions can be reduced.

Unfortunately, there is a limit to the temperatures achievable by Doppler cooling [38]. Though photon emission on average imparts no momentum to the atom, each individual event causes a small recoil. Thus, there is a small amount of heating associated with emission, creating a Doppler cooling limit of $k_B T = \hbar\Gamma/2$, where k_B is Boltzmann's constant and Γ is the natural linewidth of the transition. For the 422nm strontium line, calculation of the Doppler limit yields T=76 μK.

Experimentally, however, the ion temperature was determined to be 660 mK - several orders of magnitude hotter than the Doppler limit (see Fig. 3.2). Two factors

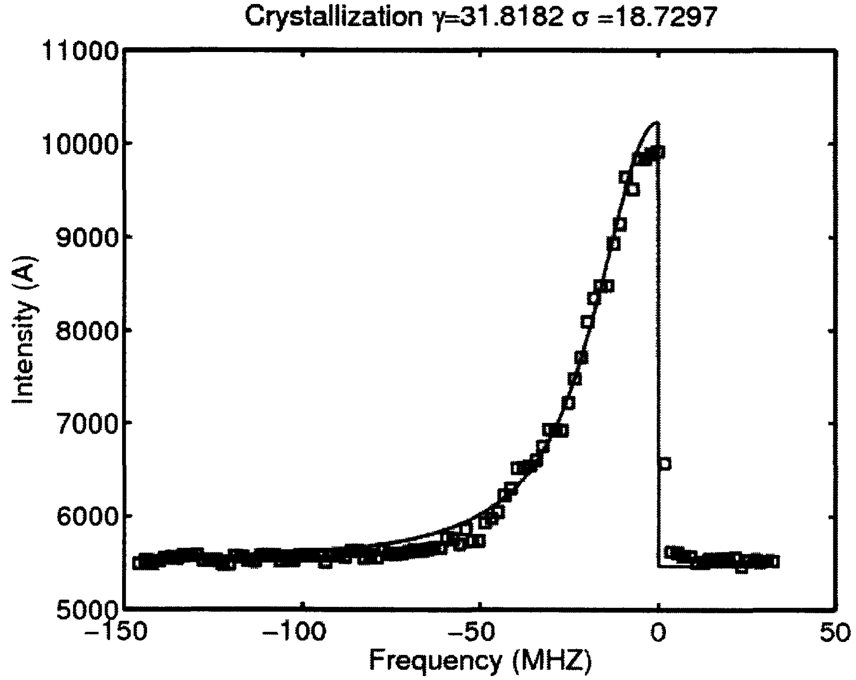

Figure 3-2: Laser-induced fluorescence at 422nm from a cold chain of ions. As the frequency is increased towards resonance, the fluorescence increases. Above resonance, however, laser heating decrystallizes the chain and the signal drops. The lineshape is a convolution of a Lorentzian (natural linewidth) and a Gaussian (Doppler broadening).

contribute to this value. First, the blue laser was simultaneously being used to cool the ions and determine their temperature. This results in an upper temperature bound, not an accurate measurement of the true temperature. Second, only one degree of freedom was being cooled. To reach the Doppler limit, all three directions must be addressed concurrently. At this point, it is difficult to tell whether or not this temperature is sufficient to observe the red laser effects since the measurement provides only an upper bound. However, as we shall soon see, the red laser itself can be used to more accurately determine ion temperature.

3.1.2 The 1092nm Transition

A strontium ion in the $5^2\mathrm{P}_{1/2}$ state will decay to the $4^2\mathrm{D}_{3/2}$ metastable state with probability 1/14. After a short amount of time, all of the strontium ions would be shelved in the $D_{3/2}$ state, and the detection and cooling processes would fail. As a result, we employ a 1092nm laser to repump the ion back to the $P_{1/2}$ state. This prevents depopulation of the ground state and allows us to continue running our experiments as usual.

3.1.3 The 674nm Transition

The 674nm line in $^{88}\mathrm{Sr}^+$ is a strongly forbidden electric quadrupole transition. Its frequency has been reported as 444 779 044 095 484.52±.10 Hz [39], and represents one of the most accurately measured quantities in all of atomic physics. Since the transition is strongly forbidden, its lifetime is large (345ms) and its natural linewidth is small (0.4 Hz). The crux of this thesis revolves around addressing this narrow line in order to probe trapped strontium ions. In particular, we wish to observe the effects of depletion and quantum jumps and accurately measure the ion temperature.

Before describing these effects in greater detail, it is useful to mention some of the other applications of the 674nm line. Recently, there has been interest in using trapped ions for optical clocks [40]. Since visible radiation is of higher frequency than the microwave radiation used for cesium atomic clocks, optical clocks will have greater time resolution and should prove to be more accurate. P. Gill *et. al.* have demonstrated a frequency standard based on the 674nm line that is three times more stable than the current cesium standard at NIST [41]. Additionally, the $5^2\mathrm{S}_{1/2} \rightarrow 4^2\mathrm{D}_{5/2}$ transition has been proposed as an optical qubit for ion trap quantum computation [42, 43]. In these schemes, the $\mathrm{S}_{1/2}$ state serves as the logical $|0\rangle$, the $\mathrm{D}_{5/2}$ state is the logical $|1\rangle$, and the 674nm radiation is used to couple the two states to each other.

3.2 Linewidth Considerations

The natural linewidth of the 674nm transition is 0.4 Hz. Experimentally, however, the linewidth appears much broader. There are two significant effects: Doppler broadening and power broadening. Doppler broadening is the dominant process; even if we were to cool to the Doppler limit, the resultant linewidth is calculated to be 125 kHz (a full derivation of the Doppler linewidth will be given in Sec. 4.1.3). Therefore, the narrow Lorentzian natural linewidth will be heavily shrouded by the broad, Gaussian Doppler profile.

If we were to employ techniques to cool below the Doppler limit, narrower linewidths could be attained. However, as the linewidth continues to shrink, one will begin to observe power broadening effects. When intense laser light irradiates an atom, it will be possible for slightly off-resonant frequencies to induce the transition [44]. This off-resonant excitation makes the absorption line appear broader than its natural linewidth. For a transition with a natural linewidth γ, the steady state solution to the Optical Bloch Equations allows calculation of the power-broadened linewidth γ' [45]:

$$\gamma' = \gamma\sqrt{1+s_0} \tag{3.1}$$

In Eq. 3.1, s_0 defines the on-resonance saturation parameter,

$$s_0 = \frac{2|\Omega|^2}{\gamma^2} = \frac{I}{I_s} \tag{3.2}$$

where Ω is the Rabi frequency, I is the laser intensity, and I_s is the saturation intensity of the transition, given by

$$I_s = \frac{\pi hc}{3\lambda^3\tau} \tag{3.3}$$

Plugging in numbers for the 674nm transition, we find that $I_s = 1.9 \times 10^{-6}$ W/m^2. Thus, for a typical 200 μW beam focussed to a 200 μm spot size, we calculate a saturation parameter $s_0 \approx 1 \times 10^9$ and a power-broadened linewidth of $\gamma' \approx 10$ kHz.

3.3 Depletion, Quantum Jumps, and Temperature Measurements

We shall now turn our attention to three of the interesting experiments that can be performed with trapped strontium ions using the 674nm transition.

3.3.1 Depletion

Consider the strontium level structure as shown in Fig. 3.1. If we irradiate the atom with only 422nm and 1092nm radiation, it will cycle primarily between the S and P states, occasionally decaying to the $D_{3/2}$ state and consequently repumped by the IR laser. Since the atom emits a 422nm photon each time it decays from the P state to the S state (on average, every 7.9ns), the atom will fluoresce quite strongly and can be easily observed.

Now consider the effects of shining all three lasers at the atom simultaneously. If the red laser is significantly more powerful than the blue, an atom in the ground state will begin to cycle between the S state and the $D_{5/2}$ state. This causes a depopulation of the $S \rightarrow P$ transition, and the 422nm photon emission rate will decrease. As a result, part of the fluorescence signal will disappear, since the imaging optics cannot detect an ion in the D state. This phenomenon is termed depletion, and should be visible in both clouds and crystals. Given a moderately stable and powerful red laser tuned to the transition frequency, depletion should be easily observable.

3.3.2 Quantum Jumps

Quantum jumps [46, 47, 48] are fascinating physical phenomena closely related to depletion. Let us again consider a strontium ion in the ground state. If we were to look for depletion, we would tune the red laser to the transition frequency, increase the red power as much as possible, and observe a dip in the fluorescence signal for the entire time the red laser was on. A simple question can now be asked: what happens when the red laser power is decreased?

In this case, the simple explanation is the correct one. We have an atom in the S state, a blue laser trying to excite it the P state, and a red laser pushing it to the $D_{5/2}$ state. Since there can only be one transition at a time, it is easy to imagine a competition between the blue and red lasers. For some value of relative laser powers, the atom will have some probability p of transitioning to the $D_{5/2}$ state, and some probability $1 - p$ of being excited to the P state. If the red laser power is then increased, so will the probability of transitioning to the $D_{5/2}$ state. If we increase the red laser power dramatically, p approaches 1, and we find ourselves in the depletion regime. Of course, if the red laser power is reduced dramatically, p approaches 0, and we see the usual fluorescence signal.

Naturally, the intermediate regime is the most interesting. Let's consider the fluorescence signal of a single ion over time. When the atom cycles between the S and P states, 422nm photons will be continuously emitted, giving some number of counts per time window. Although there will always be some statistical noise in the number of counts, we expect the value to remain relatively steady. Every so often, however, the red laser will successfully excite the $S \longrightarrow D_{5/2}$ transition. While the atom remains in this state, no blue photons can be emitted. Therefore, we expect our fluorescence signal to drop to 0. The number of counts will increase to the previous value only after the atom has decayed from the $D_{5/2}$ state and begins transitioning between S and P once more.

These random hops in the fluorescence signal are the signature of quantum jumps. Every time the single ion finds itself in the ground state, it faces a probabilistic choice to transition to either the P or $D_{5/2}$ state. Although we are able to predict the long-term fractions of time spent in each state, we can never with certainty predict the behavior in the short term. Recent work [49] has analyzed over 200,000 quantum jumps of a single strontium ion, demonstrating strongly randomized behavior of the system. For this reason, many researchers are interested in exploiting quantum jumps for random number generation.

An important theoretical problem is to determine the relative red and blue intensities necessary to observe quantum jump effects. Unfortunately, the analytical expressions describing the system cannot be cast into an enlightening or easily interpretable form [50]. Consequently, we solved the problem numerically using Mathematica.

We wish to find the probability of being in the $D_{5/2}$ state as a function of red laser Rabi frequency (i.e. power) and detuning. Setting the blue laser on resonance with a Rabi frequency of 10 MHz, we determined this probability over a range of red Rabi frequencies and detunings (see Fig. 3.3).

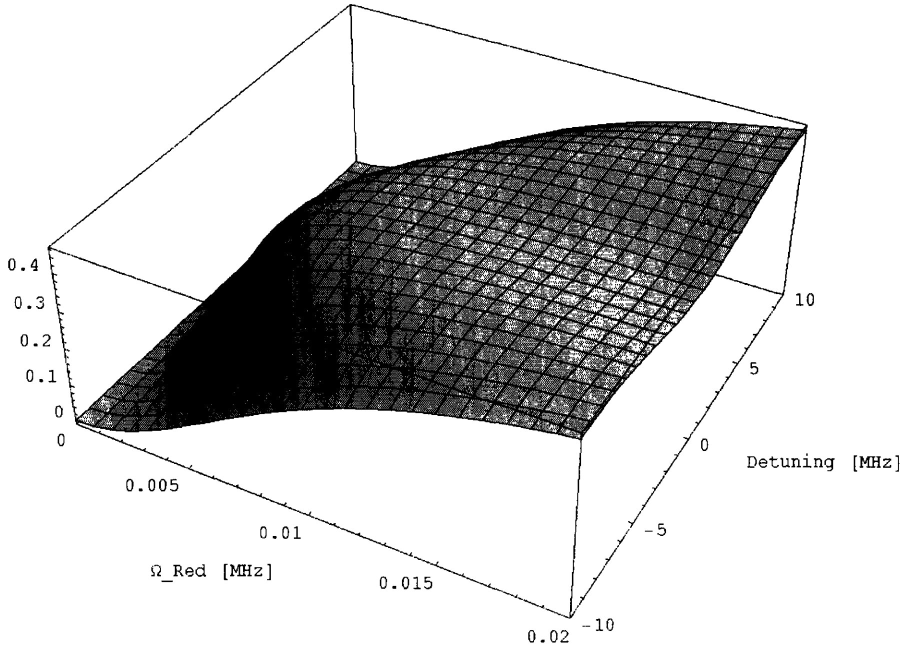

Figure 3-3: Numerical solution to the 3-level problem with spontaneous emission. The probability of being in the D state is plotted as a function of red Rabi frequency and detuning.

We see that for $\Omega_{red} > 10$ kHz, the probability of finding the atom in the D state remains relatively uniform. This corresponds to the low end of the depletion limit, where the red power is strong compared with the blue. Therefore, we would expect the best quantum jump contrast to be found in the regime where 2 kHz $< \Omega_{red} <$ 10 kHz.

We also notice that the probability varies little over a detuning range of 20 MHz. The calculated profile is directly related to the blue laser power. The blue Rabi frequency of 10 MHz causes the $S \rightarrow D_{5/2}$ transition to be broadened; as a result, the red laser can be slightly detuned and still excite the transition. The small dip around resonance is a manifestation of the Autler-Townes effect [51], which predicts a dip whose size is proportional to the strength of the blue laser. However, since we will only work with low to intermediate blue power, we will not expect to see any detuning effects. As a result, we can produce a simplified version of Fig. 3.3 by setting the detuning equal to 0 (see Fig. 3.4). This confirms that we should hunt for quantum jumps with a red Rabi frequency between 2 kHz and 10 kHz.

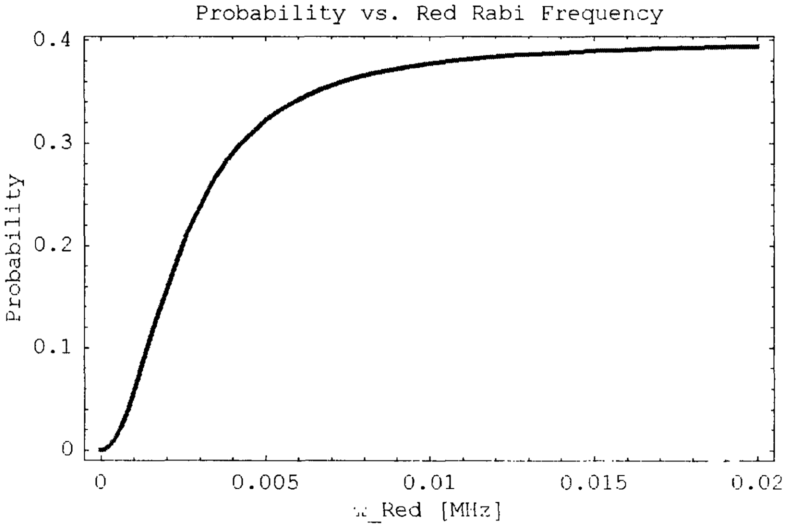

Figure 3-4: Probability of being in the D state as a function of Rabi frequency with the red laser on resonance.

To gain intuition about the dynamics of the system, I wrote a Monte-Carlo simulation of the experimental setup (see App. A). The program takes the red and blue laser Rabi frequencies as input, and outputs the simulated fluorescence signal over several seconds. Using the results of the previous analysis, I was immediately able to identify a workable range of red Rabi frequencies in which to look for jumps. Fig. 3.5 shows the output of two different simulations with slightly different red Rabi frequencies.

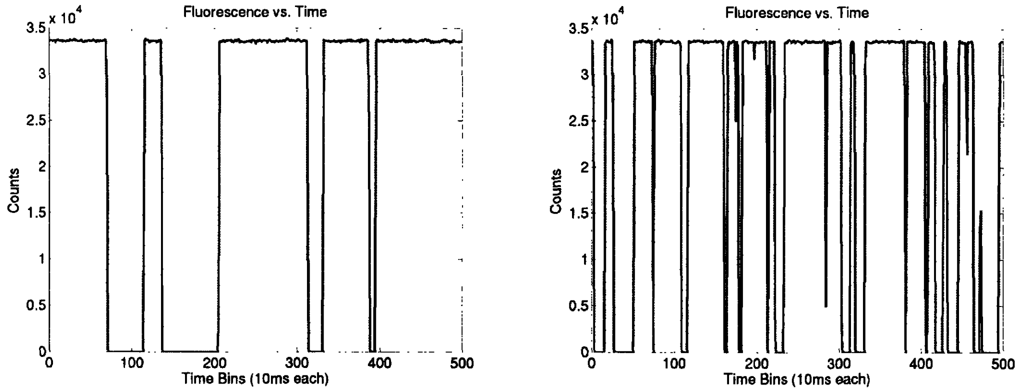

Figure 3-5: Monte-Carlo simulation of quantum jumps for two different red Rabi frequencies. *Left*: Ω_{blue}=10 MHz, Ω_{red}=4 kHz. *Right*: Ω_{blue}=10 MHz, Ω_{red}=8 kHz.

For the 5 seconds of simulated data, it is clear that there are many more quantum jumps at the higher red Rabi frequency (as expected). Re-running the simulation over a range of red Rabi frequencies, I found that quantum jumps were discernable from Ω_{red}=2 kHz to Ω_{red}=40 kHz. This is great news for our experiment, since we will expect jumps to be observed for over 2 orders of magnitude in red power.

3.3.3 Temperature Measurements

As mentioned in Sec. 3.1.1, scanning the blue laser gives an inaccurate measurement of ion temperature. To improve the measurement, we will instead seek to scan the red laser. Since the red laser does not address the cooling $S \rightarrow P$ transition, we can fix the blue laser at a single frequency (and therefore fixed cooling) while independently sweeping the red laser. This will allow us to find the Doppler linewidth of the ions, from which we can extract the temperature.

Let us consider the effects of sweeping the red laser across the 674nm transition. For red laser intensities at and above I_s and low blue power, the probability of being in the D state on resonance is 1/2. Since the natural lineshape is Lorentzian, slightly off-resonant light will be able to excite the transition. However, we can never populate the D state more than 50% of the time. Therefore, for large red power, we can expect a profile that has Lorentzian tails, but flattens out across all frequencies which would give saturated excitation (see Fig. 3.6). By reducing the power, this phenomenon becomes unimportant, and we can observe the full line.

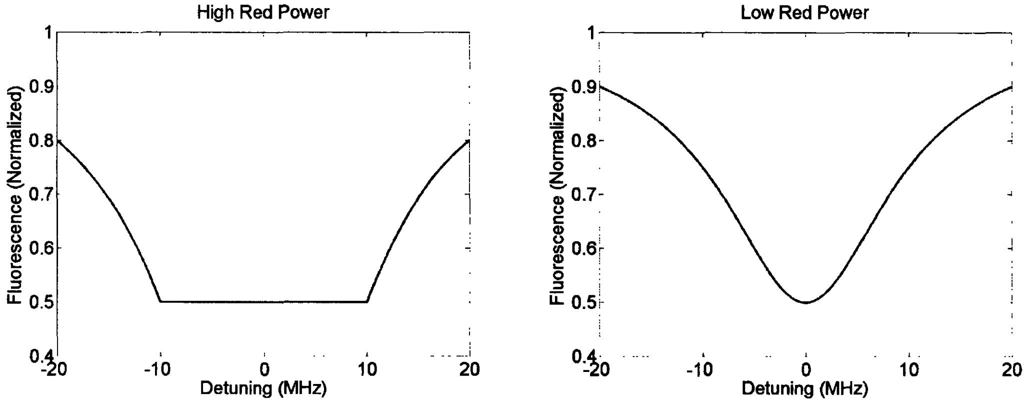

Figure 3-6: Expected spectrum of the 674nm line for high and low red laser power. *Left*: predicted fluorescence for high red power. Since the maximum population in the D state is only 1/2, we predict a flat bottom to a Lorentzian. *Right*: when the power is lowered and the amplitude of the Lorentzian is smaller, we avoid the saturation barrier and the full lineshape is recovered.

Notice, however, that the line would still be broadened to ~20 MHz by the blue laser. To circumvent this effect, the blue laser intensity must be reduced below saturation. Unfortunately, as the blue power is decreased, it becomes more difficult to image, cool, and keep an ion crystal. In all likelihood, this will be the limiting factor in making temperature measurements. Our final upper bound will depend upon how low we can set the blue power and still run the experiment.

Resolved sidebands represent a more accurate method of extracting the ion temperature. In the limit of a single, cold ion, the red laser is able to excite the $S \rightarrow D_{5/2}$ transition when its detuning is an integer multiple of the secular frequency [52]. To determine the temperature, we simply have to make a measurement of the peak amplitudes.

Let us think about the 674nm absorption spectrum of a trapped strontium ion. Naturally, when the red laser is tuned to a frequency ω_0 resonant with the transition, there will be strong absorption. However, this is not the only frequency at which we can observe a resonance. Since the atom is moving in a harmonic pseudopotential with some frequency ω_{sec}, the absorption and emission spectrum will have additional components at $\omega_0 \pm n\omega_{sec}$, where n is an integer. For these sidebands to be observed, it is imperative that the linewidth of the transition be smaller than the secular frequency. Recall that though the natural linewidth of the 674nm transition is 0.4 Hz, Doppler broadening effects will yield a linewidth of order 100 kHz (when the ion is cooled to the Doppler limit). Given that the secular frequencies of our linear Paul trap are ~1 MHz, we will be able to resolve sidebands provided our ions are cold enough.

The ratio of sideband amplitudes amplitudes can be used to determine the average number of motional quanta, $\langle m \rangle$. As derived in Ref. [53], the ratio of the upper ($\omega = \omega_0 + \omega_{sec}$) to lower ($\omega = \omega_0 - \omega_{sec}$) sideband amplitudes is given by

$$\frac{A_{upper}}{A_{lower}} = \frac{\langle m \rangle + 1}{\langle m \rangle} \tag{3.4}$$

When $\langle m \rangle$ is small, there will be a clear disparity in sideband amplitudes, and $\langle m \rangle$ can easily be determined via. Eqn. 3.4. Since the population $\langle m \rangle$ arises from a thermal distribution, we can use the standard Planck formula from statistical mechanics to write [54]:

$$\langle m \rangle = \frac{1}{e^{\frac{\hbar\omega_{sec}}{k_B T}} - 1} \tag{3.5}$$

Rearranging for temperature, we find that

$$k_B T = \frac{\hbar\omega_{sec}}{\ln\left(1 + \frac{1}{\langle m \rangle}\right)} \tag{3.6}$$

Therefore, simply by measuring the ratio of peak hights, one is immediately able to determine the average number of quanta $\langle m \rangle$ as well as the ion temperature. This represents a highly accurate method of measuring temperatures of only a few μK while leaving the system intact.

For Eq. 3.4 to give good results, we must be in the low $\langle m \rangle$ limit. If the number of motional quanta is large, then the upper and lower sidebands will have approximately equal amplitudes. In this case, we must take the ratio of the sideband to carrier amplitude:

$$\frac{A_{lower}}{A_{carrier}} = \frac{1}{2}\eta^2 \langle m \rangle \tag{3.7}$$

or alternatively,

$$\frac{A_{upper}}{A_{carrier}} = \frac{1}{2}\eta^2 (\langle m \rangle + 1) \tag{3.8}$$

where η is the Lamb-Dicke parameter, given by

$$\eta = kx_0 = \frac{2\pi}{\lambda}\sqrt{\frac{\hbar}{2m\omega_{sec}}} \tag{3.9}$$

Once η and the amplitude ratios are calculated, we again can immediately determine $\langle m \rangle$ as well as the ion temperature.

3.4 Sideband Cooling

Sideband cooling represents the next class of ion trap experiments. Although sideband cooling is slightly beyond the scope of this thesis, it deserves a few words on account of its great importance.

Sideband cooling [55, 56, 57] exploits the physics of resolved sidebands to cool ions below the Doppler limit to their motional ground state. This process eliminates

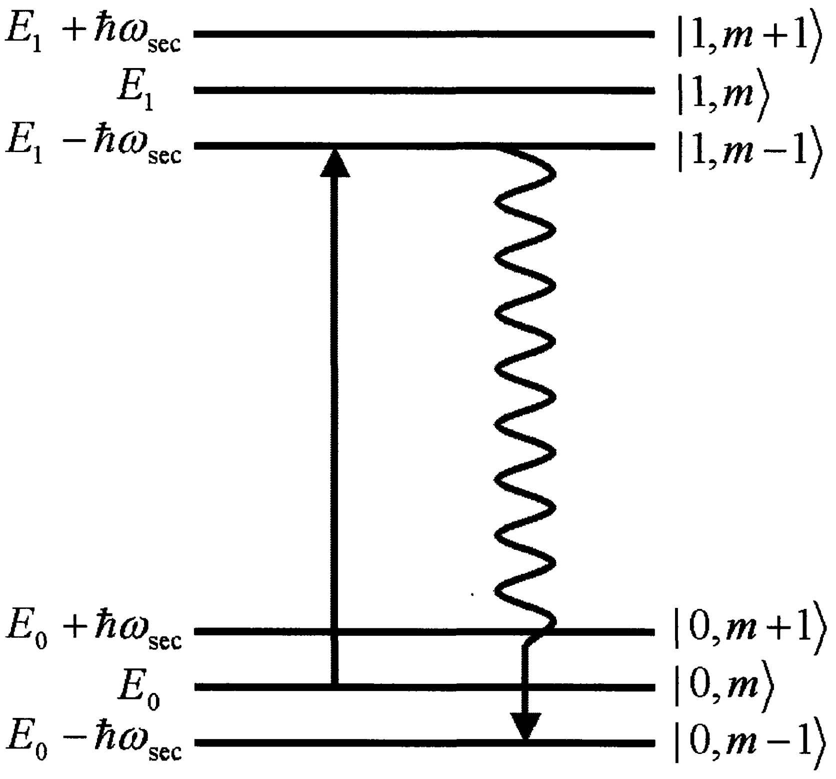
$E_1 + \hbar\omega_{sec}$
E_1
$E_1 - \hbar\omega_{sec}$
$|1,m+1\rangle$
$|1,m\rangle$
$|1,m-1\rangle$
$E_0 + \hbar\omega_{sec}$
E_0
$E_0 - \hbar\omega_{sec}$
$|0,m+1\rangle$
$|0,m\rangle$
$|0,m-1\rangle$

Figure 3-7: Energy level diagram for sideband cooling. 0 and 1 correspond to the S and $D_{5/2}$ states (respectively), and m is the number of motional quanta. After exciting an atom in the state $|0, m\rangle$ with radiation of energy $E_1 - E_0 - \hbar\omega$, the atom will on average decay to the state $|0, m-1\rangle$, losing one motional quanta in the process.

negative effects due ion motion (e.g. Doppler shifts, micromotion), and is a necessary precursor to implementation of logic gates in ion trap quantum computation.

Consider the energy level diagram in Fig. 3.7. Suppose we have an atom in the ground electronic state with some number of motional quanta m. To begin the sideband cooling process, we irradiate the atom with laser light of frequency $\omega_0 - \omega_{sec}$, where ω_0 again is the on-resonance transition frequency. After excitation, we are now in the $|1, m-1\rangle$ state. The atom then spontaneously decays, landing in the $|0, m\rangle$, $|0, m-1\rangle$, or $|0, m-2\rangle$ state with roughly equal probability. Thus, on average, the atom can be found in the state $|0, m-1\rangle$ after one cycle of sideband cooling, corresponding to the loss of one motional quanta. Repeated iterations cause the atom to eventually land in the electronic and motional ground state $|0,0\rangle$. One can verify that the atom is in its ground motional state if the lower sideband disappears, since there are no accessible lower energy states.

We can again take a red spectrum after sideband cooling to determine $\langle m\rangle$, and therefore, the ion temperature. Since the sideband cooling process is inherently designed to minimize the number of motional quanta, we expect to find the atom in the low $\langle m\rangle$ limit. Therefore, we can use Eq. 3.4 to accurately measure $\langle m\rangle$. As a check, consider the $\langle m\rangle$=0 case. According to Eq. 3.4, the ratio of amplitudes should tend to infinity. This is consistent with our prediction that the lower sideband will disappear when there are no further motional quanta left to cool.

3.5 Summary

In this chapter, we have explored the structure of the strontium ion and the various interesting experiments that can be performed when ions are confined in a linear Paul trap. We have found that phenomena such as depletion, quantum jumps, and temperature measurements should be observable given our equipment, while sideband cooling presents future experimental opportunities. We shall now proceed by detailing the design and construction of laser systems to observe these effects.

Chapter 4

An Iodine-Stabilized Red Laser

We now turn our attention to the construction of a laser system to address the $5^2S_{1/2} \rightarrow 4^2D_{5/2}$ transition in $^{88}Sr^+$. This chapter will describe a first attempt at building a laser stable enough to discern the physical effects discussed in Chapter 3. I will first present the theory behind various optical components commonly used to stabilize diode lasers. I will then detail the construction process and show experimental results of laser stability.

4.1 Theoretical Background

4.1.1 Laser Diodes

A laser diode (Sanyo DL3149-056) was used in all experiments to attain the desired 674nm wavelength (see Fig. 4.1). Diode lasers offer many advantages compared with other types of lasers: they tend to be quite easy to work with, their output amplitude is relatively constant, and their cost is surprisingly low (approximately $15 each). Unfortunately, linewidths for diode lasers are typically ~300-500 MHz [58], which is 4-5 orders of magnitude too large for these experiments. As we will soon see, however, this linewidth can be dramatically reduced through well-known techniques.

Since their inception in the 1960s, an impressive number of books and articles have been written about diode lasers [59, 60, 61, 62]. In general, lasers produce

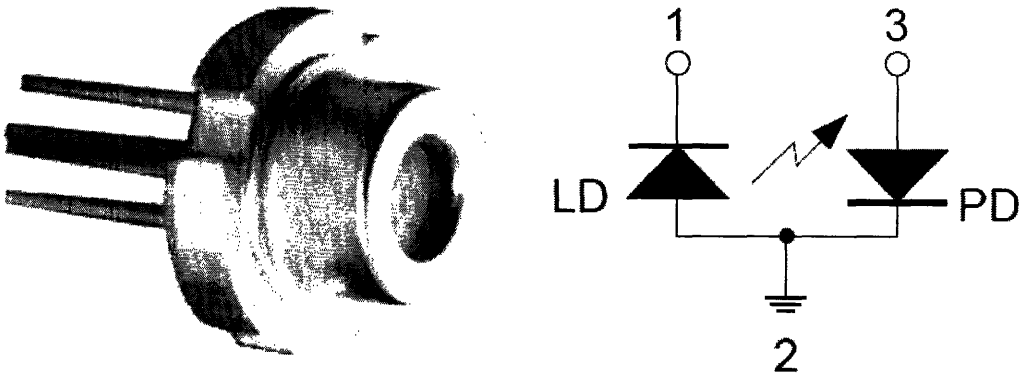

Figure 4-1: The Sanyo DL3149-056 laser diode. *Left*: photograph of the diode housing and connection pins. *Right*: circuit schematic. LD=laser diode, PD=photodiode. Pin 2 is held at ground, pin 1 is at negative voltage, and pin 3 (optional) is at positive voltage.

stimulated emission via population inversion, in which electrons are more likely to be found in excited states rather than ground states. However, since the Einstein A and B coefficients are exactly the same for absorption and emission, one cannot achieve a population inversion with only two states. Three or more levels are required.

For semiconductor lasers, population inversion is realized via valence and conduction bands at a $p-n$ junction. Because the electrons and holes reach an equilibrium in the conduction and valence bands much more quickly than they can recombine, the carriers populate the states close to the band gap. We can treat the semiconductor as a three-level system: the ground state is the valence band, the first excited state is the lower edge of the conduction band, and the third level is comprised of higher states in the conduction band.

When an injection current is applied across the $p-n$ junction, electrons and holes will recombine and emit photons with random polarizations and phases. However, above a certain current threshold, photons will be able to cause recombination by stimulated emission. This process produces a second photon that is in phase with the first, resulting in coherent light. Amplification of the effect can be achieved by placing the active material between two highly reflective mirrors.

As discussed by Dumke [63], direct band gap semiconductors are far easier to fabricate than indirect band gap semiconductors. For materials with an indirect band gap, photon emission must be accompanied by phonon emission, causing the probability of recombination to sharply decrease. To date, no laser action has been observed in indirect band gap semiconductors [64].

The diode laser used in these experiments is a direct gap AlGaInP semiconductor whose typical lasing wavelength is 670nm. Coarse wavelength tuning may be realized by varying the temperature of the diode. Colder temperatures cause the band gap to shrink slightly, resulting in a longer wavelength. Finer tuning may be achieved by varying the injection current.

4.1.2 Diffraction Gratings

Diffraction gratings are small optical components consisting of equally spaced grooves deposited on a reflective substrate. The grooves are typically spaced several hundred nanometers apart. Constructive and destructive interference effects from the closely-spaced grooves cause reflections from the grating to occur only in discrete directions, called orders. The zeroth order reflection is wavelength independent and behaves as though the grating were an ordinary mirror. All higher order reflections have a wavelength-dependent angular divergence from the zeroth order reflection.

A diffraction grating can be used to provide optical feedback to the laser diode, thereby narrowing the linewidth to ~1 MHz [65]. To accomplish this, the grating must be placed such that the first order reflection is fed back to the diode (see Fig. 4.2). This creates a resonant cavity between the back facet of the laser diode and the grating surface. In this arrangement, deemed an extended-cavity diode laser (ECDL), only discrete modes will be in resonance and lase. As the length of the external cavity increases, the laser stability improves, although the mechanical stabilization of the optical components becomes more difficult.

Construction and characterization of ECDLs has been extensively studied in detail [66, 67, 68]. In most configurations, the grating is attached to a piezo-electric crystal affixed to a kinematic mount. This allows one to vary the length of the external cavity, providing fine and coarse frequency tuning capability. The laser stability is

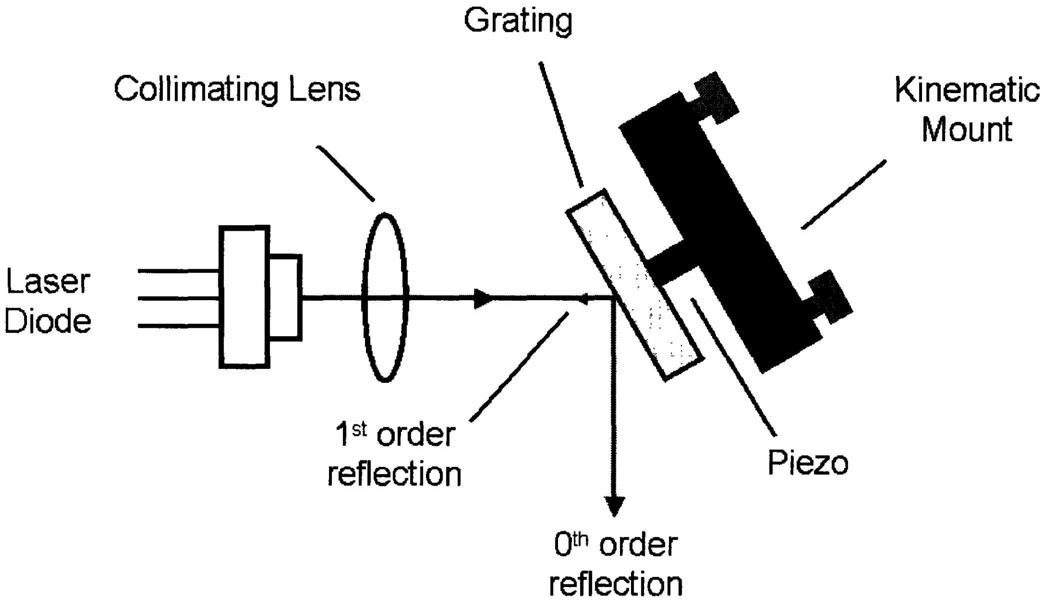

Figure 4-2: Schematic of an extended-cavity diode laser. Laser light from the diode is collimated and directed towards a diffraction grating. The zeroth order reflection is used for science, while the first order reflection returns to the diode for stabilization. Coarse tuning is performed using a kinematic mount (ThorLabs KMS), and fine tuning is accomplished by varying the voltage across a piezo-electric crystal.

highly dependent on the external cavity's length. Small variations due to vibrations, mechanical instabilities, or thermal expansion can easily destroy the sensitive feedback. Thus, the entire ECDL setup is typically housed in a temperature-controlled box and insulated from vibrations with sorbothane rubber.

Nonetheless, mechanical stabilization of the system to picometer precision over the long term is a difficult, if not impossible task. We therefore should seek ways to utilize the zeroth order output beam to further improve the laser frequency stability. Our approach was to use electronic feedback to lock the laser frequency to a fixed reference. The two most common frequency references - gas absorption cells and Fabry-Perot cavities - will now be discussed in detail.

4.1.3 Absorption Cells

Gas absorption cells contain a pure species of molecular vapor through which laser light can pass. If the frequency of the laser is on resonance with one of the molecular transitions, photons will be absorbed by the gas. If one then monitors the intensity of light passing through the cell, one will see a dip in the transmission signal on resonance. Since resonant frequencies of transitions do not change over time, they serve as outstanding frequency references.

The absorption cell used in this experiment contained I_2 and was purchased from ThorLabs (QC19100-I). The cell was fabricated from Corning 7740 quartz. The ends are slanted at Brewster's angle to prevent retroreflections, and the entire cell is placed in an oven to increase the absorption signal.

The atoms in the cell are held at some temperature T (typically 100°C) and move at some velocity v given by the Maxwell-Boltzmann distribution [69]:

$$n(v)dv = N\sqrt{\frac{M}{2\pi k_B T}}e^{-\frac{Mv^2}{2k_B T}}dv \tag{4.1}$$

where N is the number of particles, M is the particle's mass, and k_B is Boltzmann's constant. Since the atoms are in motion relative to the laser light, each one "sees" a different frequency due to the Doppler effect. The Doppler-shifted frequency is given by:

$$\nu = \nu_0\left(\frac{c+v}{c}\right) \tag{4.2}$$

If v is positive (moving towards the light), the observed frequency is slightly higher than the laser frequency, and the light appears blueshifted. Rearranging Eq. 4.2 and substituting into Eq. 4.1, we can calculate the probability distribution in frequency:

$$n(\nu)d\nu = N\sqrt{\frac{Mc^2}{2\pi k_B T\nu_0^2}}e^{-\frac{Mc^2(\nu-\nu_0)^2}{2k_B T\nu_0^2}}d\nu \tag{4.3}$$

This is simply a Gaussian with a full-width at half max (FWHM) given by

$$\Delta\nu = 2.355\nu_0\sqrt{\frac{k_B T}{Mc^2}} \tag{4.4}$$

Substituting the relevant values, we find a FWHM of 543 MHz. This Doppler broadening dominates all other lineshape considerations (e.g. power broadening, collisional broadening, the natural linewidth, etc.).

One way to circumvent Doppler broadening effects is to employ saturated absorption methods [70, 71, 72]. In saturated absorption setups, a laser beam is split and sent counterpropogating through the absorption cell. Since the beams are at the same frequency, each will excite transitions on opposite sides of the velocity distribution: one beam addresses atoms with velocity v, while the other addresses atoms with velocity $-v$. The absorption signal will slowly increase as the frequency of the laser is tuned closer to resonance, since there are more particles in this region of the velocity distribution. At the peak of the distribution, however, both beams will address the same velocity class, causing a dip in the absorption signal. This dip occurs exactly at the desired transition, but is typically over 2 orders of magnitude narrower than the Doppler-broadened linewidth. As we will soon see, narrower resonances are preferable for laser stabilization.

4.1.4 Fabry-Perot Cavities

The Fabry-Perot cavity [73, 74, 75] makes use of multi-beam interference to create sharp, wavelength-dependent resonances. In typical setups, laser light impinges on a pair of highly-reflective mirrors, and is transmitted through the etalon only for certain frequencies. Consider the geometry presented in Fig. 4.3. Two plates with reflectivities $\mathcal{R}$ and transmittances $\mathcal{T} = 1 - \mathcal{R}$ are separated by a distance d. We now investigate the effect of impinging a beam of light at some angle α [76]. If the incoming wave has some intensity I_0 and an electric field amplitude A_0, then the

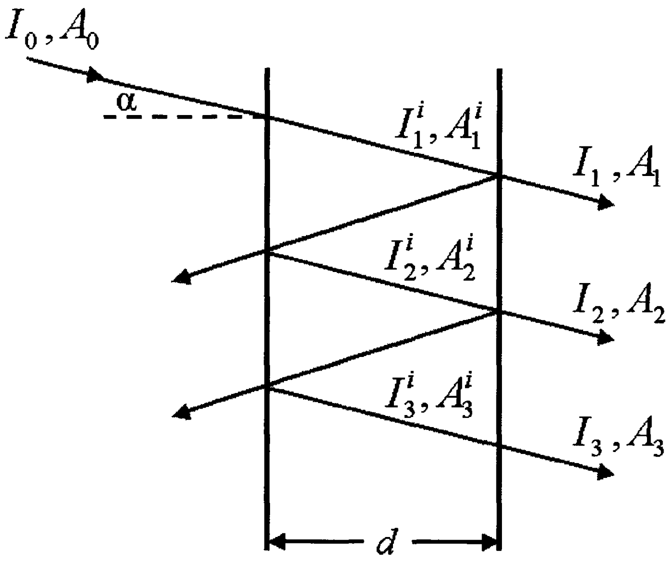

Figure 4-3: Drawing of a Fabry-Perot cavity. Two highly reflecting mirrors held a fixed distance d apart lead to constructive interference and transmission only for certain resonant frequencies.

intensity after passing through the first plate will be given by

$$I_1^i = (1 - \mathcal{R})I_0 = \mathcal{T}I_0 \tag{4.5}$$

whereas the amplitude can be written

$$A_1^i = A_0\sqrt{1 - \mathcal{R}} \tag{4.6}$$

By simple bookkeeping of reflected and transmitted amplitudes at each junction, we can find the amplitudes of the waves traversing the second plate:

$$\begin{aligned} A_1 &= A_0(1 - \mathcal{R}) \\ A_2 &= A_0(1 - \mathcal{R})\mathcal{R} \\ A_3 &= A_0(1 - \mathcal{R})\mathcal{R}^2 \\ A_n &= A_0(1 - \mathcal{R})\mathcal{R}^{n-1} \end{aligned} \tag{4.7}$$

We expect the incoming wave to be of the form $E = A\cos(kx-\omega t+\delta)$, where k is the magnitude of the wavevector and δ is a phase shift. For each internal reflection within the cavity, the wave picks up a phase shift due to the extra path length traversed:

$$\delta = \frac{2kdn}{\cos\alpha} \tag{4.8}$$

where n here is the index of refraction. Using this definition of δ and the expressions for the wave amplitudes (Eq. 4.7), we may calculate the outgoing electric fields:

$$\begin{aligned}
E_1 &= A_1\cos(kx-\omega t) \\
E_2 &= A_2\cos(kx-\omega t+\delta) \\
E_3 &= A_3\cos(kx-\omega t+2\delta) \\
E_n &= A_n\cos(kx-\omega t+(n-1)\delta) \\
&= A_0(1-\mathcal{R})\mathcal{R}^{n-1}\cos(kx-\omega t+(n-1)\delta) \qquad (4.9)
\end{aligned}$$

The total electric field at the far side of the etalon may be found by summing all the E_n's. Using that $e^{i\theta} = \cos\theta + i\sin\theta$,

$$\begin{aligned}
E_{tot} &= \sum_{n=1}^{\infty} A_0(1-\mathcal{R})\mathcal{R}^{n-1}e^{i(kx-\omega t+(n-1)\delta)} \qquad (4.10) \\
&= e^{i(kx-\omega t-\delta)}A_0(1-\mathcal{R})\frac{1}{\mathcal{R}}\sum_{n=1}^{\infty}\mathcal{R}^n e^{in\delta} \qquad (4.11)
\end{aligned}$$

The sum in Eq. 4.11 is a geometric series with $\mathcal{R} < 1$:

$$\sum_{n=1}^{\infty}\mathcal{R}^n e^{in\delta} = \frac{\mathcal{R}e^{i\delta}}{1-\mathcal{R}e^{i\delta}} \tag{4.12}$$

Substituting Eq. 4.12 back into Eq. 4.11, we find

$$E_{tot} = e^{i(kx-\omega t)}A_0(1-\mathcal{R})\frac{1}{1-\mathcal{R}e^{i\delta}} \tag{4.13}$$

We may now use that $I_{tot} = |E_{tot}|^2$ to find the output intensity:

$$
\begin{aligned}
I_{tot} &= I_0 \frac{(1-\mathcal{R})^2}{(1-\mathcal{R}e^{i\delta})(1-\mathcal{R}e^{-i\delta})} && (4.14)\\
&= I_0 \frac{(1-\mathcal{R})^2}{1+\mathcal{R}^2-2\mathcal{R}\cos\delta} && (4.15)\\
&= I_0 \frac{(1-\mathcal{R})^2}{(1-\mathcal{R})^2+4\mathcal{R}\sin^2(\delta/2)} && (4.16)
\end{aligned}
$$

Setting the angle of incidence $\alpha = 0$ and substituting for δ, we find

$$
I_{tot} = I_0 \frac{(1-\mathcal{R})^2}{(1-\mathcal{R})^2+4\mathcal{R}\sin^2\left(\frac{2\pi dn}{\lambda}\right)} \qquad (4.17)
$$

The intensity as a function of λ is plotted in Fig. 4.4.

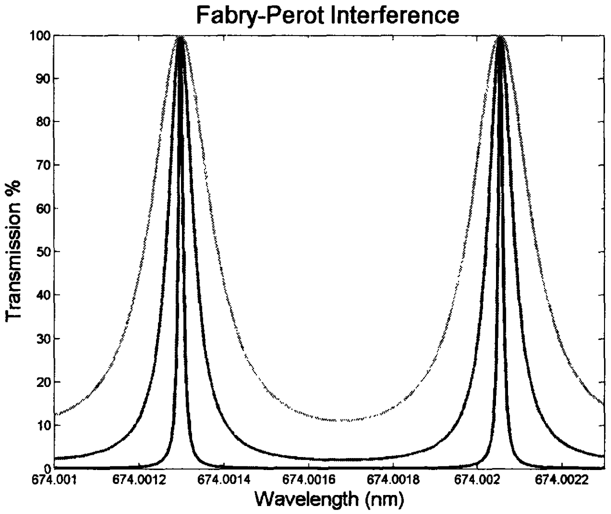

Figure 4-4: Fabry-Perot interference fringes for three different mirror reflectivities: 50% (green), 75% (red), and 95% (blue). The FWHM of the resonance peaks decreases sharply as the mirror reflectivity approaches unity.

Due to the $\sin^2$ factor in the denominator, the intensity is a periodic function of the wavelength. We notice that if $d = \frac{m\lambda}{2n}$, where m is an integer and n is the index of refraction, the intensity will remain constant for any m. Since the peaks are separated by a wavelength $\delta\lambda = 2dn$, the separation in frequency space is given by

$$\delta\nu = \frac{c}{2dn} \tag{4.18}$$

This inter-resonance frequency distance defines the free spectral range (FSR) of a Fabry-Perot cavity.

When characterizing a Fabry-Perot cavity, one often defines the finesse ($\mathcal{F}$) as the ratio of the FSR to the FWHM of a resonant peak. To calculate the finesse in terms of mirror reflectivity, we first must calculate the FWHM of the peaks:

$$\frac{I_{tot}}{I_0} = \frac{1}{2} = \frac{(1-\mathcal{R})^2}{(1-\mathcal{R})^2 + 4\mathcal{R}\sin^2\left(\frac{2\pi dn}{\lambda}\right)} \tag{4.19}$$

$$4\mathcal{R}\sin^2\left(\frac{2\pi dn}{\lambda}\right) = (1-\mathcal{R})^2 \tag{4.20}$$

$$\sin\left(\frac{2\pi dn}{\lambda}\right) = \pm\frac{1-\mathcal{R}}{2\sqrt{\mathcal{R}}} \tag{4.21}$$

Eq. 4.21 gives two solutions, λ_1 and λ_2:

$$\frac{2\pi dn}{\lambda_1} = \sin^{-1}\left(\frac{1-\mathcal{R}}{2\sqrt{\mathcal{R}}}\right) \qquad \frac{2\pi dn}{\lambda_2} = -\sin^{-1}\left(\frac{1-\mathcal{R}}{2\sqrt{\mathcal{R}}}\right) \tag{4.22}$$

We can subtract the solutions and convert to frequency units to find the FWHM:

$$\frac{2\pi dn}{\lambda_1} - \frac{2\pi dn}{\lambda_2} = 2\pi dn\frac{\text{FWHM}}{c} = 2\sin^{-1}\left(\frac{1-\mathcal{R}}{2\sqrt{\mathcal{R}}}\right) \tag{4.23}$$

Since we are interested in the case of high reflectivity, we may approximate $\mathcal{R} \gg (1-\mathcal{R})$, giving

$$\text{FWHM} = \frac{c}{2\pi dn}\frac{1-\mathcal{R}}{\sqrt{\mathcal{R}}} \tag{4.24}$$

Thus the finesse can be written

$$\mathcal{F} = \frac{\text{FSR}}{\text{FWHM}} = \frac{\pi\sqrt{\mathcal{R}}}{1-\mathcal{R}} \tag{4.25}$$

We see that simply by increasing the mirror reflectivity, we can improve the finesse (and hence decrease the FWHM of the peaks). Unfortunately, there is a practical limit of $\mathcal{F} \approx 50$ for this parallel mirror geometry. To achieve a higher finesse, the mirrors would need to be flat to within 5 nm - a challenging and expensive technical feat. A better approach is to use a slightly different geometry, in which the parallel mirrors are replaced by confocal spherical mirrors (see Fig. 4.5). This arrangement is far less sensitive to small imperfections in the mirror surface, allowing much higher finesses to be attained. Given mirrors of very high reflectivity, it is not uncommon to obtain $\mathcal{F} > 100,000$ [77, 78, 79]. The mirrors used in this experiment were 95% reflecting, giving a theoretical finesse of 61. However, since the mirrors were aligned in an invar spacer by hand, the maximum finesse achieved was ~15.

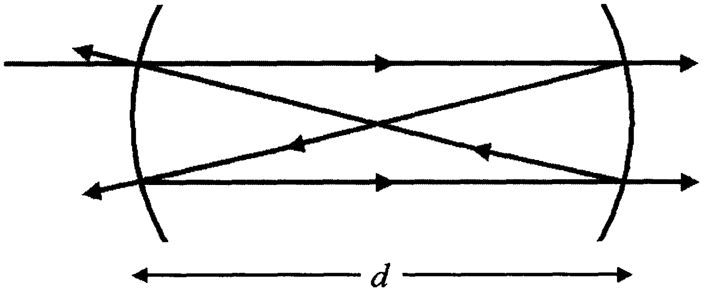

Figure 4-5: Fabry-Perot cavity in a confocal arrangement. The centers of curvature for each mirror intersect directly at the center of the etalon. Light entering slightly off axis reflects in a confocal (or "bowtie") mode, giving twice the path length of a parallel plate Fabry-Perot.

The path length for the confocal Fabry-Perot cavity is approximately twice that for the parallel plate cavity, so the expression for the FSR must be rewritten:

$$\mathrm{FSR} = \frac{c}{4dn} \tag{4.26}$$

For this thesis we used a 15 cm long confocal cavity with a free spectral range of 499.5 MHz. One of the cavity mirrors was mounted on a piezo-electric transducer disk, allowing the length of the cavity to be finely tuned. Given an experimentally determined $\mathcal{F} = 15$, we find the FWHM for each Fabry-Perot peak to be 33 MHz -

significantly narrower than the FWHM of Doppler-broadened absorption lines.

The major drawback of using Fabry-Perot cavities for laser stabilization is their long term frequency drift. The invar spacer has a non-zero coefficient of thermal expansion (1.6 ppm/°C), so temperature variations will cause a change in mirror separation. At 674nm, a .1°C change in temperature corresponds to a frequency change of 65 MHz. Analogously, pressure variations can change the effective optical path length between the mirrors. Fluctuations of 10 Pa (1/10000 atmospheric pressure) will lead to frequency shifts of 20 MHz. To reduce these instabilities, we must employ active feedback to stabilize the length of the cavity.

4.1.5 Electronic Feedback

Electronic feedback [80] allows one to stabilize the laser to a fixed frequency reference, such as a gas absorption cell or a Fabry-Perot cavity. A photodetector can be used to convert the resonance signal into an electronic signal. If the frequency of the laser should change, the voltage signal at the photodetector will change as well. Electronic circuitry detects the deviation and adjusts the injection current and ECDL grating position to bring the frequency back to the original value. We shall now investigate two methods of employing electronic feedback: side locking and peak locking.

Side Locking

Consider the resonance peak in Fig. 4.6. By combining a photodetector with an absorption cell or Fabry-Perot cavity, we can generate a frequency-dependent voltage signal. In side-locking setups, we choose a voltage V_0 along the side of the peak, corresponding to a frequency ν_0. We then construct a feedback loop to keep the voltage fixed at V_0. Suppose the laser frequency drops slightly below ν_0. This causes a small decrease in the voltage signal, which is detected by the feedback electronics. To compensate for the shift, the grating position and injection current are altered to bring the voltage back to V_0 (and hence the frequency back to ν_0). The highest possible sensitivity to changes in voltage occurs when the slope is steepest, and this

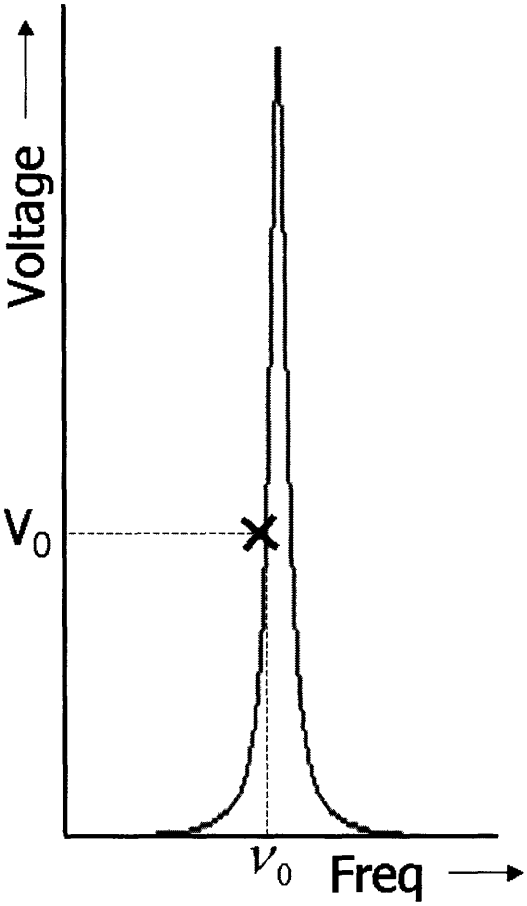

Figure 4-6: Side-locking to a voltage signal. Feedback circuitry holds the photodetector voltage at V_0, and hence the laser frequency at ν_0.

is consequently the optimal place to lock the laser.

Although side-locking techniques are relatively easy to set up, they carry several disadvantages. Side-locking is very sensitive to changes in the amplitude or offset of the voltage signal. For instance, if the temperature of the absorption cell changes, so will the transmission and photodetector voltage amplitude. The feedback loop will detect the change and vary the grating position and injection current, even though the laser frequency was not drifting. Similarly, the feedback electronics will respond to any change in background light sources (e.g. room lights, shadows, etc.). Controlling and eliminating these factors is critical for achieving stable side locks.

Peak Locking

As its name implies, peak locking can be used to stabilize a laser to the top of a resonance signal. Consider the Gaussian signal in Fig. 4.7, perhaps generated by a Doppler-broadened absorption line (the following analysis holds for other lineshapes as well). We recognize that applying side-locking methods towards the top of the curve will not be successful, since the small slope decreases the sensitivity to changes. Instead, a lock-in amplifier is used to take the first derivative of the absorption signal. The zero crossing of the derivative corresponds to the peak of the Gaussian, and is also the point where the magnitude of the second derivative is largest. We thus stabilize the laser by side-locking to the zero crossing of the first derivative.

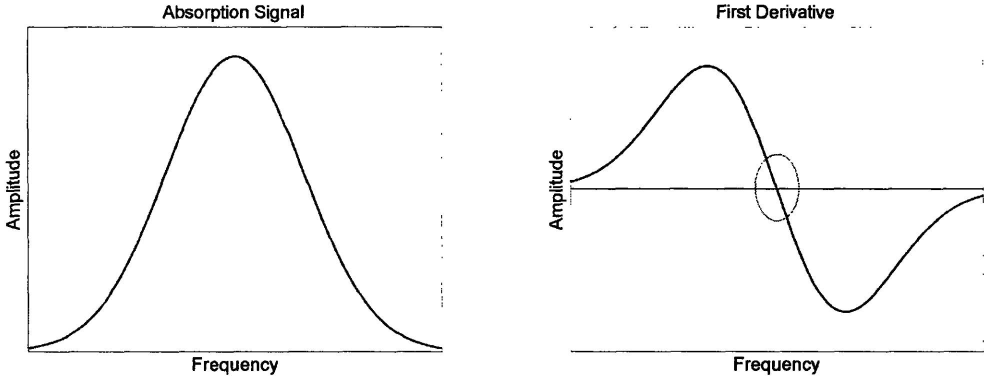

Figure 4-7: Peak-locking to a voltage signal. *Left*: a Gaussian absorption signal. *Right*: the first derivative of the signal on the left. The zero crossing (circled in red) provides the optimal locking point.

As is always the case when side-locking, steeper slopes lead to improved performance. Let us now examine the effect of linewidth on the first derivative's slope. Suppose we have an absorption signal of form

$$I = Ae^{-\frac{(\nu-\nu_0)^2}{2\sigma^2}} \tag{4.27}$$

where A is an amplitude and σ is a width parameter characterizing the Gaussian.

Taking the first and second derivatives, we find

$$\frac{dI}{d\nu} = -\frac{A(\nu - \nu_0)}{\sigma^2} e^{-\frac{(\nu-\nu_0)^2}{2\sigma^2}} \tag{4.28}$$

$$\frac{d^2I}{d\nu^2} = \left[\frac{A^2(\nu - \nu_0)^2}{\sigma^4} - \frac{A}{\sigma^2}\right] e^{-\frac{(\nu-\nu_0)^2}{2\sigma^2}} \tag{4.29}$$

To find the slope of the first derivative in the locking region, we must evaluate $d^2I/d\nu^2$ at $\nu = \nu_0$:

$$\left.\frac{d^2I}{d\nu^2}\right|_{\nu=\nu_0} = -\frac{A}{\sigma^2} \tag{4.30}$$

We see that the slope is inversely proportional to the square of the linewidth. We therefore seek the narrowest possible resonance lines to serve as our peak-locking frequency standard.

4.2 The Dual-Laser Setup

Now that we have developed an understanding of various optical components and techniques, we can design an effective laser stabilization system. Of the methods previously described, saturated absorption would provide the tightest lock since its linewidth is the narrowest (~1-10 MHz). Unfortunately, the closest atomic line to the 674nm strontium transition is 10 GHz away - too far for locking. The Fabry-Perot cavity described above can provide decently narrow linewidths (33 MHz), but is sensitive to very small temperature and pressure fluctuations.

One method to circumvent the negative aspects of Fabry-Perot cavities is to use a dual-laser setup [81], as illustrated in Fig. 4.8. Since we know that atomic transitions will not drift due to changes in temperature or external pressure, they can be used as a fixed reference to stabilize the length of the cavity. The first laser is locked to the strongest nearby Iodine transition at a frequency of 444973.5 GHz [82]. This locked laser is then directed through the Fabry-Perot cavity. High voltage is applied to the piezo so that the incident light is resonant, and a feedback loop locks to the

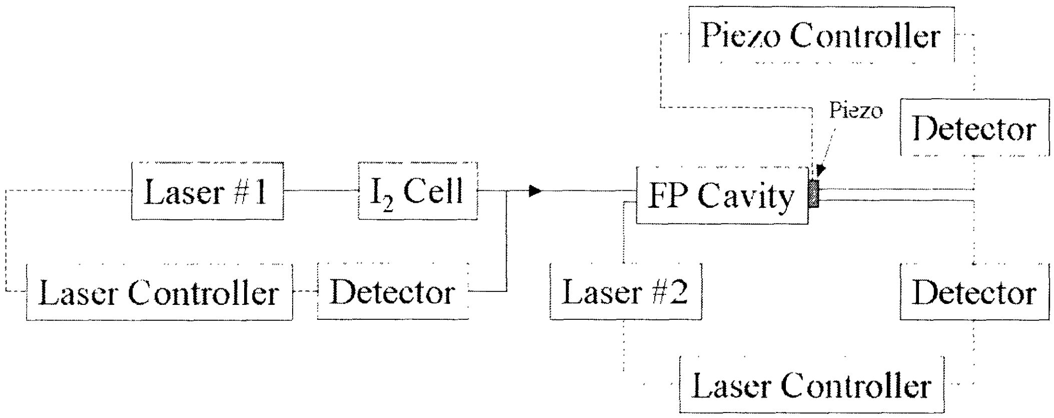

Figure 4-8: Schematic of the dual-laser setup. Laser #1 is locked to an I_2 cell, stabilizing its frequency 200 GHz away from the 674nm strontium transition. This stabilized beam is used to fix the length of the Fabry-Perot cavity by including the mirror piezo in the electronic feedback loop. Laser #2 can then be locked to the stabilized cavity and address the 674nm line.

transmission signal (and hence locks the length of the cavity). Should the temperature or pressure change, the piezo will expand or contract to offset the effect. With the length stabilized, a second laser can be directed through cavity, peak locked using a second set of feedback electronics, and sent to the ion trap.

4.3 Laser Construction

We now seek to construct a laser system following the plan outlined in Section 4.2. This section will detail the process of building the ECDLs and optical breadboards necessary to realize the dual-laser design.

4.3.1 Building an ECDL

Two extended cavity diode lasers (ECDLs), tuned to 444779.0 GHz and 444973.5 GHz, are required for this system. An ECDL has three important subassemblies: the baseplate and housing, the diode mount and collimating lens, and the grating/piezo fixture. We expect the output of the ECDL to provide a collimated beam that lases in a single mode, maintains a stable power amplitude, and has a linewidth on the order of 1 MHz. I shall now describe the construction of an ECDL fashioned from readily available components.

Baseplate and Housing

The baseplate and housing of the ECDL provide a closed box for the laser diode and optics. This creates a contained environment for temperature stabilization of the diode as well as vibrational and electrical isolation. Both the baseplate and clear acrylic housing were custom-designed to fit our purposes. Two photographs of the laser box can be seen in Fig. 4.9.

The baseplate consists of two machined pieces of 1/4" steel. The first piece forms the bottom of the box and includes mounting slots. A second, smaller piece sits 1/8" above the bottom and provides a platform for the laser diode, collimating lens, and grating/piezo/kinematic mount assembly. Heat-sink grease is applied to a thermoelectric cooler (TEC, ThorLabs TEC3-2.5), which is then clamped between the two steel plates. This allows us to vary the temperature of the laser box by changing the current applied to the TEC element. By varying the direction and amplitude of the current, baseplate temperatures of 10-40°C can easily be reached.

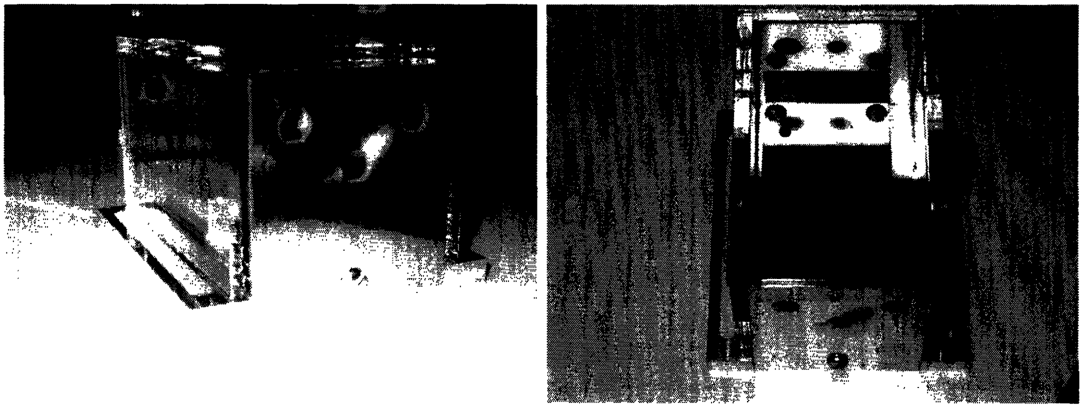

Figure 4-9: Photographs of the ECDL baseplate and housing. Laser optics are mounted on a small steel plate secured with teflon screws. A thermistor/TEC pair (not shown) are mounted on the baseplate to provide active temperature stabilization. The holes are sized to accept BNC bulkheads for internal electrical connections.

When a TEC is paired with a thermistor, the setup can be used for active temperature stabilization. A PID feedback loop uses the thermistor to determine the temperature of the baseplate and the TEC to correct for any changes. We used a Wavelength Electronics PID-1500 Temperature Controller to set the desired temperature, read the thermistor voltage, and supply the appropriate current to the TEC. Temperature stability was observed to be 5 mK over a 5 minute period. Now that we have a stabilized enclosure, we can mount the diode and collimating lens.

Diode Mounting and Collimation

We used a 5 mW Sanyo DL3149-056 diode to produce our 674nm light. The diode was secured in a mount (ThorLabs LM9F) and affixed to the steel platform. A low-noise current controller (Wavelength Electronics MPL-250) was used to power the diode, and the injection current was monitored using a digital multimeter.

Light emitted from the diode is highly divergent, so a collimating lens (ThorLabs C390TM-B) is critical for producing a useful beam. The lens is mounted in a precision-machined aluminum holder. For optimal performance, the lens must be positioned exactly on axis with and one focal length away from the point laser source.

To achieve the correct positioning, the lens holder is temporarily attached to a 3-axis mechanical stage with an extension arm. This allows the lens position to be accurately controlled in all directions until proper collimation is attained. A well-collimated beam should exhibit symmetry, limited spatial expansion, and a tightly focussed spot at the center of an elliptical envelope. When everything is optimized, the lens mount is secured to the diode mount using a fast curing epoxy. The collimating process is detailed in Fig. 4.10.

Grating Feedback and Tuning

Once a collimated beam is attained, it can be reflected off a diffraction grating to form an extended cavity. For this setup, we used a ThorLabs GR13-1850 ruled reflective grating with 1800 grooves/mm and a 500nm blaze. In order to stabilize the frequency using the ECDL configuration, the 1st order reflection from the grating must be

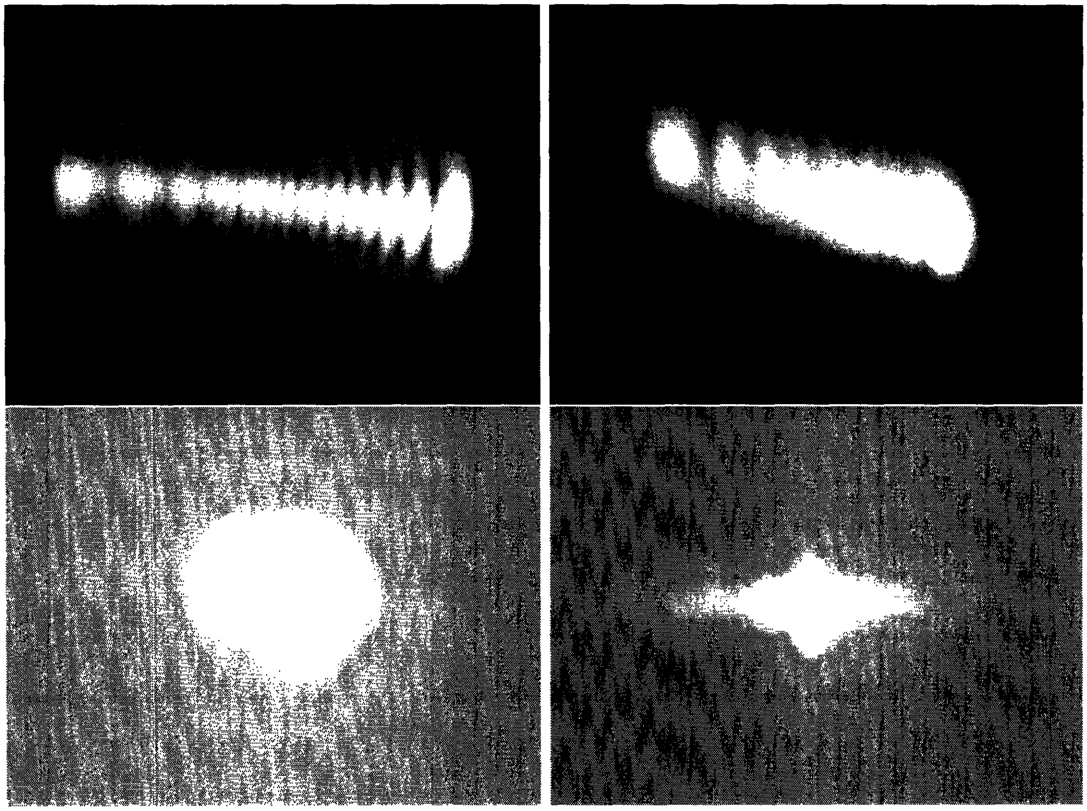

Figure 4-10: Photographs of the collimation process. *Top Left*: beam profile after coarse positioning of the lens. Interference fringes, a large size, and asymmetries indicate poor collimation. *Top Right*: changing the distance between the diode and lens produces a slightly more focussed beam, though the interference and asymmetries are still present. *Bottom Left*: better horizontal and vertical positioning eliminate many of the problems, but the spot size is still large. *Bottom Right*: small changes to each degree of freedom lead to a well-collimated beam.

directed back to the diode. To accomplish this, we first position the grating coarsely on the baseplate platform. When the angle is set properly, two spots should be visible on the grating: one is the main zeroth order reflection, while the other results from 1st order retroreflection off the diode facet. We then use the knobs on the kinematic mount to bring the two spots together, ensuring optimal feedback to the diode. A power meter at the ECDL output can be used to detect when the two beams are exactly coaligned. Small changes can now be made to the grating position (using the kinematic knobs or piezo) to provide frequency tuning up to several hundred

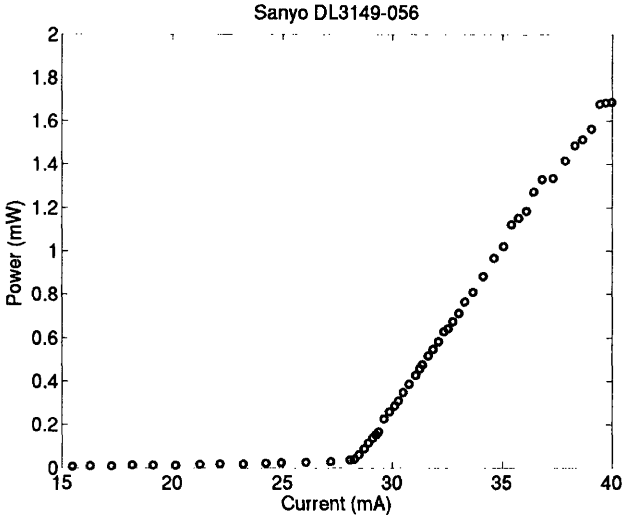

Figure 4-11: Characteristic Power-Current curve for the Sanyo DL3149-056 laser diode. The lasing threshold is at 28.3 mA, and the slope efficiency is .15 mW/mA.

gigahertz.

Strong feedback can be best detected around the lasing threshold. Without feedback, the Sanyo diode threshold current was 30.5 mA. As the feedback was strengthened and optimized, the threshold current was pushed down to 28.3 mA. Fig. 4.11 shows the characteristic Power-Current curve for the DL3149-056 diode. The threshold and slope efficiency (.15 mW/mA) are both within manufacturer specifications. With the ECDL behaving exactly as expected, we are ready to use the Fabry-Perot cavity and Iodine absorption cell to further stabilize the frequency.

4.3.2 Optical Breadboard Setups

The block diagram in Fig. 4.8 gives a broad overview of the dual-laser setup. In this section, I will present more detailed plans and pictures of the optical breadboards.

Locking to a Doppler-broadened Iodine Transition

In order to lock to a Doppler-broadened transition, we first must tune the ECDL to the proper frequency by adjusting the diode temperature, injection current, and

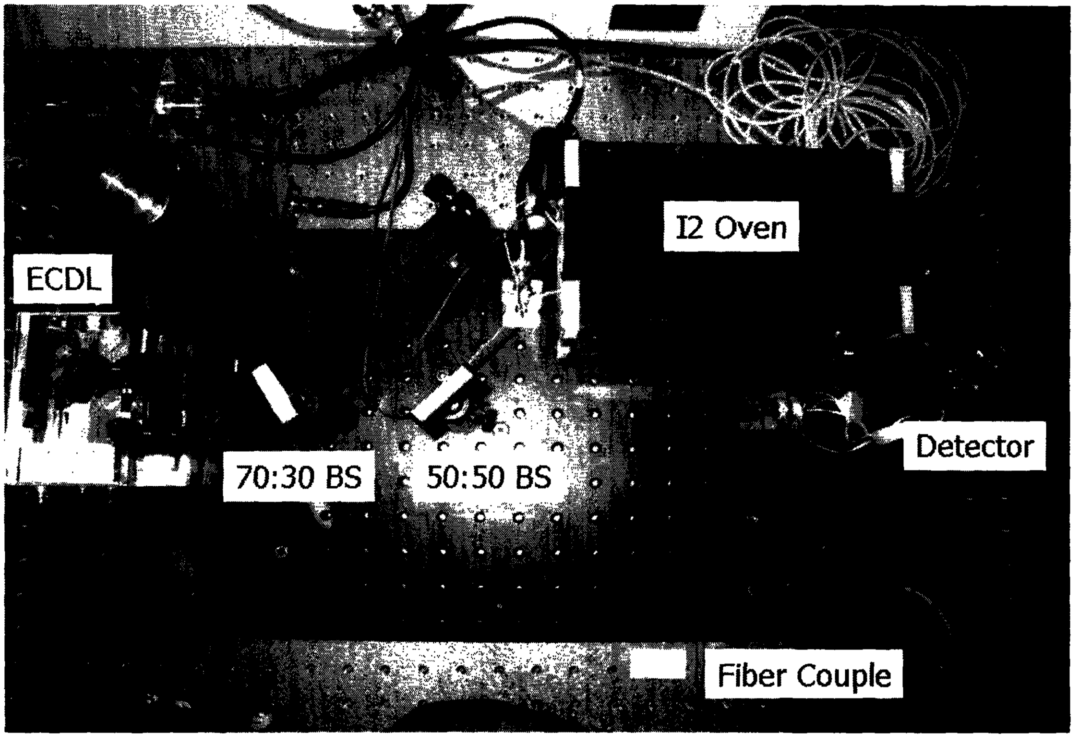

Figure 4-12: Photograph of a laser stabilized to a Doppler-broadened Iodine line. An oven is used to heat the gas cell to increase the absorption, and a balanced detector is helpful for eliminating background environmental effects. The stabilized laser beam is exported through the fiber coupler to stabilize the length of the cavity in the second laser system.

grating position. Once this is achieved, the beam can be passed through an Iodine absorption cell. A photodetector on the far side of the cell monitors the transmission signal, which will drop when the laser frequency is on resonance with the atomic line.

A picture of the laser setup can be seen in Fig. 4.12. The output beam from the ECDL first travels through a periscope to bring its height up to the level of the optics. The beam passes through a beam splitter, sending 70% of the power to the fiber coupler. The remaining 30% is split once more, with half traversing the Iodine cell and half impinging directly on the balanced detector. Typical operating powers are 2 mW out of the ECDL, 1.4 mW into the fiber coupler, and 300 μW through the absorption cell.

Locking to a Saturated-Absorption Iodine Transition

Saturated absorption setups make use of counterpropogating beams to give a very narrow signal at the transition frequency. If we are able to observe the transition, we should be able to improve the lock stability by several orders of magnitude. Fortunately, we only need to redesign the part of the setup following the 70:30 beamsplitter. Pictures and schematics can be seen in Fig. 4.13.

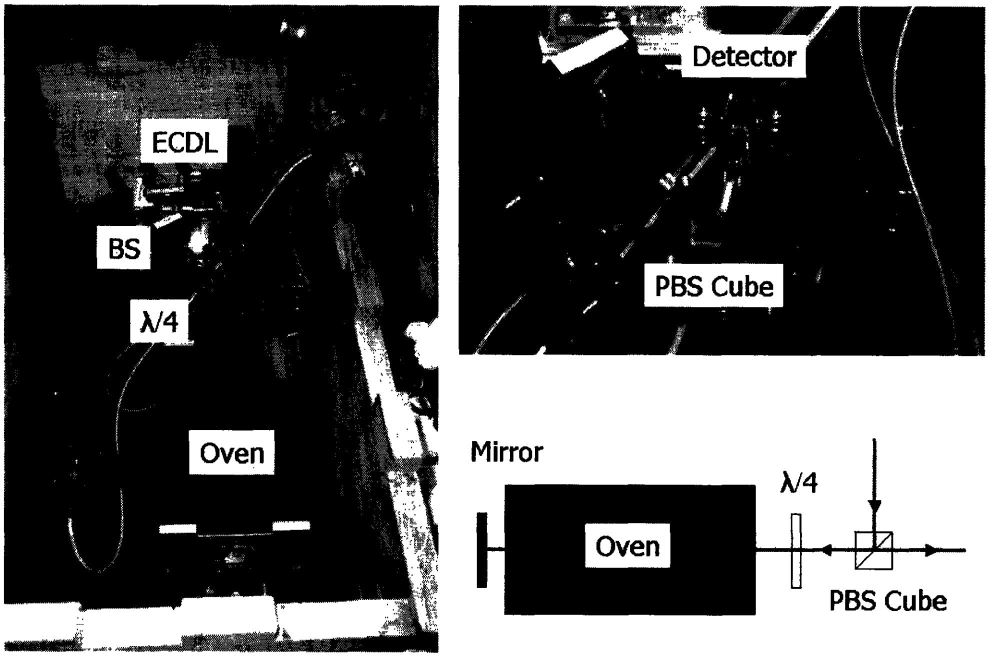

Figure 4-13: Pictures and schematic of a saturated-absorption setup. *Left*: photograph showing the ECDL, 70:30 beam splitter, quarter wave plate ($\lambda/4$), and Iodine oven. *Top Right*: photograph showing the polarizing beam splitter cube (PBS) and balanced detector. *Bottom Right*: schematic of the saturated absorption arrangement.

Light from the ECDL is incident on a polarizing beam splitter cube (PBS), which reflects S-polarized light and transmits P-polarized light. Since most of the light emitted from a laser diode is S-polarized, most of the beam is reflected towards the absorption cell. The small P-polarized part of the beam is transmitted and directed towards one of the photodiodes on the balanced detector.

The reflected light passes through a quarter wave plate ($\lambda/4$), changing the polarization from linear to circular. The beam passes through the gas cell, reflects off a mirror, and counterpropogates back through the cell. After passing through the $\lambda/4$ plate, the beam now exhibits P-polarization, and is transmitted through the PBS cube to a photodiode. In practice, we are able to pass $\sim 550\mu$W of power through the Iodine cell.

Locking to a Length-Stabilized Fabry-Perot Cavity

The second laser system is designed to lock to a length-stabilized Fabry-Perot cavity. Length stabilization is achieved via a feedback loop and a frequency reference, as detailed in Sec. 4.2.

A schematic of the laser setup is shown in Fig. 4.14. The ECDL output beam is first passed through a 90:10 beamsplitter, sending the majority of its power to the ion trap. This leaves 200 μW of power for stabilization and frequency measurement. The beam passes through a 50:50 beam splitter so that the wavelength can be monitored, and 100 μW of power are sent through the cavity. The absorption signal is detected with a photodiode (PD1).

To hold the length of the cavity constant, we import an iodine-stabilized beam from the first laser system. The beam enters through a fiber, passes through the cavity travelling to the right, and is detected by a second photodiode (PD2).

This completes the design and construction of the two laser systems. We can now perform our locking and observe the stability.

4.4 Stability Results

4.4.1 Side-locking to a Fabry-Perot Cavity

As an initial test, we seek to side-lock to a Fabry-Perot resonance and measure the frequency stability. During this phase of the experiment, the cavity is not actively stabilized, and is susceptible to temperature and pressure fluctuations. Frequency

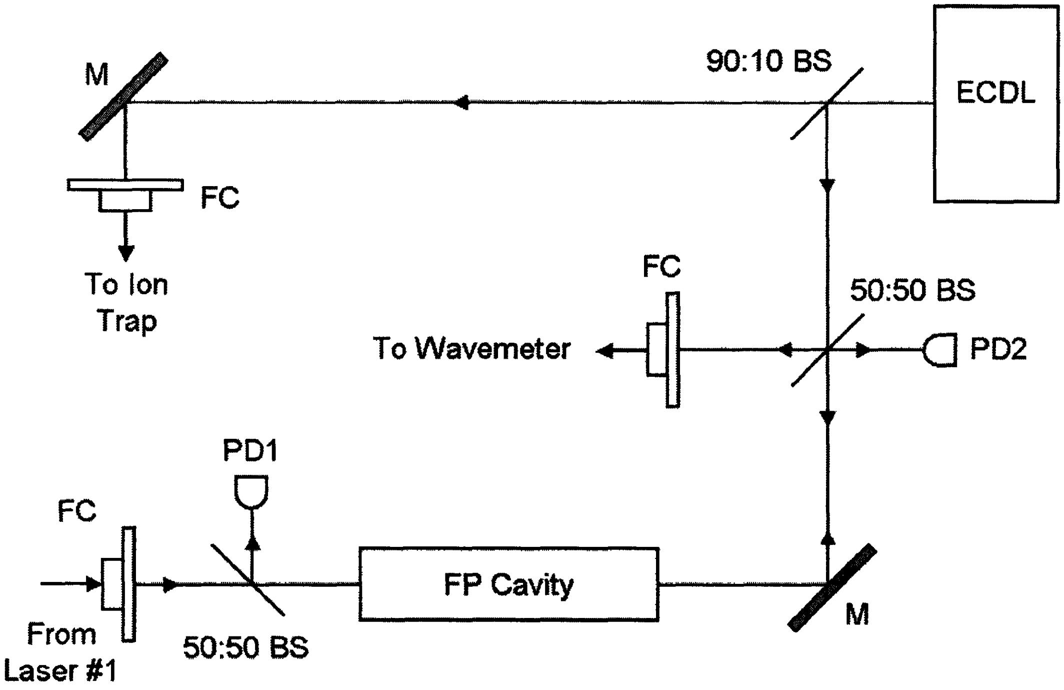

Figure 4-14: Schematic of a laser system locked to an iodine-stabilized Fabry-Perot cavity. BS=Beam Splitter, M=Mirror, FC=Fiber Coupler, PD=Photodiode. See text for details.

instabilities often exhibit two timescales: short term (t<1s) and long term (t>5m). Short term jitters are generally dependent upon the sensitivity of the lock; steeper resonance signals will improve the feedback loop's response, and the short-term instabilities will decrease. Long term frequency variations are usually related to a systematic drift caused by environmental factors. Thermal expansion, optical path length changes, and mechanical instabilities are three slowly-varying effects that will produce noticeably worse laser performance.

We use a Toptica WS/7 wavelength meter to monitor the laser frequency. When locked, we observe short-term frequency drifts of 2-3 MHz/s and a long-term frequency drift of 50 MHz/5m. Clearly, this is not stable enough to observe the effects detailed in Chapter 3. However, it is useful to take inventory of the drift sources and contributions. Recall that the invar cavity spacer has a coefficient of thermal expansion of 1.6 ppm/°C. As we found in Sec. 4.1.4., a .1°C change in temperature leads to a 65 MHz change in frequency. Pressure also plays a significant role; changes in pressure cause the optical path length between mirrors to shift. Fluctuations of 10 Pa (1/10000 atm) are enough to induce 20 MHz of drift. Other effects contribute minimally to laser instability; electronic noise, for example, accounts for ~10 kHz of drift. From this analysis, it becomes apparent that an actively stabilized cavity is necessary to improve the performance.

4.4.2 Side-locking to Iodine Transition

We now investigate the stability of a laser side-locked to an Iodine transition. The frequency drifts observed over a 5 minute period can be seen in Fig. 4.15.

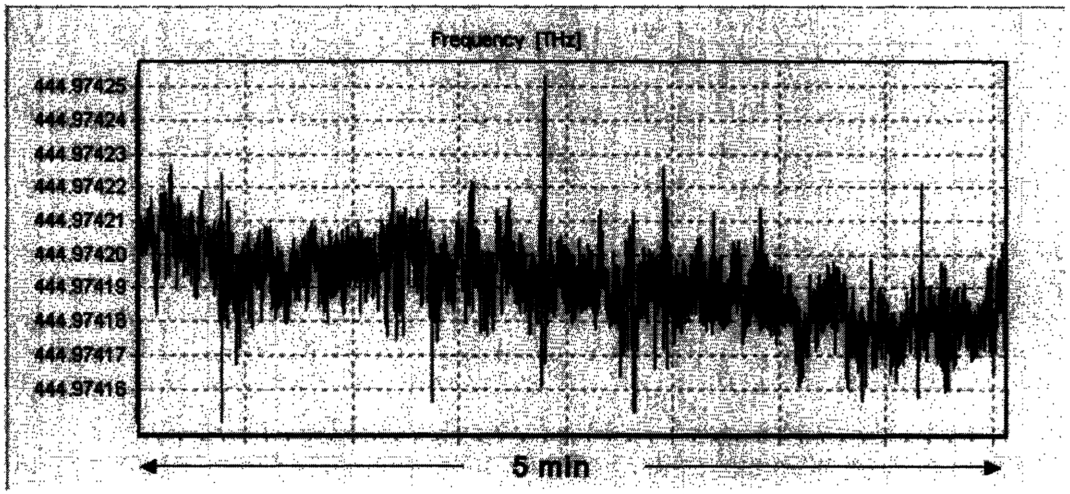

Figure 4-15: Frequency drifts of a laser side-locked to an Iodine transition.

For the side-locked laser, we observe short-term drifts of 10-15 MHz and long-term drifts of 20-30 MHz. This compares nicely with our expectations. Since the linewidth of a Doppler-broadened iodine line is much wider than that of a Fabry-Perot cavity fringe, we would predict the short term jitter to be larger when locking to the atomic transition. However, since the atomic line does not drift over time, we would expect the long-term stability to be better than when locked to a cavity resonance. Nevertheless, there is still much room for improvement.

4.4.3 Peak-locking to Iodine Transition

Since peak-locking techniques are insensitive to offset or amplitude variations in the resonance signal, we expect the long-term behavior to be more stable than side-locking. Short-term behavior is more difficult to predict, however, since the slope of the error signal depends directly on the lock-in amplifier gain settings. We again take a 5 minute frequency measurement, the results of which can be seen in Fig. 4.16.

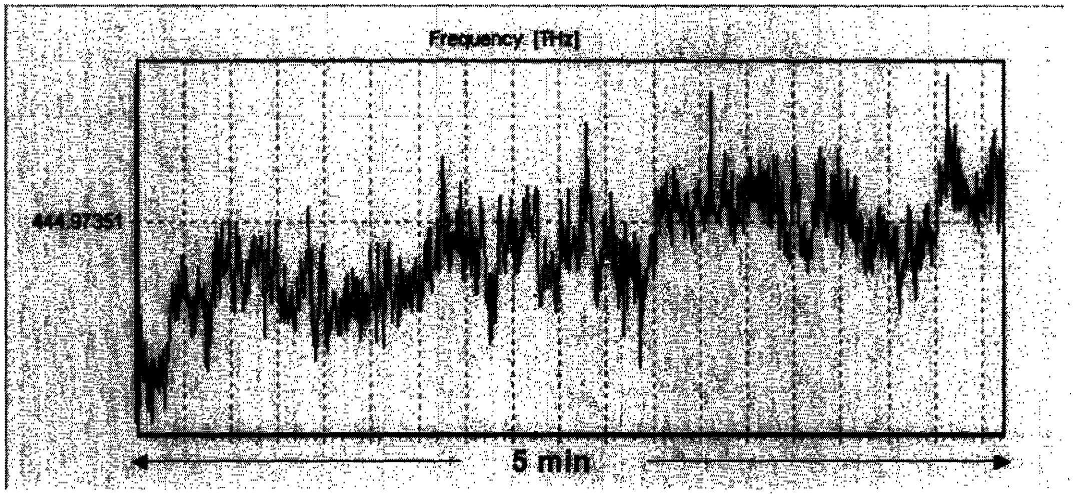

Figure 4-16: Frequency drifts of a laser peak-locked to an Iodine transition.

For the peak-locked laser, we observe short term drifts of 2-3 MHz and long-term drifts of less than 10 MHz. This is quite a nice improvement, as it approaches the frequency accuracy of the wavemeter itself. However, the instabilities of the peak-locked laser are still 3 orders of magnitude too large. We must therefore seek an alternative method for improving the setup.

4.4.4 Locking to a Saturated Absorption Line

Recalling the result of Eq. 4.30, we found that the stability of the peak-locked laser should scale inversely with the square of the linewidth. Thus, we wish to use the narrowest possible line as our frequency reference. Since saturated absorption lines are typically 2 orders of magnitude narrower than Doppler-broadened transitions, we would expect a 4 order of magnitude improvement in the stability if we could lock to such a line.

Unfortunately, after setting up the optics as described in Sec. 4.3.2, no saturated absorption signal was observed. Even with the 70:30 beam splitter removed and all 2 mW of power pumped through the absorption cell, the sharp resonance could not be found. In all likelihood, this is a direct result of molecular structure. Saturated absorption methods are only successful when the transition is closed. However, molecules contain a large number of closely-spaced rotational and vibrational levels. As a result, the majority of lines cannot be saturated, and the process fails. To be complete, all other Iodine transitions addressable by the laser diode were checked, but the resonance signal was never seen on any line.

4.5 Summary

This chapter has described a first attempt at building a laser system stable enough to observe the effects described in Chapter 3. We found that an invar Fabry-Perot cavity without active stabilization led to significant drifts in the laser frequency. While the plan to fix the length of the cavity using an iodine-locked laser was a promising idea, the stability of the reference laser was observed to be 10 MHz over 5 minutes - several orders of magnitude too large. Since saturated absorption methods proved unsuccessful, we have effectively exhausted the possibilities of this setup. To realize further improvement, we must consider a completely new laser stabilization architecture.

Chapter 5

A Monolithic Red Laser

This chapter will present a new approach to solving the laser stability problems we have witnessed in Chapter 4. As we have seen, fixing the length of a Fabry-Perot cavity to an Iodine transition gives a large instability of 10 MHz over 5 minutes. Thus, we return to the problem of eliminating temperature and pressure fluctuations in the cavity's environment. Additionally, recall that in the previous setup there was a small jitter caused by fast electronics in the feedback loop. We should seek to eliminate this effect as well. As always, we would like to achieve as narrow a linewidth as feasible.

To address these issues, we have designed and constructed a monolithic laser stabilized using resonant optical feedback and slow electronics. The laser is termed monolithic because the ECDL, beam shaping optics, and cavity are all affixed to a baseplate contained in a hermetically sealed, temperature controlled aluminum box. The vacuum-sealed box has a footprint of less than 1 square foot, and permits much better stabilization of the external environment than was previously attainable.

Resonant optical feedback techniques circumvent the use of fast electronics to lock a laser to a cavity [83]. In these setups, there is strong feedback to the diode only when the lasing frequency coincides with a cavity resonance. At this frequency, the feedback creates a small bump in the laser gain profile. Since the lasing action takes place at the peak of the gain profile, resonant feedback forces the laser to automatically lock itself to the cavity resonance. Slow electronics are still necessary to compensate for any long-term drifts, but the laser can be expected to stay optically locked for several minutes without any electronic feedback.

The structure of this chapter is similar to the structure of Chapter 4. Here, I will present the design for the monolithic laser (monolaser) and detail the special optical components at the heart of the design. I will then describe the construction, frequency tuning, and operation of the monolaser. Finally, I will show laser stability results. Experimental results using the monolaser will be presented in Chapter 6.

5.1 Monolaser Design

This section introduces a monolithic laser design that should satisfy our stability requirements. I will first discuss the design as a whole and the placement of the optical components. This will be followed by an in-depth theoretical discussion of the triangular Fabry-Perot cavity used to stabilize the diode.

5.1.1 Optical Breadboard Setup

The phrase "optical breadboard" here is somewhat of a misnomer. All of the optical components in the monolaser are secured to holes drilled in a 1.5" inch thick aluminum baseplate. Since the placement is designed prior to machining, the arrangement can be optimized without being restricted to the typical 1" optical breadboard grid. Additionally, since everything is affixed to a single baseplate, we avoid stresses and drifts caused by mismatches in the coefficient of thermal expansion across the system. Correcting for the expansion of the aluminum baseplate is a task easily handled by piezo-electric transducers and feedback loops.

Our monolaser design, inspired by K. Hayasaka [84], is shown in Fig. 5.1. Laser light is emitted from a diode, collimated with a lens, and reflected off a grating for pre-stabilization. This forms a simple ECDL configuration identical to the one described in Chapter 4. The collimated beam then passes through a set of cylindrical lenses, transforming the beam profile from elliptical to circular. A standard plano-convex lens is used to match the mode of the Fabry-Perot cavity for optimal transmittance, while a second lens is used to re-collimate the beam before exiting the monolaser.

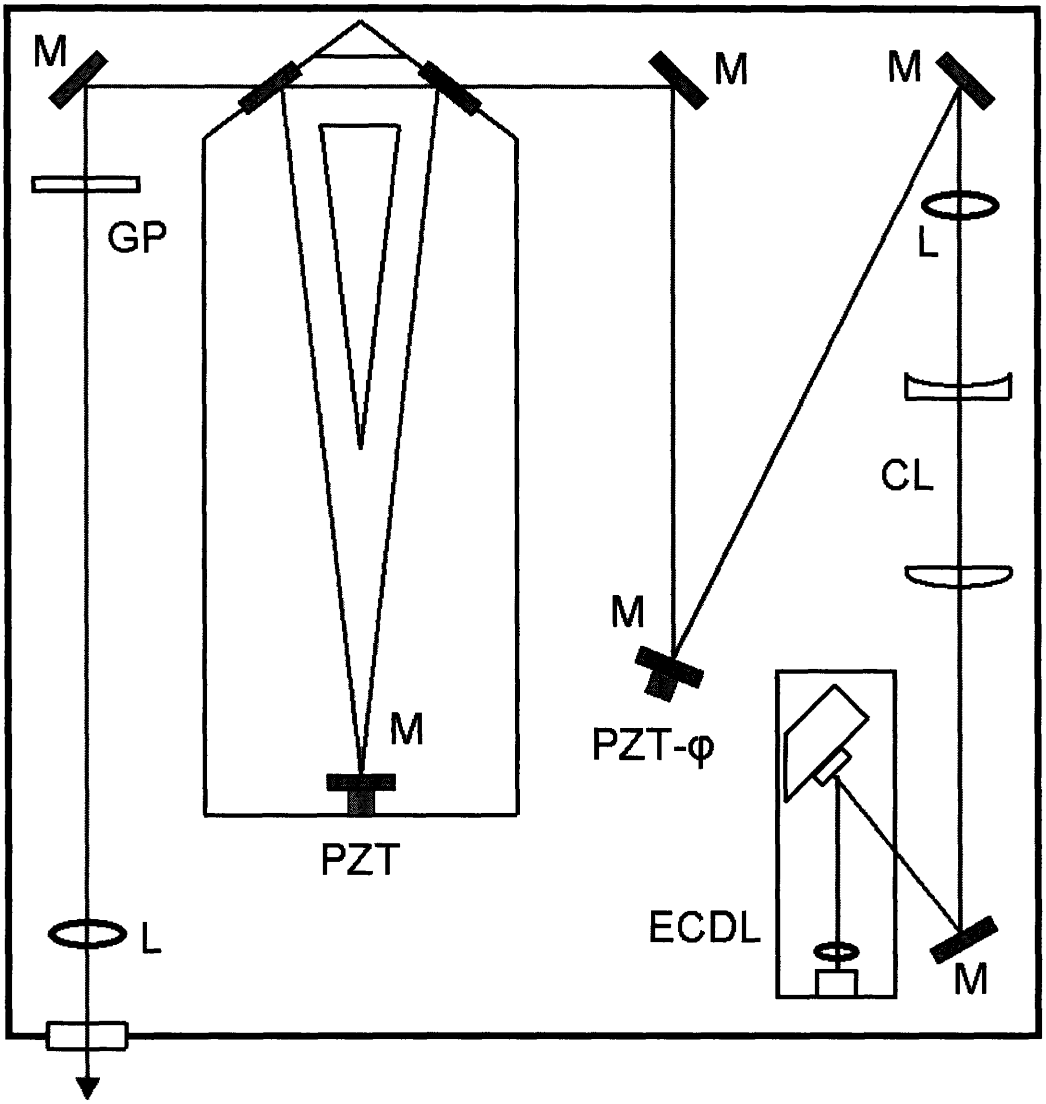
M
M
M
GP
L
CL
M
M
PZT-φ
PZT
ECDL
L
M

Figure 5-1: Optical layout for the monolithic laser. M=Mirror, CL=Cylindrical Lens, L=Lens, PZT=Piezo, GP=Glass Plate. See text for details.

We use a glass plate to reflect 4% of the power back through the cavity, off the grating, and into the diode. This allows us to provide the laser with feedback for the optical lock. Feedback will only be provided when the laser frequency matches a cavity resonance, since transmittance through and reflection back cannot exist otherwise. However, matching the cavity resonance is not a sufficient condition for attaining stable locks; we must also be mindful of the feedback phase. Consider the case where the back reflection is π radians out of phase with the outgoing light. As the beam retraces its steps, it will cause destructive interference, and the diode will see no feedback. Therefore, we need to ensure that the feedback phase differs from the outgoing phase by an integer multiple of 2π. To accomplish this feat, we attach a piezo to one of the monolaser mirrors (labelled PZT-ϕ). Changes to the piezo length allow us to change the total path length between the diode and glass plate. Thus, by scanning the piezo over a small range, we can optimize the feedback phase.

The V-shaped Fabry-Perot cavity generates the resonance signal for the optical lock and performs spatial filtering of the laser light [85]. As we will soon see, we can arrange the setup so that only a Gaussian beam (TEM$_{00}$ mode) is transmitted through the cavity. This is quite beneficial, since Gaussian beams are well-described by standard optical formulas, are easy to manipulate, and can be fiber coupled very efficiently.

The filter cavity has 3 mirrors; two are on axis with the incoming laser beam with reflectivities of 99%, while the third is a purely reflecting curved mirror attached to a piezo at the far end of the cavity (see Fig. 5.2). As before, changing the voltage applied to the piezo allows us to vary the length of the cavity. Using Eq. 4.25, we calculate the theoretical finesse of the cavity to be 300.

We now have enough information to characterize the effect of the optical lock. As demonstrated by Laurent *et. al.* [86], the linewidth of a diode laser optically locked to a cavity will be reduced by a factor of P^2, where P is the ratio of ECDL finesse to cavity finesse. Performing the calculation, we find that $P^2 \approx 10^4$. Given an ECDL laser linewidth of ~1 MHz, the monolaser should output a beam with a linewidth less than 10 kHz.

Figure 5-2: Photograph of the filter cavity.

5.1.2 The Filter Cavity

Since the filter cavity forms the heart of the monolaser, its physics deserve detailed attention. The cavity accomplishes two tasks: resonance signal production and Gaussian-mode selection. Generation of the resonance is straightforward, and the theoretical explanation is identical to that given in Sec. 4.1.4. Selection of the TEM_{00} mode is possible because the various modes of propagation exhibit different resonant frequencies [87].

To understand why this is the case, we must first develop a mathematical description of the modes inside the cavity. In general, the modes of propagation are Hermite-Gaussian functions [88]. These functions are orthonormal, complete, and satisfy the paraxial Helmholtz equation.

Let us define a rectangular coordinate system such that $\hat{z}$ points axially along the beam in the cavity, and $\hat{x}$ and $\hat{y}$ point radially. We may now write the Hermite-Gaussian function at any point in space [89]:

$$U_{\ell,m}(x,y,z) = A_{\ell,m} \exp\left[-ikz - ik\frac{x^2+y^2}{2R(z)} + i(\ell+m+1)\tan^{-1}\left(\frac{\lambda z}{\pi w_0^2}\right)\right] \quad (5.1)$$

Here I have explicitly separated the amplitude and phase of the mode (the reader is directed to Ref. [89] for the complete functional form and derivation). In Eq. 5.1, $A_{\ell,m}$ represents the mode amplitude, $R(z)$ is the radius of curvature of the wavefronts, and w_0 is a parameter specifying the beam width. We notice immediately that the phase is dependent upon the mode numbers (ℓ, m). Using Eq. 5.1, we can find the phase at any point along the cavity axis as a function of ℓ and m:

$$\phi(0,0,z) = kz - (\ell + m + 1)\tan^{-1}\left(\frac{\lambda z}{\pi w_0^2}\right) \tag{5.2}$$

In order for the resonator to transmit light, the beam must be in phase with itself after every pass around the ring. This condition demands that the accrued phase be an integer multiple of 2π. For a cavity with a round-trip path length L and a starting coordinate z_0, we can write:

$$2\pi n = kL - (\ell + m + 1)\left[\tan^{-1}\left(\frac{\lambda(z_0 + L)}{\pi w_0^2}\right) - \tan^{-1}\left(\frac{\lambda z_0}{\pi w_0^2}\right)\right] \tag{5.3}$$

where $n = 0, \pm 1, \pm 2 \ldots$. Substituting for k,

$$2\pi n = \frac{2\pi \nu L}{c} - (\ell + m + 1)\left[\tan^{-1}\left(\frac{\lambda(z_0 + L)}{\pi w_0^2}\right) - \tan^{-1}\left(\frac{\lambda z_0}{\pi w_0^2}\right)\right] \tag{5.4}$$

and rearranging,

$$\nu_{\ell,m,n} = \frac{nc}{L} + \frac{c}{2\pi L}(\ell + m + 1)\left[\tan^{-1}\left(\frac{\lambda(z_0 + L)}{\pi w_0^2}\right) - \tan^{-1}\left(\frac{\lambda z_0}{\pi w_0^2}\right)\right] \tag{5.5}$$

We can now clearly see that the resonant frequencies of the cavity, $\nu_{\ell,m,n}$, are different for the various (ℓ, m) modes. By altering the length of the cavity (and hence its resonant frequency), we will be able to select only the TEM_{00} mode. All other modes will be non-resonant and rejected from the cavity. As a check, consider the (0,0) mode propagating through a standard 2-mirror cavity with a return trip path length of $L = 2dn$ (n here is the index of refraction). Substitution into Eq. 5.5 gives a resonant mode spacing of $c/2dn$, the exact result found in Eq. 4.18 for the free spectral range of a non-confocal cavity.

5.2 Construction of the Monolaser

5.2.1 Baseplate and Housing

As mentioned above, all of the monolaser components sit on a 1.5" thick aluminum baseplate. The baseplate is designed to accommodate optical mounts while keeping the laser beam at a level height. As a result, a complex pattern of holes and grooves must be machined in the baseplate. We used a CNC mill to fashion the part from a solid 8" x 8" x 1.5" piece of aluminum stock. A photograph of the baseplate is shown in Fig. 5.3.

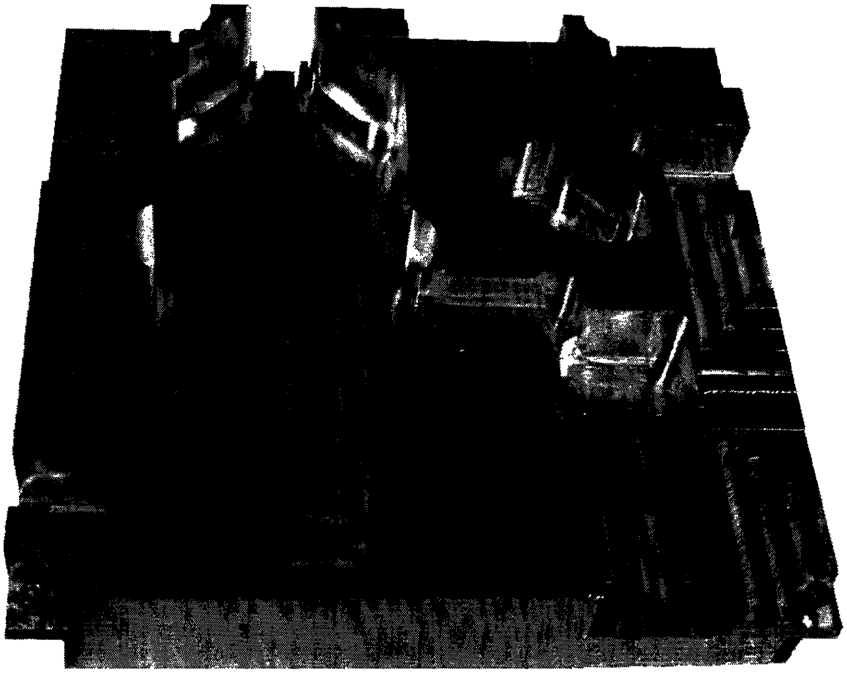

Figure 5-3: Photograph of the monolaser baseplate.

This entire baseplate is housed in a 10" x 10" vacuum-tight box. The walls are constructed from 3/8" aluminum and welded together to prevent leaks. A small turbo pump is connected to the box, and pressures as low as 8×10^{-5} Torr can be reached in less than an hour. The housing contains four 1/2" diameter posts on which the baseplate sits. As in the ECDL design presented in Chapter 4, the baseplate hovers above the bottom of the housing, thereby providing electrical and vibrational isolation from the external environment. The completed baseplate and housing, with all of the optical components attached, is shown in Fig. 5.4.

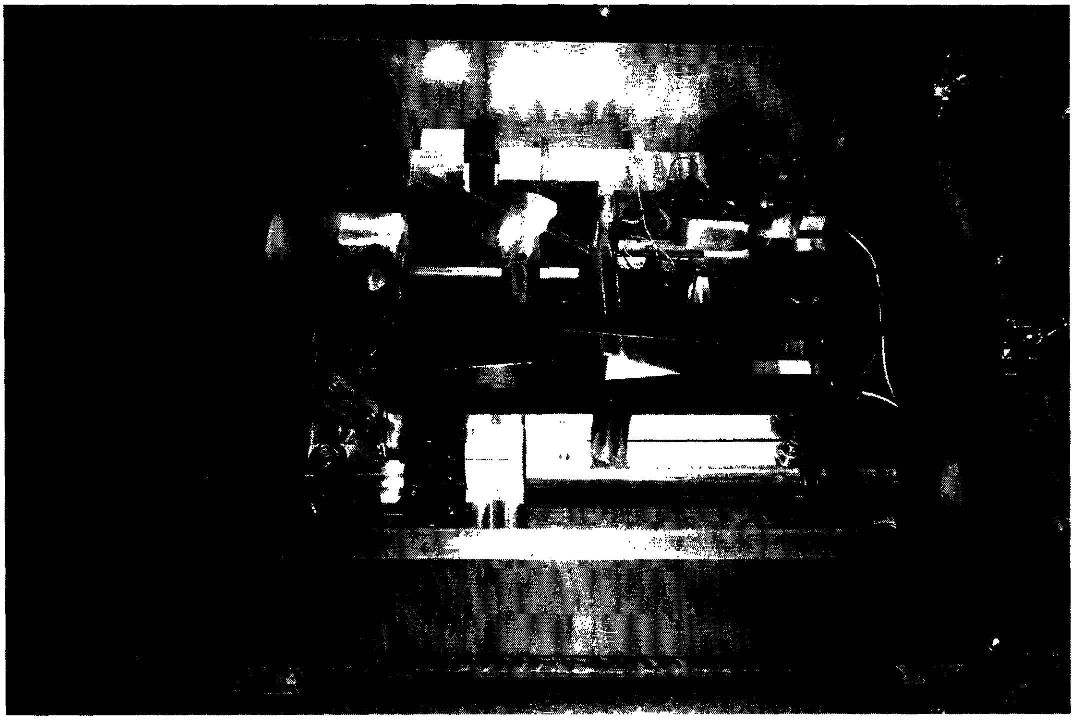

Figure 5-4: Photograph of the completed monolaser.

As before, a TEC/thermistor arrangement is used to actively stabilize the temperature inside the housing. Two TEC elements (ThorLabs TEC3-2.5) are coated with heat-sink grease and clamped in place between the baseplate and housing. A thermistor embedded in the baseplate provides a temperature reading to the control unit (Toptica DTC 110) that alters the TEC current accordingly to stabilize the temperature. Since the monolithic design is inherently resistant to change, small changes in the temperature setpoint will often require 30-60 minutes of equilibration time.

5.2.2 Diode Mounting, Collimation, and Frequency Tuning

For the monolaser, we begin by building an ECDL. The diode and collimating lens are mounted in precision-machined pieces of aluminum and aligned following the procedure introduced in Sec. 4.3.1. The result is a well-collimated beam .1" above the top of the baseplate. As before, the beam is then directed towards a diffraction grating, providing feedback to the diode. Rather than use a kinematic mount, the grating is secured to a trapezoidal metal piece with an embedded piezo for fine-tuning. Finely-threaded screws are used to control the grating position along all three directions.

At the start of the frequency tuning and feedback process, the screws are pre-tensioned to allow for adjustment in either direction. The collimated laser light is reflected off the grating, and the grating position is adjusted until the 1st order reflection is sent back to the diode. The position is then tweaked to give the maximum power output and lowest threshold.

After feedback optimization, the frequency of the laser is then measured. In all likelihood, the lasing frequency will not be the one desired. To fix this, the grating position must be delicately moved and feedback recaptured. This process can be iterated until the proper frequency is attained. Should this prove impossible, or should the mode be unstable, the temperature setpoint can be adjusted so that previously inaccessible modes can become usable.

5.2.3 Transmission Through the Filter Cavity

Two conditions must be met for optimal transmission through the cavity: the laser frequency must be resonant with the cavity TEM_{00} mode, and the beam must be well-aligned and mode-matched. To realize good transmission, we first scan the cavity piezo. This should give a series of peaks corresponding to transmission of the various allowed cavity modes. At this point, the cylindrical lenses should be adjusted so that only the TEM_{00} mode peak is transmitted. By re-tuning the alignment, the transmission can be optimized.

Fig. 5.5 shows the results of locking the laser to the cavity. We have successfully tuned the cavity so that it transmits only the Gaussian mode and rejects all higher order modes. Once we observe the strong Gaussian transmission, we are ready to employ electronic feedback to stabilize the laser over the long term.

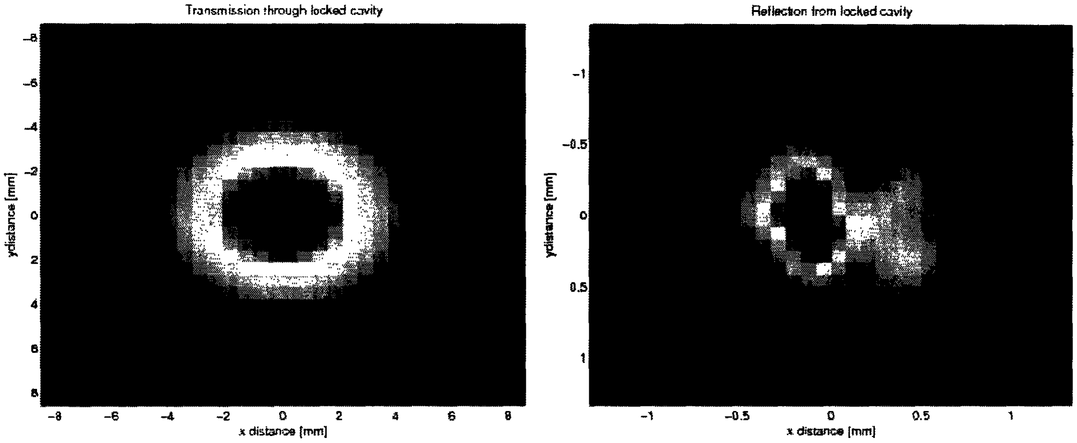

Figure 5-5: Transmission through and reflection from a well-aligned filter cavity. *Left:* transmission spectrum showing a Gaussian profile. *Right:* reflection from the cavity, showing the higher-order rejected modes.

5.2.4 Feedback and Operation

After the proper frequency and alignment are achieved, we wish to lock the laser frequency to the cavity. As noted above, we require the lasing frequency to be resonant with the TEM_{00} cavity mode and the feedback phase to be an integer multiple of 2π.

Ordinarily, the transmission through a cavity will exhibit a Lorentzian lineshape. In this setup, however, the transmission curve is greatly modified by the optical feedback. As shown in Fig. 5.6, the transmission rises sharply at some critical point, slowly climbs to a maximum, and falls to zero at a second critical point. Typically, the width of the transmission curves are of order 100 MHz, which is considerably larger than the FWHM of a high-finesse cavity peak.

As shown by Ohshima and Schnatz, the optimal conditions on frequency and phase are met when the transmission curve is symmetric [90]. Using this result, we can stabilize both the frequency and phase by using electronic feedback. Just as we peak locked to the Iodine transition in Chapter 4, we can peak lock the phase to the top of the transmission curve in this setup. Since we can start the lock at any point on the transmission curve, the locking range is several hundred MHz wide.

A lab-built software controller interfaces with an FPGA chip to simultaneously

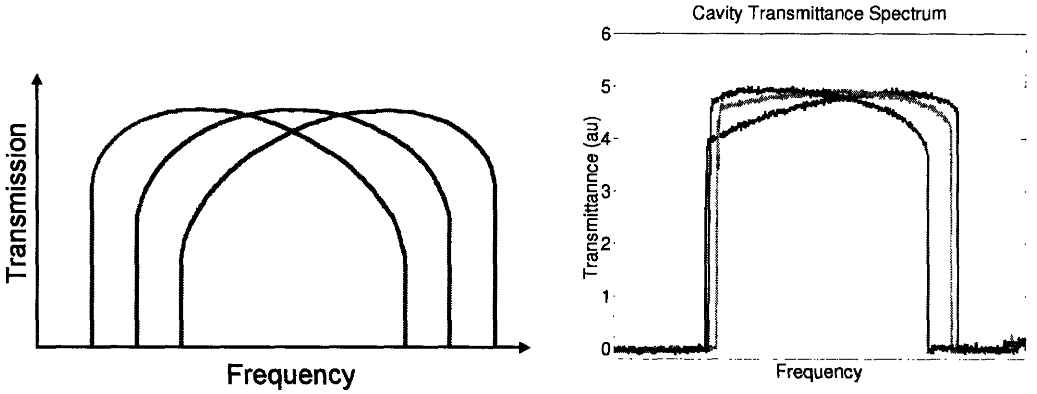

Figure 5-6: Filter cavity transmission spectrum with optical feedback. *Left:* theoretical spectrum, modelled after Fig. 2 in Ref. [90]. Three transmission curves, each with a different phase, are plotted as a function of frequency. Since there is no asymmetry to the center curve, the laser frequency is on resonance and the phase is an integer multiple of 2π. *Right:* experimental spectrum, obtained by sweeping the grating over the locking range for three different phase values. The green curve is symmetric, while the red and blue curves are oppositely antisymmetric.

lock the phase and frequency. A 10 kHz oscillator is used to dither the phase piezo (PZT-ϕ), and a photodiode at the far end of the filter cavity monitors the transmission. This signal is sent to an on-board lock-in amplifier that detects the 1f feedback and appropriately servos the piezo to compensate for drifts. This ensures that the phase remains at an optimal value.

In order to lock the frequency, we employ 3f feedback. This takes the third derivative of the transmission curve and sends the signal to another on-board lock-in amplifier. Any asymmetries in the transmission curve will be detected by the third derivative signal. To compensate, the feedback electronics servo the grating piezo until the third derivative signal is symmetric. As a result, the laser is locked precisely to the peak of the transmission curve where frequency and phase are optimal.

Once locked, the lasers remain stable for many hours. A spontaneous loss of lock is rarely observed; usually, the lasers unlock themselves when we tune too far away from the optimal frequency locking point. Although the frequency is tunable over a range of a few hundred MHz, the best stability is achieved when the system is left untouched. However, most of the red laser experiments demand sweeping the laser over some range to obtain data.

This problem can be solved by employing an acousto-optic modulator (AOM) in a double-pass configuration [91]. An AOM makes use of sound waves at rf frequencies to modulate the frequency of light passing through it. When an rf signal is sent to the AOM, it induces an oscillation in a piezo-electric transducer. This vibration causes sound waves to propagate through a crystal. Since the compression and rarefaction of the wave changes the index of refraction, an incoming laser beam can be diffracted by passing through the crystal. By conservation of energy and momentum, the light exiting the AOM will have a frequency $\nu + mf$, where ν is the incoming frequency, m is the diffraction order $(0, \pm 1, \pm 2, \ldots,)$, and f is the frequency of the sound wave.

To scan the laser frequency without touching the monolaser controls, we simply vary the frequency of the AOM rf drive. However, since the diffraction is generated by travelling sound waves, the diffraction angle depends on the input frequency. This can be problematic for beam alignment and fiber coupling, since scanning the drive frequency causes the beam to shift position. To circumvent this problem, we use the AOM in a double-pass configuration (see Fig. 5.7).

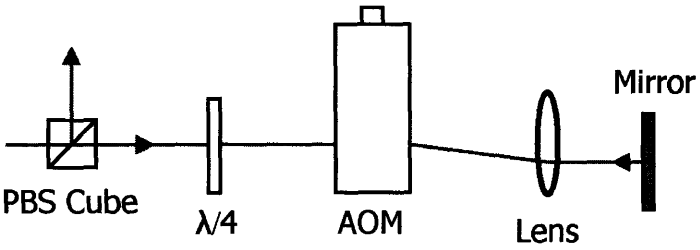

Figure 5-7: Schematic of an AOM in a double-pass configuration.

P-polarized light is transmitted through the PBS Cube, and a quarter wave plate converts the polarization to circular. After passing through the AOM, the beam is diffracted at some angle depending on the rf drive frequency. An off-center lens is used to bend the beam and direct it towards a mirror. When the system is aligned so that the beam reflects perpendicularly off the mirror, the laser will retrace its steps back through the lens and AOM. After it passes through the quarter wave plate, the light will be S-polarized, and will be reflected by the polarizing beam splitter cube. This beam will have a frequency $\nu + 2f$ since it has passed through the crystal twice. Additionally, changes in the rf drive frequency will not change the final position of the beam. As a result, this beam can be efficiently fiber coupled and sent to the ion trap.

5.3 Monolaser Stability

Once the monolaser was constructed and operational, we took some frequency stability measurements. Following the convention established in Chapter 4, we used a wavelength meter to monitor the instabilities over a 5 minute period (see Fig. 5.8). From the plot, we see a short-term peak-to-peak instability of ~500 kHz and a long-term drift of ~2 MHz. These results show that the monolaser is significantly more stable than the previous red laser. However, these numbers only give an upper bound on the frequency stability.

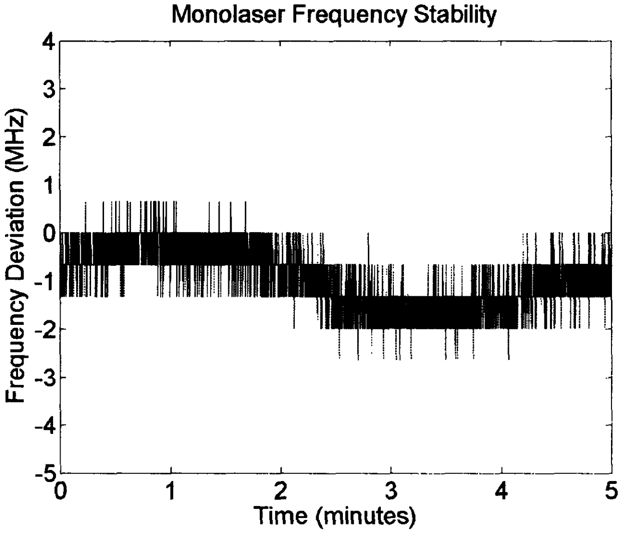

Figure 5-8: Monolaser frequency stability over a 5 minute period.

The wavemeter itself is not accurate enough to resolve frequency deviations on this order. To know the true stability of the red laser, we would require a more precise wavelength meter or a new method of measuring frequency instabilities.

In the meantime, we can improve our estimate somewhat by examining the performance of the monolaser used to address the 422nm transition. As we have seen, trapped strontium ions will fluoresce differently for different blue laser frequencies. When we have only a few ions in the trap, the blue laser resonance becomes quite narrow. Therefore, we can use the ion fluorescence signal as a gauge for locking the frequency of the blue laser.

With the blue laser locked to the ion signal, we recorded the 5-minute stability by monitoring the cavity piezo change. Converting this voltage into a frequency gives the plot shown in Fig. 5.9:

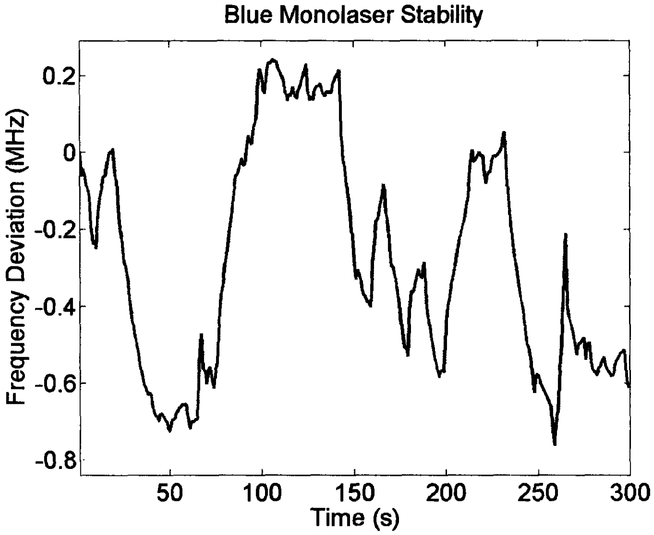

Figure 5-9: Blue monolaser frequency stability over a 5 minute period when locked to the ion fluorescence signal.

Although there is considerable noise due to photon counting statistics, ion motion, and other effects that impact fluorescence, we were able to measure a frequency instability of 1 MHz over a 5 minute period. Furthermore, in our experience, the red monolaser has always given more stable frequency readings than the blue monolaser (according to the wavelength meter). Thus, we can expect the red laser stability to be notably better than 1 MHz/5 minutes. This figure is quite encouraging, and should allow us to see the interesting effects discussed in Chapter 3.

5.4 Summary

In this chapter, we have introduced our design for a monolithic red laser that outputs a stable, Gaussian beam. By mounting the optical components on a single, thick piece of milled aluminum and enclosing the setup in a temperature-controlled, vacuum-sealed box, we were able to realize a stability of better than 1 MHz over 5 minutes. We shall now use our stable monolaser to probe the trapped strontium ions and witness the results.

Chapter 6

Experimental Setup and Results

Now that the monolaser has been constructed, we can explore the physical phenomena of depletion and quantum jumps as well as improve our estimate of ion temperature. This chapter will describe the setup for these experiments and present our collected data.

6.1 Ion Trap Setup

As we saw earlier, colder ion temperatures can be achieved by propagating the blue laser along multiple directions at once. With this in mind, the lasers were placed as shown in Fig. 6.1. The blue laser exits the fiber coupler and propagates diagonally through the ion trap, cooling one degree of freedom. After leaving the ion trap, the blue light is reflected from a hot/cold mirror, off a second mirror, and back through the ion trap axially. This permits cooling along two directions simultaneously.

The red laser, coaligned with the blue, makes the same trip in reverse. The red beam exits its fiber coupler, passes through the ion trap twice, and terminates at the blue fiber coupler. Since the IR beam is not needed for cooling, it is sufficient to have it pass through the trap just once. Along the axis of the linear trap, all three lasers are coaligned.

We carefully kept track of beam waists to ensure that the lasers were focussed to as small a spot size as possible at the center of the trap. The blue fiber coupler

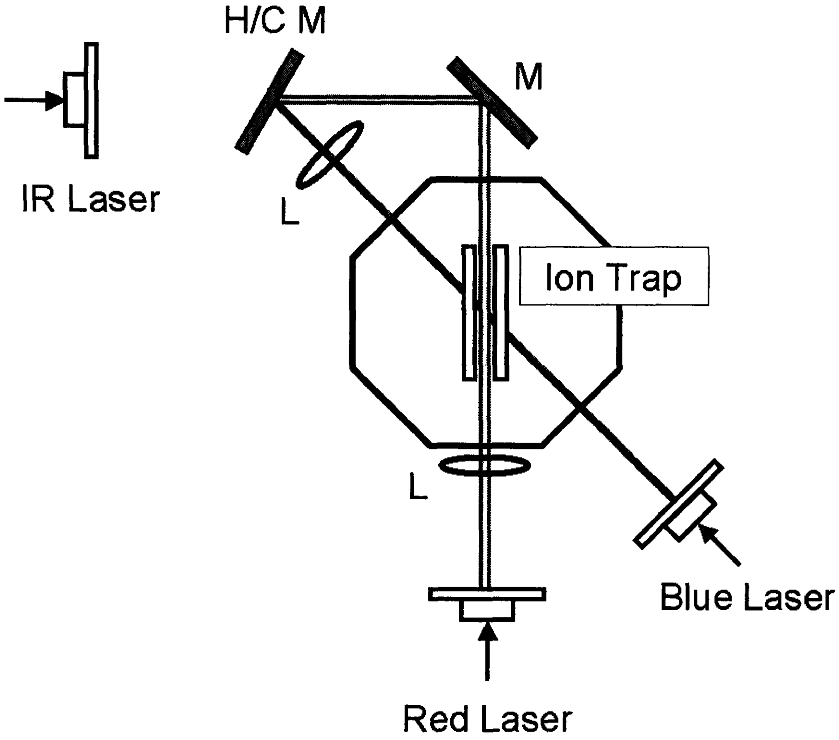

Figure 6-1: Schematic of the ion trap setup. The blue and red lasers propagate diagonally and axially, and the IR laser only propagates axially. M=Mirror, H/C M=Hot/Cold Mirror, L=Lens.

(ThorLabs FC230-A) was placed 10 cm away from the trapping region, corresponding to a spot size of 100 μm. We placed a lens at the far side of the trap to re-collimate the expanding blue beam before it is propagated axially. For the red beam, a lens was placed between the fiber coupler (ThorLabs FC230-B) and the trap, reducing the spot size to 80 μm.

Typically, the maximum operating powers are 250 μW for the blue, 500 μW for the IR, and 280 μW for the red. However, since these blue and red powers are both far above saturation, they will need to be reduced if we hope to see any meaningful data.

Now that the lasers have been set up, we can begin collecting data. We simply need to trap ions and adjust the laser powers and frequencies to look for the desired effects.

6.2 Depletion

As was explained in Chapter 3, we expect to see depletion when the red laser is consistently able to excite the $S \longrightarrow D_{5/2}$ transition with little competition from the blue laser. To begin our search for depletion, we loaded a cloud of ions and reduced the blue power to 100 μW. Almost immediately, the hints of a depletion signal were seen. By careful adjustment to the red laser position, we were able to obtain the signal shown in Fig. 6.2:

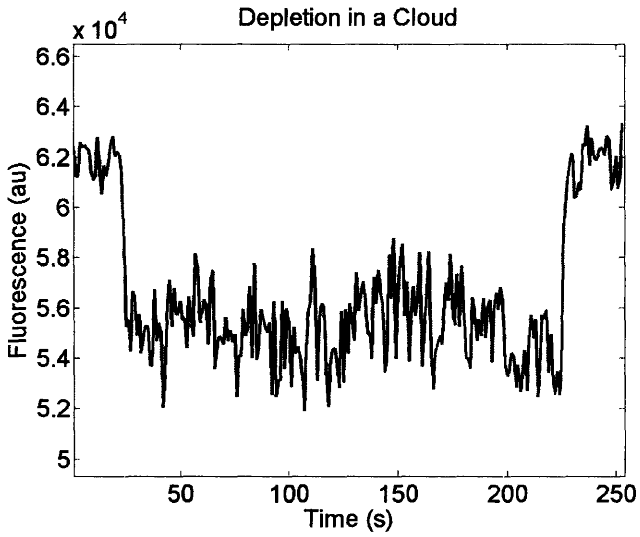

Figure 6-2: Depletion in an ion cloud. At t = 30 s, the red laser was turned on, causing a drop in the number of photon counts. At t = 225 s, the red laser was turned off, and the fluorescence returns to its previous value.

At the start of the scan, the red laser is blocked to establish a baseline value of ion fluorescence. After 30 seconds, the red laser is sent through the trap, depleting the $S \longrightarrow P$ transition and causing a dip in the 422nm photon signal. At $t = 225$ s, the red laser is blocked once again to ensure that the ion signal returns to its previous level.

We found that the strength of depletion remained relatively constant over a tuning range of several hundred MHz. This is an artifact of Doppler broadening of the red transition. In a hot cloud of ions, temperatures are typically of order ~1000 K, giving a Doppler-broadened FWHM of ~1 GHz. Thus, the red laser frequency can be significantly detuned, but still induce depletion in a cloud.

Clearly, we need to find the red line with much more precision if we are to perform further experiments. To reduce Doppler-broadening effects, we instead loaded a cold, crystallized chain of ions. Since typical crystal temperatures are less than 1 K, we expect the Doppler-broadened linewidth to decrease by at least 2 orders of magnitude. Finding depletion in this setup allows us to refine our red laser frequency placement.

With the laser set at the same frequency as in Fig. 6.2, we loaded a chain of ions to hunt for depletion. Not surprisingly, no depletion signal was seen. By tuning the laser across a wide range and observing the fluorescence, we were able to find the transition 200 MHz lower than our starting point. Data showing the depletion signal in a crystal can be seen in Fig. 6.3.

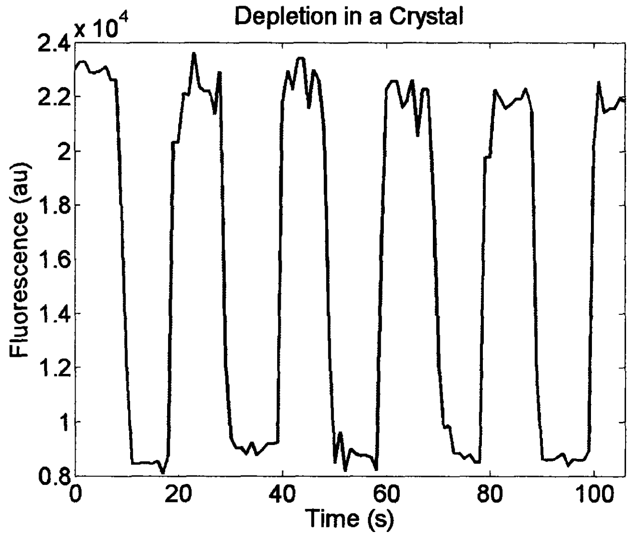

Figure 6-3: Depletion in an ion crystal. In this plot, the red laser was blinked on and off for 10 seconds each.

For this experiment, the red laser remained off for the first 10 seconds to again establish a fluorescence baseline. The red laser was turned on for the following 10 seconds, and the depletion is evident. This process was repeated dozens of times, five cycles of which are shown in the plot.

The fact that we found depletion in a crystal is an encouraging result. This demonstrates that we have found the transition whose linewidth is only a few MHz, and that our physical theory describing depletion is accurate. We are now ready to reduce the red power and search for quantum jumps.

6.3 Quantum Jumps

From the numerical solution and Monte-Carlo simulation presented in Sec. 3.3.2, we expect to see quantum jumps when the blue Rabi frequency is 10 MHz and the red Rabi frequency is several kHz. Since we know the linewidth, saturation intensity, and spot size of the blue laser, we can use Eq. 3.2 to determine the required power. Calculation gives that 5 μW of blue power focussed to a 100 μm spot corresponds to a Rabi frequency of 10 MHz. Similarly, a red Rabi frequency between 2 kHz and 40 kHz requires a red laser power of .08 μW to 30 μW focussed to an 80 μm spot size. We chose to use 5 μW of red power to look for quantum jump effects, giving $\Omega_{red} = 16$ kHz.

To begin, we loaded a cold chain of 3 ions. At first, we kept the red laser at high power and tuned the frequency until a depletion signal was seen. Once we verified that

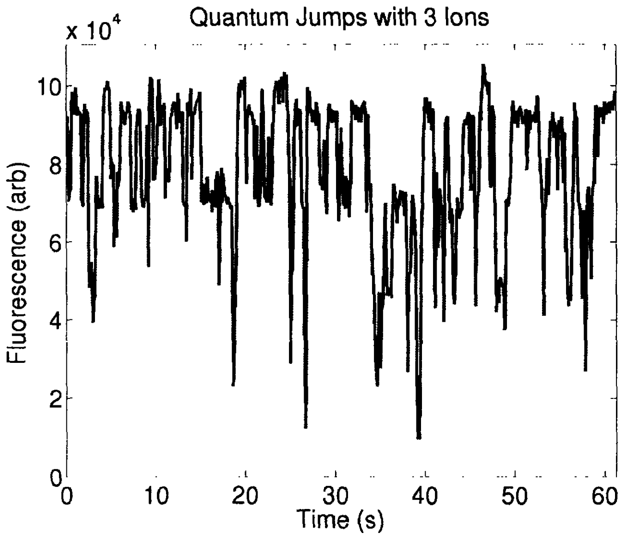

Figure 6-4: Quantum jumps of 3 trapped strontium ions. In this experiment, $\Omega_{blue} =$ 10 MHz and $\Omega_{red} = 16$ kHz.

we were on resonance, we turned the red power down to 5 μW to observe quantum jumps. A sample time-dependent scan is shown in Fig. 6.4.

Each ion exhibits the random loss of fluorescence that is the hallmark of quantum jumps. Since there are three ions in the trap, Fig. 6.4 effectively shows the sum of three individual quantum jump profiles. As expected, the ions hop fairly often since our red Rabi frequency is approaching the low end of the depletion limit. Additionally, we notice that the ions stay dark on average for 300-600 ms, in agreement with our simulations.

Since we have three ions in the trap, we would expect there to be four discrete levels of fluorescence, corresponding to 0, 1, 2, and 3 dark ions. By taking a histogram of the number of counts at each fluorescence level in Fig. 6.4, we can directly verify this assertion. This histogram is plotted in Fig. 6.5.

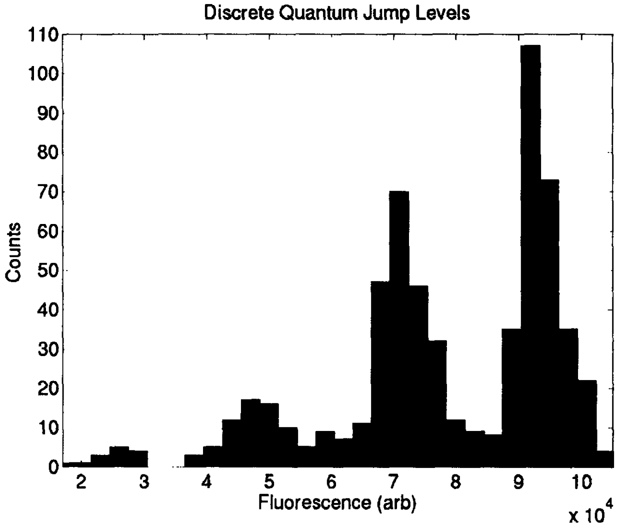

Figure 6-5: Discrete quantum jump levels. By taking a histogram of Fig. 6.4, we see the 4 expected fluorescence levels, representing 0, 1, 2, and 3 dark ions. Each of the peaks are evenly spaced since each ion fluoresces with equal intensity.

When running this experiment, we can expect each ion to transition to the $D_{5/2}$ state with some probability p. Thus, the probability of finding 1 dark ion is p, the probability of simultaneously finding 2 dark ions is p^2, and the probability of having 3 dark ions is p^3. By applying simple statistical methods to the data shown in Fig.

6.5, we can extract the transition probability p.

Of the 613 total events recorded in Figs. 6.4 and 6.5, 279 are at full fluorescence, 231 represent 1 dark ion, 83 represent 2 dark ions, and 20 represent 3 dark ions. By dividing the number of counts at each level by the total number of counts, we generate experimental data for p, p^2, and p^3. By taking the appropriate roots and averaging, we find that $p = .356$.

Let us examine the quality of this experimental result. Applying this value of p to the data, we would expect 289 counts at full fluorescence, 218 counts with 1 dark ion, 78 counts with 2 dark ions, and 28 counts with 3 dark ions. These numbers closely match the experimental results presented above. If we recall the results of Poisson counting statistics, we find that only the lowest fluorescence level lies more than one standard deviation away from the expected value.

Additionally, we can compare this probability to theoretical predictions. As shown in Fig. 3.4, when $p = .356$, $\Omega_{red} = 8$ kHz. Since the spot size of the red laser can easily be several 10's of μm larger than the theoretical optimum, the red Rabi frequency can range from 16 kHz down to 6.5 kHz. Thus, a measured value of $\Omega_{red} = 8$ kHz is well within the expected bounds.

6.4 Temperature Measurements

6.4.1 Blue-broadened Regime

In addition to observing depletion and quantum jumps, we wish to accurately measure the temperature of our ions. As we saw in Chapter 3, sweeping the blue laser gives an inaccurate upper temperature bound of 660 mK. To make a more precise measurement, we must keep the blue laser at a fixed frequency (and therefore fixed cooling) while sweeping the red laser.

We begin the process by again searching for a depletion signal. Once we have confirmed that the lasers are on resonance, we simply scan the frequency of the red laser and monitor the ion signal. As the red frequency is detuned from resonance, we expect the depletion effects to abate and the fluorescence to increase.

For our first iteration of the experiment, we set the blue power to 100 μW and the red power to 280 μW. This corresponds to a relatively large red power with a Rabi frequency of 120 kHz. Holding the blue laser at fixed frequency, we scanned the red frequency over a 40 MHz range by using the AOM. The captured fluorescence signal from this scan is shown in Fig. 6.6.

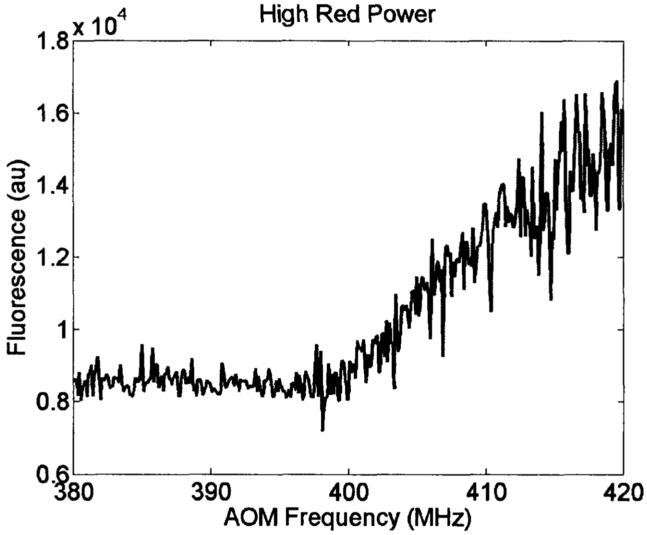

Figure 6-6: Frequency dependence of ion fluorescence in the high red power limit.

The results of the scan closely match the prediction shown in Fig. 3.6 *Left*. We see that at the low frequency side of the scan, frequency has little effect on fluorescence. At these points, the transition is saturated, and no further depletion can occur. As the frequency is tuned off resonance, we regain the familiar Lorentzian-type tails.

As discussed in Sec. 3.3.3, we can recover the full line by decreasing the red laser power. Using 10 μW of blue power and 50 μW of red, we took another 40 MHz scan using the AOM (see Fig. 6.7).

Since the red power has been lowered, we can observe the full line. As expected, the blue laser causes broadening of the transition, adding to the Doppler linewidth of the ion. Since the blue broadening causes a Lorentzian lineshape and Doppler broadening exhibits a Gaussian profile, we expect the scan to have a Voigt lineshape

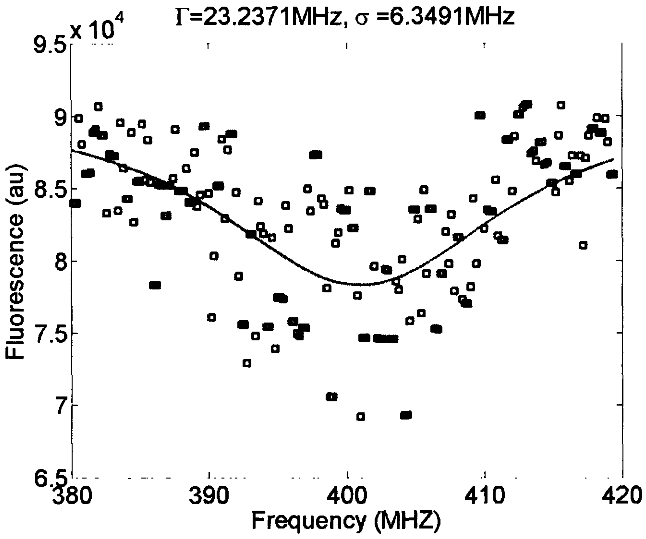

Figure 6-7: Frequency dependence of ion fluorescence in the low red power limit. The red line is a fitted Voigt function, giving a Lorentzian linewidth of 23 MHz and a Gaussian linewidth of 6 MHz.

(i.e. a convolution of Lorentzian and Gaussian).

With this in mind, we fit the data in Fig. 6.7 to a Voigt function, allowing us to extract a Lorentzian and a Gaussian linewidth. From the fit, we find that the blue laser broadens the transition by $\Gamma = 23.2$ MHz, consistent with our expectations. As for the Gaussian component, we find that $\sigma = 6.3$ MHz. Plugging this value into the Doppler broadening equation, we calculate an ion temperature of 35 mK. This represents a significant improvement over our previous upper bound of 660 mK.

This result is nearly three orders of magnitude larger than the Doppler cooling limit. We suspect that there are two primary contributions to ion temperature. The first relates to our setup: since we only cool two degrees of freedom, we can never expect to reach the Doppler limit. The second contribution is likely excess micromotion, which can be reduced by better compensation.

Once the micromotion has been abated, the ion temperature will necessarily drop. However, we quickly move beyond the limit where the Voigt fitting procedure gives useful results, since the Lorentzian lineshape will begin to dominate the Gaussian. We therefore need to develop a new methodology to probe the red transition without broadening it. By implementing pulse sequences, we will be able to move to the resolved sideband regime and more accurately measure colder temperatures.

6.4.2 Resolved Sideband Regime

Sidebands can never be resolved when the red transition is broadened by the blue laser, since the broadening is $\sim$20 times larger than the sideband spacing. Therefore, if we hope to observe sidebands and extract cold ion temperatures, the blue laser must be turned off whenever we irradiate the ion with 674nm light.

To accomplish this, we use pulse sequences to precisely control the delivery of laser light to the ion trap. At the start of the sequence, the blue laser is used to cool the ions for 10 ms while the red laser remains off. After 10 ms, the blue laser is turned off and the red laser is turned on for 10 ms. At $t = 20$ ms, the red laser is turned off and the cycle begins anew.

Should the red laser excite a transition, there will be a drop in fluorescence when the blue laser turns on. This drop is a direct result of depletion, and should be observable with a photon counter. As before, we expect the strength of depletion to increase on resonance and subside as the frequency is detuned. However, due to the presence of sidebands, we expect dips in fluorescence when the detuning is an integer multiple of the secular frequency.

Our procedure is as follows. We start the pulse sequence at some red AOM frequency and monitor the number of photon counts. We iterate the sequence 50 times and sum the total number of counts in order to build up statistics. Then, the red AOM frequency is incremented slightly and 50 more pulse cycles are run. In this way, we expect to observe the red spectrum without being broadened by the blue laser.

The results of this scan are shown in Fig. 6.8, along with a fit to the data. We see that the two sidebands are both spaced 650 kHz away from the carrier, consistent with our expectation of the secular frequency. Furthermore, as we increase the secular frequency by tightening the trap potential, we observe an increase in the sideband spacing.

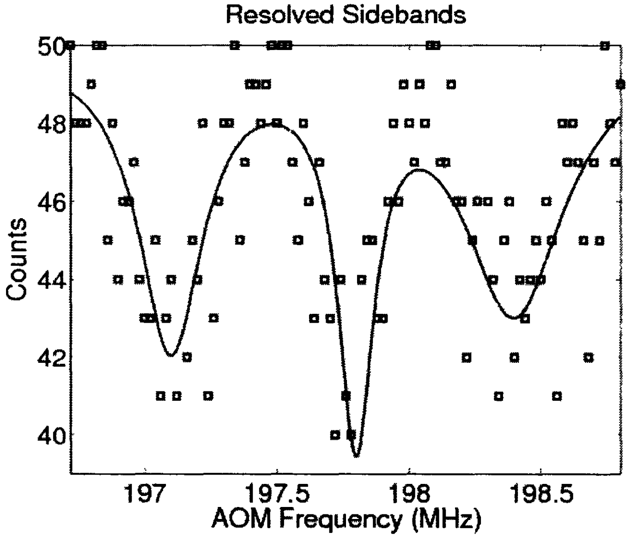

Figure 6-8: The 674nm transition spectrum with resolved sidebands. From the fitted Lorentzians, we observe an equal spacing of 650 kHz.

Additionally, we see that the amplitudes of the two sidebands are approximately equal. Thus, we need to use Eqs. 3.7 and 3.8 to determine the number of motional quanta $\langle m \rangle$. By taking the ratios of the fitted peak amplitudes, we find that $\langle m \rangle = 143^{+90}_{-46}$. If we then plug this value of $\langle m \rangle$ into Eq. 3.6, we can calculate an ion temperature of $6.8^{+4.4}_{-2.2}$ mK. Given that we only Doppler cool along two directions and that there are still visible traces of micromotion, it should be possible to cool the ions further in future experiments.

Chapter 7

Conclusion

In this thesis, we have explored the design and construction of two laser systems to probe the 674nm transition of $^{88}\text{Sr}^{+}$ in a linear Paul trap. Initial experiments showed that the laser stabilization provided by a low-finesse Fabry-Perot cavity was an unsuitable 50 MHz over 5 minutes. As a result, we designed and built a dual-laser setup to stabilize the cavity to an Iodine transition. Although a variety of different locking methods were explored, the best stability observed was 2-3 MHz over short time scales and 10 MHz over 5 minutes. Since this was still insufficient, a completely new laser architecture was required to improve the stability.

We developed a monolithic red laser to provide better performance. The ECDL, optics, and a triangular Fabry-Perot filter cavity were mounted on a single aluminum baseplate housed in a temperature-controlled, vacuum-sealed box. Consequently, frequency instabilities due to temperature and pressure fluctuations were minimized. Locking was achieved via resonant optical feedback as well as 1f/3f electronic feedback, and was robust enough to last for many hours. The output of the monolaser was a Gaussian beam with a frequency stability of at least 1 MHz over 5 minutes and an estimated linewidth less than 10 kHz.

Using the monolaser, we were able to perform three types of experiments in our strontium trap. The first was a depletion experiment, in which the red laser was used to depopulate the 422nm $S \rightarrow P$ transition. Since our camera and photon counter detect the emission of 422nm photons, depopulation of the transition causes a measurable dip in the fluorescence signal. By setting the red laser on resonance and monitoring the ions, we could observe depletion effects.

Next, we succeeded in observing quantum jumps. Theory predicts that when the red and blue powers are in an intermediate regime, they will compete to drive either the $S \longrightarrow P$ or $S \longrightarrow D_{5/2}$ transition. Whenever the ion transitions to the $D_{5/2}$ state, the fluorescence signal will disappear. By tuning the red and blue laser powers to theoretically predicted values, we witnessed the spontaneous loss of fluorescence that is the signature of quantum jumps. We showed that when there were three ions in the trap, the time-dependent fluorescence signal exhibited four discrete levels, corresponding to 0, 1, 2, and 3 dark ions. By some simple statistical analysis, we showed that the number of counts at each level was consistent with a single probability of transitioning, $p = .356$.

Additionally, we were able to vastly improve our measurement of the ion temperature. Without the red laser, the temperature was determined by sweeping the blue laser to observe a half-Voigt profile. Since sweeping the blue frequency directly effects the ion cooling, the result of 660 mK provided only an upper bound on temperature.

Since the 674nm line is independent of the cooling transition, the red laser can be swept to determine the Doppler linewidth, and hence temperature, of the ion. When the red laser power was high, we observed a saturation effect, where the red laser could not induce any further drop in fluorescence. By lowering the red laser power, we were able to see the full line. Fitting this line to a Voigt profile gave a Lorentzian linewidth of 23 MHz and a Gaussian linewidth of 6 MHz. The Lorentzian component was a direct result of blue-laser broadening, while the Gaussian component corresponded to a temperature of 35 mK.

Finally, we were able to observe sidebands of the red transition, which arise due to the secular motion in ion traps. By applying a chain of pulse sequences, we could resolve features previously shrouded by the blue laser. We found that the sidebands were equally separated from the carrier by 650 kHz, and that the separation could be changed by altering the trapping potential. By taking the ratios of peak heights, we were able to determine the average number of motional quanta $\langle m \rangle = 143^{+90}_{-46}$. From this value, we used the Planck distribution to extract an ion temperature of $6.8^{+4.4}_{-2.2}$ mK. Since this is still two orders of magnitude above the Doppler limit, we concluded that further ion cooling should be possible.

The work in this thesis has paved the way for the next class of interesting strontium ion trap experiments. The logical next step is to further cool our trapped ions. By sending a blue laser down the third degree of freedom and devising methods to improve micromotion compensation, we can hope to reduce the number of motional quanta and approach the Doppler limit.

Beyond this, we would like to sideband cool our ion to reach the motional ground state. To accomplish this task, most experimental groups use a temperature-controlled, vacuum-sealed high-finesse Fabry-Perot cavity fashioned from an ultra-low coefficient of thermal expansion material. Peak locking to such a narrow cavity resonance typically gives stabilities on the order of 10 Hz over 5 minutes. Our quoted monolaser stability compares unfavorably to this value. Therefore, while we may be able to sideband cool with the monolaser, the best data will likely be obtained after building a high-finesse cavity setup. Additionally, sideband cooling would require the construction of a 1033nm laser to ensure that the cooling rate is faster than the environmental heating rate.

Once the ions are in their motional ground state, they can be entangled and used to perform quantum computations. While large-scale quantum computation is likely years away, the foundations of the field are already in place. Many consider ion traps to be the leading candidate for experimental realization of quantum computing, and several computer architectures involving ion traps have been proposed. The work presented in this thesis represents a necessary foundation for realization of these long-term goals.

Appendix A

MATLAB Code for Quantum Jump Simulations

```
%%%%%%%%%%%%%%%%%%%%%%%%%%%%%%%%%%%%%%%%%
% fluorescence.m
% Phil Richerme (richerme@mit.edu)
% 12.7.05
% Evolves the 3 level Sr system in time
%%%%%%%%%%%%%%%%%%%%%%%%%%%%%%%%%%%%%%%%%
clear;
format long;

% Set parameters:
Wps=1e7; %\Omega for s-p transition (blue)
Wds=4e3; %\Omega for s-d transition (red)
gps=2e7; %gamma for s-p transition
gds=sqrt(gps/10^7); %gamma for s-d transition
t=5e-9; %timestep
T=1e-3; %Time window
totalT=10000e-3; %Total Experimental Time
```

```
% Set up matrices and vectors:
s=[1;0;0];
p=[0;1;0];
d=[0;0;1];
H=hbar/2*[0 Wps Wds; Wps 0 0; Wds 0 0];
Hc=H-i*hbar/2*gps*p*p'-i*hbar/2*gds*d*d';
U=expm(-i*t*Hc/hbar);

% Set Constants and Initialize variables:
hbar=6.626e-34;
psi=s;

% Run the algorithm
for n=1:totalT/T
    photons=0; % Reset Counter
    for j=1:T/t
        psi=U*psi;
        psi=psi/norm(psi);
        r=rand([1 1]);
        p1=gps*abs(psi(2,1))^2*t;
        p2=gds*abs(psi(3,1))^2*t;

        if p1>r %decay from p to s
            psi=s;
            photons=photons+1;
        end

        if p1+p2>r && r>p1 %decay from d to s
            psi=s;
        end
    end

    photonsmx(1,n)=photons;

    % Monitor Progress (comment out to increase speed)
    if length(photonsmx)/10==floor(length(photonsmx)/10)
        y=[0:1:length(photonsmx)-1];
        plot(y,photonsmx)
        pause(.001);
    end

end

x=[0:1:length(photonsmx)-1];
plot(x,photonsmx)
xlabel(‘Time Bins’,‘FontSize’,14);
ylabel(‘Counts’,‘FontSize’,14);
title(‘Fluorescence vs. Time’,‘FontSize’,16);

%Re-plot with 10ms and 100ms time bins
if 10e-3>T && 10e-3<totalT
    j=totalT/10e-3;
    k=10e-3/T;
    for n=1:j
        Aa=k*n-k+1;
        Ab=k*n;
        A(1,n)=sum(photonsmx(1,Aa:Ab));
    end
    Ax=[0:1:j-1];
    figure;
    plot(Ax,A)
    xlabel('Time Bins (10ms each)','FontSize',14);
    ylabel('Counts','FontSize',14);
    title('Fluorescence vs. Time','FontSize',16);
end

if 100e-3>T && 100e-3<totalT
    j=totalT/100e-3;
    k=100e-3/T;
    for n=1:j
        Ba=k*n-k+1;
        Bb=k*n;
        B(1,n)=sum(photonsmx(1,Ba:Bb));
    end
    Bx=[0:1:j-1];
    figure;
    plot(Bx,B)
    xlabel('Time Bins (100ms each)','FontSize',14);
    ylabel('Counts','FontSize',14);
    title('Fluorescence vs. Time','FontSize',16);
end
```

Bibliography

[1] P. K. Ghosh. *Ion Traps.* Clarendon Press, Oxford (1995).

[2] F. G. Major, V. N. Gheorghe, and G. Werth. *Charged Particle Traps.* Springer, Berlin (2005).

[3] H. Friedburg and W. Paul. *Naturwissenschaft* **38**, 159 (1951).

[4] H. G. Bennewitz and W. Paul. *Z. Phys.* **139**, 489 (1954).

[5] H. G. Dehmelt. *Adv. in Atom. and Mol. Phys.* **5**, 109 (1969).

[6] G. Gräff, F. G. Major, R. Roeder, and G. Werth. *Phys. Rev. Lett.* **30**, 1155 (1968).

[7] R. S. Van Dyck Jr., P. B. Schwinberg, and H. G. Dehmelt. *Phys. Rev. Lett.* **59**, 26 (1987).

[8] W. M. Itano, D. J. Heinzen, J. J. Bollinger, and D. J. Wineland. *Phys. Rev. A* **41**, 2295 (1990).

[9] E. Fischer. *Z. Phys.* **156**, 1 (1959).

[10] M. Bradley, J. Porto, S. Rainville, J. Thompson, and D. E. Pritchard. *Phys. Rev. Lett.* **83**, 4510 (1999).

[11] D. J. Wineland, M. Barrett, J. Britton, J. Chiaverini, B. L. DeMarco, W. M. Itano, B. M. Jelenkovic, C. Langer, D. Leibfried, V. Meyer, T. Rosenband, and T. Schaetz. *Phil. Trans. Royal Soc. London A* **361**, 1349 (2003).

[12] S. Gulde, M. Riebe, G. Lancaster, C. Becher, J. Eschner, H. Häffner, F. Schmidt-Kaler, I. L. Chuang, and R. Blatt. *Nature* **421**, 48 (2003).

[13] S. Earnshaw. *Trans. Camb. Phil. Soc.* **7**, 97 (1842).

[14] F. M. Penning. *Physica* **3**, 873 (1936).

[15] W. Paul, O. Osberghaus, and E. Fischer. *Fort. des Wirt. und Verkher. Nordrhein-Westfalen* **415**, (1958).

[16] R. F. Wuerker, H. Shelton, and R. V. Langmuir. *J. Appl. Phys.* **30**, 342 (1959).

[17] W. Paul. *Rev. Mod. Phys.* **62**, 531 (1990).

[18] M. G. Raizen, J. M. Gilligan, J. C. Bergquist, W. M. Itano, and D. J. Wineland. *Phys. Rev. A* **45**, 6493 (1992).

[19] J. I. Cirac and P. Zoller. *Phys. Rev. Lett.* **74**, 4091 (1995).

[20] R. E. March and J. Todd. *Quadrupole Ion Trap Mass Spectrometry.* John Wiley & Sons, Hoboken, NJ (2005) p. 39.

[21] E. Mathieu. *J. Math. Pure. Appl.* **13**, 137 (1868).

[22] G. Floquet. *Ann. l'Ecole Norm. Sup.* **12**, 47 (1883).

[23] F. M. Arscott. *Periodic Differential Equations.* Pergamon Press, New York (1964) p. 121.

[24] H. Schnitzler. Ph.D. Thesis, University of Konstanz (2001) p. 16.

[25] N. W. McLachlan. *Theory and Application of Mathieu Functions.* Clarendon Press, Oxford (1947) pp. 10-17.

[26] P. L. Kapitsa. *Zh. Eksp. Teor. Fiz.* **34**, 242 (1951).

[27] B. King. Ph.D. Thesis, University of Colorado Boulder (1999) pp. 10-11.

[28] D. J. Berkeland, J. D. Miller, J. C. Bergquist, W. M. Itano, and D. J. Wineland. *J. Appl. Phys.* **83**, 10 (1998).

[29] J. Chiaverini, J. Britton, D. Leibfried, E. Knill, M. D. Barrett, R. B. Blakestad, W. M. Itano, J. D. Jost, C. Langer, R. Ozeri, T. Schaetz, and D. J. Wineland. *Science* **308**, 997 (2005).

[30] H. C. Nägerl, Ch. Roos, D. Leibfried, H. Rohde, G. Thalhammer, J. Eschner, F. Schmidt-Kaler, and R. Blatt. *Phys. Rev. A* **61**, 023405 (2000).

[31] K. Toyoda, A. Miura, S. Urabe, K. Hayasaka, and M. Watanabe. *Opt. Lett.* **26**, 1897 (2001).

[32] M. Musha, A. Zvyagin, K. Nakagawa, and M. Ohtsu. *Jpn. J. Appl. Phys.* **33**, 1603 (1994).

[33] G. Barwood, K. Gao, P. Gill, G. Huang, and H. Klein. *IEEE Trans. Inst. Meas.* **50**, 543 (2001).

[34] K. R. Brown, R. J. Clark, J. Labaziewicz, P. Richerme, D. R. Leibrandt, and I. L. Chuang, quant-ph/0603142.

[35] K.-A. Brickman, P. C. Haljan, P. J. Lee, M. Acton, L. Deslauriers, and C. Monroe. *Phys. Rev. A*, **72**, 050306 (2005).

[36] D. J. Wineland and H. Dehmelt. *Bull. Am. Phys. Soc.* **20**, 637 (1975).

[37] S. Stenholm. *Rev. Mod. Phys.* **58**, 699 (1986).

[38] Y. Castin, H. Wallis, and J. Dalibard. *J. Opt. Soc. Am. B* **6**, 2046 (1989).

[39] H. S. Margolis, G. Huang, G. P. Barwood, S. N. Lea, H. Klein, W. H. C. Rowley, and P. Gill. *Phys. Rev. A* **67**, 032501 (2003).

[40] S. A. Diddams, T. Udem, J. C. Bergquist, E. A. Curtis, R. E. Drullinger, L. Hollberg, W. M. Itano, W. D. Lee, C. W. Oates, K. R. Vogel, and D. J. Wineland. *Science* **293**, 825 (2001).

[41] H. S. Margolis, G. P. Barwood, G. Huang, H. Klein, S. N. Lea, K. Szymaniec, and P. Gill. *Science* **306**, 1355 (2004).

[42] D. Stevens, J. Brochard, and A. M. Steane. *Phys. Rev. A* **58**, 2750 (1998).

[43] D. J. Berkeland. *Los Alamos Science* **27**, 178 (2002).

[44] M. L. Citron, H. R. Gray, C. W. Gabel, and C. R. Stroud Jr. *Phys. Rev. A* **16**, 1507 (1977).

[45] H. J. Metcalf and P. van der Straten. *Laser Cooling and Trapping.* Springer Verlag, New York (1999) pp. 24-27.

[46] J. C. Bergquist, R. Hulet, W. M. Itano, and D. J. Wineland. *Phys. Rev. Lett.* **57**, 1699 (1986).

[47] P. A. Barton, C. J. S. Donald, D. M. Lucas, D. A. Stevens, A. M. Steane, and D. N. Stacey. *Phys. Rev. A* **62**, 032503 (2000).

[48] D. J. Berkeland. *Rev. Sci. Inst.* **73**, 2856 (2002).

[49] D. J. Berkeland, D. A. Raymondson, and V. M. Tassin. *Phys. Rev. A* **69**, 052103 (2004).

[50] L. M. Narducci, M. O. Scully, G.-L. Oppo, P. Ru, and J. R. Tredicce. *Phys. Rev. A* **42**, 1630 (1990).

[51] S. H. Autler and C. H. Townes. *Phys. Rev.* **100**, 703 (1955).

[52] G. P. Barwood, P. Gill, H. A. Klein, and W. R. C. Rowley. *IEEE Trans. on Inst. and Meas.* **46**, 133 (1997).

[53] D. J. Wineland, W. M. Itano, J. C. Bergquist, and R. G. Hulet. *Phys. Rev. A* **36**, 2220 (1987).

[54] F. Reif. *Fundamentals of Statistical and Thermal Physics.* McGraw Hill, Boston (1965) p. 340.

[55] F. Diedrich, J. C. Bergquist, W. M. Itano, and D. J. Wineland. *Phys. Rev. Lett.* **62**, 403 (1989).

[56] E. Peik, J. Abel, T. Becker, J. von Zanthier, and H. Walther. *Phys. Rev. A* **60**, 439 (1999).

[57] Ch. Roos, Th. Zeiger, H. Rohde, H. C. Nägerl, J. Eschner, D. Liebfried, F. Schmidt-Kaler, and R. Blatt. *Phys. Rev. Lett.* **83**, 4713 (1999).

[58] C. E. Wieman and L. Hollberg. *Rev. Sci. Inst.* **62**, 1 (1991).

[59] G. Burns and M. I. Nathan. *Proc. of the IEEE* **52**, 770 (1964).

[60] M. I. Nathan. *Appl. Opt.* **5**, 1514 (1966).

[61] Y. M. Popov. *Appl. Opt.* **6**, 1818 (1967).

[62] J. C. Camparo. *Contemp. Phys.* **26**, 443 (1985).

[63] W. P. Dumke. *Phys. Rev.* **127**, 1559 (1962).

[64] C. Kittel. *Introduction to Solid State Physics.* John Wiley & Sons, Hoboken, NJ (1996) p. 587.

[65] M. W. Fleming and A. Mooradian. *IEEE J. Quant. Elect.* **17**, 44 (1981).

[66] K. B. MacAdam, A. Steinbach, and C. E. Wieman. *Am. J. Phys.* **60**, 1098 (1992).

[67] L. Ricci, M. Weidemüller, T. Esslinger, A. Hemmerich, C. Zimmermann, V. Vuletic, W. König, T. W. Hänsch. *Opt. Comm.* **117**, 541 (1995).

[68] A. S. Arnold, J. S. Wilson, and M. G. Boshier. *Rev. Sci. Inst.* **69**, 1236 (1998).

[69] C. Kittel and H. Kroemer. *Thermal Physics.* W. H. Freeman & Co., New York (1980) p. 393.

[70] V. S. Letokhov. *Topics in Applied Physics; Chapter 4: Saturation Spectroscopy.* Ed. K. Shimoda. Springer-Verlag, New York (1976).

[71] P. G. Pappas, M. M. Burns, D. D. Hinshelwood, M. S. Feld, and D. E. Murnick. *Phys. Rev. A.* **21**, 1955 (1980).

[72] J. R. Brandenburger. *Phys. Rev. A.* **39**, 64 (1989).

[73] B. B. Rossi. *Optics.* Addison Wesley, Reading, MA (1957) pp. 140-145.

[74] G. Bekefi and A. H. Barrett. *Electromagnetic Vibrations, Waves, and Radiation.* MIT Press, Cambridge, MA (1977) pp. 549-552.

[75] G. Hernandez. *Fabry-Perot Interferometers.* Cambridge University Press, Cambridge (1986).

[76] W. Luhs. *Fabry-Perot Resonator.* MEOS GmbH 79427, Eschbach (1992).

[77] H. Mabuchi, Q. A. Turchette, M. S. Chapman, and H. J. Kimble. *Optics Lett.* **21**, 1393 (1996).

[78] B. C. Young, F. C. Cruz, W. M. Itano, and J. C. Bergquist. *Phys. Rev. Lett.* **82**, 3799 (1999).

[79] A. Schoof, J. Grünert, S. Ritter, and A. Hemmerich. *Optics Lett.* **26**, 1562 (2001).

[80] R. W. Fox, C. W. Oates, and L. W. Hollberg. *Experimental Methods in the Physical Sciences, Chap 1: Stabilizing Diode Lasers to High-Finesse Cavities.* Elsevier/Academic Press, San Diego (2003).

[81] C. Corwin. Ph.D. Thesis, University of Colorado Boulder (1999) pp. 110-116.

[82] S. Gerstenkorn and P. Luc. *Atlas du spectre d'absorption de la molecule d'iode.* CNRS, Paris (1982).

[83] B. Dahmani, L. Hollberg, and R. Drullinger. *Opt. Lett.* **12**, 876 (1987).

[84] K. Hayasaka. *Opt. Comm.* **206**, 401 (2002).

[85] B. Willke, N. Uehara, E. K. Gustafson, R. L. Byer, P. J. King, S. U. Seel, and R. L. Savage, Jr. *Opt. Lett.* **23**, 1704 (1998).

[86] Ph. Laurent, A. Clairon, and Ch. Breant. *IEEE J. of Quant. Elect.* **25**, 1131 (1989).

[87] H. Kogelnik and T. Li. *Appl. Opt.* **5**, 1550 (1966).

[88] K. D. Skeldon, K. A. Strain, A. I. Grant, and J. Hough. *Rev. Sci. Inst.* **67**, 2443 (1996).

[89] B. E. A. Saleh and M. C. Teich. *Fundamentals of Photonics.* John Wiley & Sons, New York (1991).

[90] S. Ohshima and H. Schnatz. *J. Appl. Phys.* **71**, 3114 (1992).

[91] E. A. Donley, T. P. Heavner, F. Levi, M. O. Tataw, and S. R. Jefferts. *Rev. Sci. Inst.* **76**, 063112 (2005).